Title
Processing-Dependent Growth Mechanisms and Performance Improvement of Kesterite Solar Cells

Author
Hsu, Wan-Ching

Publication Date
2014

Peer reviewed|Thesis/dissertation

UNIVERSITY OF CALIFORNIA

Los Angeles

Processing-Dependent Growth Mechanisms and Performance Improvement of Kesterite Solar Cells

A dissertation submitted in partial satisfaction of the
requirements for the degree Doctor of Philosophy

in Materials Science and Engineering

by

Wan-Ching Hsu

2014

ABSTRACT OF THE DISSERTATION

Processing-dependent Growth Mechanisms and Performance Improvement of Kesterite Solar Cells

by

Wan-Ching Hsu

Doctor of Philosophy in Materials Science and Engineering

University of California, Los Angeles, 2014

Professor Yang Yang, Chair

As the global population and economy grow rapidly, energy has been an increasingly difficult issue. We not only have to set our minds to developing new technologies to deliver carbon-neutral energy to prevent disastrous interference in the global climate, we also have to consider if the scale of the new energy is large enough to fulfill the growing demands, which will reach 28 TW by year 2050. Most of today's commercially available PVs used one or more rare elements. It is expected that, based on today's commercially available PVs, the production will bump into the ceiling of natural resources even before the needed scale has been reached. Kesterite solar cell composed of earth abundant elements prevents this issue.

To make kesterite solar cells realistic and cost-effective, both the cell performance and the manufacturing processes have to be effective enough, i.e. high power conversion

efficiency, low cost and high throughput. Co-evaporation, hydrazine-based processing and nanocrystal film selenization are three of the processes achieving the highest performance kesterite solar cells to-date (8% ~ 12%). This study aims for high power-conversion efficiency by playing to the strengths of these processes, while also taking realistic concerns, such as process scalability and simplicity, in to account. In-depth growth mechanisms, including the phase evolutions, reaction pathways, and morphology transitions, are studied to help to manage the challenges.

By understanding how to precisely control the composition/phases of films, 8-9% cell efficiencies are demonstrated by multiple co-evaporation deposition routes. A beneficial reaction pathway is suggested for the hydrazine-based processing, which may explain the high efficiency record set by the process. Through the analysis of the selenization effect and the engineering of the film surface composition, 8.6% cell efficiency has been obtained by the nanocrystal approach. The 8.6% device was finished by all-solution process all the way from kesterite deposition to transparent electrode deposition. The high performance of this all-solution processed device shows the great potential to manufacture low-cost, high-throughput, and high-performance kesterite solar cells in the future.

The dissertation of Wan-Ching Hsu is approved.

Eric Pei-Yu Chiou

Richard B. Kaner

Yang Yang, Committee Chair

University of California, Los Angeles

2014

Table of Contents

Chapter 1 Introduction of earth abundant kesterite solar cells 1

1.1 Natural resource limitation: the obstacle for PV to meet the growing energy demand 1

1.2 Kesterite: the earth abundant alternative to CIGS solar cells 3

1.3 The structural, optical, and electrical properties of kesterite 6

1.3.1 Crystal structure and optical properties 7

1.3.2 Electrical properties 9

1.4 Operating principles of kesterite solar cells 10

1.5 Overview of successful developed processes and recent progress 12

1.5.1 Single step vs two step: 13

1.5.2 Vapor phase vs liquid-phase deposition 14

1.5.3 Molecular-scale solutions vs nanocrystal inks 14

1.6 Influential factors to improve device performance 15

1.6.1 Composition and secondary phases 16

1.6.2 Composition and point defects 17

1.6.3 Grain morphology 18

Chapter 2 Co-evaporated kesterite 20

2.1 Strengths and challenges of co-evaporation 21

1.1.1 Real-time composition and phase manipulation 21

1.1.2 Difficulty of composition control by co-evaporation for kesterite 23

2.2 Experimental methods 26

2.2.1 Film growth strategies 26

2.2.2 Film characterization and device fabrication 30

2.3 Phase evolution and composition control 30

2.3.1 Logged temperature profile and the undesired Cu_xSe_y residual 30

2.3.2 Solution to consume Cu_xSe_y residual and the discussion of its origin 35

2.3.3 The phase evolution 37

2.3.4 Device performance from different strategies 38

2.3.5 Effect on grain size 40

2.4 Effect of ZnSe distribution on device performance 41

2.4.1 Effect of Zn/(Cu+Zn+Sn) ratio - bulk composition 42

2.4.2 Create ZnSe grains in different lateral positions 43

2.4.3 Effect of position of ZnSe grains on device performance 45

2.4.4 Blue-light induced breakdown 47

2.5 Summary and outlook 51

Chapter 3 Hydrazine-processed kesterite 54

3.1. Introduction to hydrazine-based processing 55

3.2 Experimental methods 57

3.2.1 Preparation of precursor solutions and inks 57

3.2.2 Precursor drying 58

3.2.3 XRD and Raman characterization 58

3.3 Precursor Species and Their Resulting Hydrazinium Frameworks 59

3.3.1 Zinc Species 60

3.3.2 Copper and Tin Species 61

3.3.3 Bimetallic Integration Process 62

3.4 Solid State Reaction Pathways 66

3.5 Comparison to the reaction pathways of other processes 72

3.6 Conclusions and outlook 73

Chapter 4 Kesterite from the selenization of nanocrystal films 75

4.1 Introduction and challenges of the nanocrystal selenization approach 76

4.1.1 Nanocrystal synthesis and film formation 76

4.1.2 Selenization and grain growth 78

4.1.3 Composition change during selenization 81

4.2 Experimental methods 82

4.2.1 Synthesis of nanocrystals 82

4.2.2 Absorber layer fabrication 83

4.2.3 Device Fabrication 84

4.2.4 Characterization 85

4.3 Selenium pressure-dependent grain morphology 85

4.3.1 Planar-type growth and inhomogeneous-type growth 86

4.3.2 Other effects on film morphology 89

4.3.3 How selenium vapor trigger the grain growing process 89

4.4 Inhomogeneous vertical composition distribution and altered surface composition 91

4.4.1 Composition depth profiling and Sn-rich surface composition 91

4.4.2 Surface composition engineering 95

4.5 All-solution processed device 97

4.6 Conclusion and Outlook 99

Chapter 5 Summary 101

Appendix A 105

Appendix B 109

References 111

List of Figures

Figure 1.1 The maximum potential of power production by PV is as high as 7500 TW assuming that the highest efficiency PV devices are used. However, only 1.5 TW can be delivered with natural resource limitation based on current technologies, which is only 15% of what we need by year 2050. 3

Figure 1.2 The relative abundance of elements by atom fraction in the Earth's upper continental crust according to US Geology Survey.[10] 4

Figure 1.3 Comparison of the crystal structure of chalcopyrite and kesterite. Adapted with permission © 2011 Elsevier. 8

Figure 1.4 Device structure and band diagram of kesterite solar cells..... 11

Figure 1.5 A sample current-voltage (IV) curve. $I_{SC} = J_{SC}$ * device area. 12

Figure 2.1 The logged deposition data of the co-evaporation run which yields a 19.9% CIGS solar cells.[79]..... 25

Figure 2.2 Three types of deposition recipes: type I starts Cu-rich, type II starts Zn-rich, and type III maintains constant rates throughout. The deposition rates in atom/unit time shown here are not precise numbers..... 27

Figure 2.3 Logged temperature profiles of type I (Cu-rich), II(Zn-rich), and III(constant rate) films. Samples T1, T2, and T3 are the products of these depositions, respectively. The interruption times of T1', T2'-a, and T2'-b are also indicated in the figure. In each completed deposition, we waited for the temperature to become level before we started to cool down the substrates. The solid arrows indicate the turn-off time for the evaporation rate of Cu and

dashed arrows indicate that of Zn. The temperature of the second turning points marked as "*" is strategy-dependent. 31

Figure 2.4 (a) Raman spectrum of two different spots of on T1' (in red and blue) and T1 (in black) (b) Raman spectrum of T2'-a (in red), T2'-b (in blue), and T2 (in black)..... 34

Figure 2.5 Emissivity of (a) film T1' (dashed line) and T1 (solid line) and (b) T2'-b (dashed line) and T2 (dashed line). 35

Figure 2.6 Morphology changes (a) from Cu-rich T1' to completed T1 for Type I and (b) from Zn-rich T2'-at to completed T2 of Type II. (Some bright features showing in T1 and T2 on the top of the films are due to the Zn cap applied during cool-down as discussed earlier. 38

Figure 2.7 The current density vs. voltage (JV) curves of one of the best devices fabricated by Type I (sample M3490), Type II (M3512), and Type III (M3461). Note that M3461 has a lower current because AR coating was not applied. 40

Figure 2.8 (a) Cross-sectional SEM images of films with A-relatively homogeneous composition (M3530, M3503), B-ZnSe grains on the back (M3480, M3490), and C-ZnSe grains on the front (M3531, M3463). (b) Depth profiles of Zn/(Cu+Zn+Sn) ratio derived from AES depth profile of M3530(A), M3490(B), and M3531(C). 45

Figure 2.9 Compositons of the mentioned films obtained from XRF. Until now, we have not found efficient devices with bulk composition poorer in Zn than this phase composition. Adapted with permission © 2013 Elsevier 45

Figure 2.10 (a) QE_{INT} of cells without large ZnSe grains (category A, M3530), with ZnSe grains on the front of absorber (category C, M3531) and the ratio between the two. (b) JV curves of the same two devices (M3530, and M3531) and their air-annealed counterparts (M3530-a, M3531-a). 47

Figure 2.11 (a) filtered JV of the device with relative homogeneous composition, (b)Non-equilibrium QE of M3530. 51

Figure 3.1 (a.1) Raman spectra of the Zn-Cu_2S-S-$SnSe_2$-Se precursor solution, (b.1) real-solution component of the Zn-Cu_2S-S-$SnSe_2$-Se precursor solution, and (c.1) Cu_2S-S-$SnSe_2$-Se mixed solution. $SnSe_2$-Se solution with $SnSe_2$: Se = 1: 1 was used. 200 cm^{-1}, 246 cm^{-1}, 268 cm^{-1} (marked by *) are vibrational modes of the double-centered $Sn_2Se_6^{4-}$ complexes. 335 cm^{-1} (marked by +) is the vibrational mode of Cu-S stretching. 214 cm^{-1} (marked by #) has not been observed from either Cu_2S-S or $SnSe_2$-Se solution. (a.2) XRD patterns of the CZTSSe precursor powder, derived from drying the Zn-Cu_2S-S-$SnSe_2$-Se precursor slurry, (b.2) Zn(Se,S)(N_2H_4) powder, derived from drying the filtered precipitation of the slurry, and (c.2) $Cu_2Sn(Se,S)_x$ hydrazine/hydrazinium powder, derived from drying the real-solution component of the same slurry. 60

Figure 3.2 (a.1) XRD patterns of Cu-Sn-Se-Se precursor powder derived from pumping Cu_2S-S-$SnSe_2$-Se mixed solution for one week, (b.1) (N_2H_4)(N_2H_5) Cu_7S_4 powder derived from pumping the Cu_2S-S solution overnight, (c.1) covellite (reference code 03-065-0603, P63/mmc), obtained by pumping the Cu_2S-S solution for 1 week. (a.2) Raman spectra of Cu-Sn-Se-S precursor film

derived from pumping Cu_2S-S-$SnSe_2$-Se mixed solution for one week and (b.2) $(N_2H_4)_3(N2H5)_4$ Sn_2Se_6 film derived from pumping $SnSe_2$ –Se solution for 1 week. 62

Figure 3.3 TGA of the Cu-Zn-Sn-Se-S precursor powder as it decomposes into $Cu_2ZnSn(Se,S)_4$ and the metal ratio of powder subjected to separated thermal processes with different annealing temperature. 67

Figure 3.4. (a) XRD patterns of dried Cu-Zn-Sn-Se-S precursor, annealed at 100 ℃, 175 ℃, and 250 ℃, as well as (b) at 350 ℃, 450 ℃, and 540 ℃. Peaks marked with # are shared by tetragonal Cu_2ZnSnX_4 and cubic Cu_2SnX_3. Peaks marked with * are unique to tetragonal Cu_2ZnSnX_4. Peaks marked with + are wurtzite ZnX. 68

Figure 3.5 Raman spectrum of Cu-Zn-Sn-Se-S precursor dried, annealed at 100 ℃, 175 ℃, 250 ℃, 350 ℃, 450 ℃, and 500 ℃. Spectra of 1. Cu_2ZnSnS_4, 2. Cu2ZnSnSe4, 3. ZnSe, and 4. Cu_2SnSe_3 are also provided for reference. .. 71

Figure 4.1 The nanocrystal approach enables phase formation to occur prior to film deposition. (a) Schematic illustration of the difference between nanocrystal approach and the others. (b) TEM and HRTEM of the as-synthesis Cu_2ZnSnS_4 nanocrystals. 78

Figure 4.2 Cross-sectional SEM images of annealed films by (a) (b)nanocrystal approach[43], [127] with the EBIC map of the identical area. The dotted lines in (b) are the benchmarks to indicate the same physical location on the sample in each image. Also, cross-sectional SEM images of (c) an organic ink-

processed CIGS film [132] and (d) a hydrazine-processed CZTSSe film[98]. Adapted with permission © 2013 The Royal Society of Chemistry..... 81

Figure 4.3 Configuration of CSS chamber. 84

Figure 4.4 The sketches of typical Planar Type and Inhomogeneous Type morphology and the cross-sectional and planar SEM images of the resulting films of selenization runs I, II, and III. 87

Figure 4.5 The cross-sectional SEM images of the resulting films of selenization runs A, B, C, D; a, b, c, and d. 88

Figure 4.6 XPS depth profiles of a selenized film with bulk composition typical of other works in literature. (a) Peak area corrected for transmission, energy dependence, and RSF of Cu-2p3/2, Zn-2p3/2 and Sn-3d5/3. The arrows indicate where the elements are most concentrated. The margins of large grains/fine grains and $MoSe_2$ were estimated by comparing the depth profiles to SEM cross-sectional images. (b) High resolution scans of the surface region of each absorber layer. (c) The composition Cu*, Zn*, and Sn* profiles of the top ~ 300 nm of absorber. The dotted lines represent the bulk composition acquired by XRF. 93

Figure 4.7 Surface depth profiles before and after selenization. (a)(b) A regular nanocrystal film before and after selenization. (c)(d) An modified nanocrystal film before and after selenization. 94

Figure 4.8 XPS depth profiles of a selenized film with significantly higher Zn content. (a) Peak area corrected for transmission, energy dependence, and RSF of Cu-2p3/2, Zn-2p3/2 and Sn-3d5/3. The arrows indicate where the elements are

most concentrated. The margins of large grains/fine grains and $MoSe_2$ were estimated by comparing the depth profiles to SEM cross-sectional images. (b) High resolution scans of the surface region of each absorber layer. (c) The composition Cu*, Zn*, and Sn* profiles of the top ~ 300 nm of absorber. The dotted lines represent the bulk composition acquired by XRF. 96

Figure 4.9 (a) A Cu-Zn-Sn ternary diagram showing the stoichiometric composition of kesterite (hollow square), the commonly adopted composition in the literature (solid circle), the composition of the best cells in the present study (solid square) and the compositions of several high-efficiency devices reported in the literature (diamonds and hollow circles). (b) The SEM cross-sectional image of the highest performance device cell. (c) Light and dark J-V curves of the highest performance device. Their bandgaps and J-V parameters are listed in Table 4.2. (d) The external quantum efficiency (EQE) spectra of the device. 99

Figure A.1 M3530 a Cu-rich-growth run. 106

Figure A.2 M3512 a Zn-rich-growth run. 107

Figure A.3 M3461 a near-stoichiomtric-growth run. 108

Figure B.1 Raman spectra of (a) $SnSe_2$-Se solution with $SnSe_2$: Se = 1: 1 and (b) Cu_2S-S solution with Cu_2S : S = 1: 2. 109

Figure B.2 Powder XRD pattern of the powder prepared by (a) drying Cu_2S-S and $SnSe_2$-Se mixed solution annealing at 200℃, and (b) filtering and drying CZTSe precursor solution. $Cu_2Sn(Se,S)_3$ or kesterite is marked by “o” (reference code 01-089-2879); $SnSe_2$ is marked by “*” (reference code 00-023-0602);

CuSe is marked by “#” (reference code 00-049-1457); Se is marked by “+” (reference code 00-042-1425); hexagonal ZnX is marked by “@” 110

List of Tables

Table 1.1 A summary of lab-scale and sub-module best efficiencies. For the definitions of efficiency, V_{OC}, J_{SC}, and FF, see Sec 1.4. 6

Table 1.2 A table compare the structural, optical and electrical parameters of kesterite to chalcopyrite (CIGS). 6

Table 1.3 Comparison of the processes 13

Table 2.1 Deposition types and film compositions. 29

Table 2.2 The extracted parameters of the curves shown in Figure 2.7. 40

Table 2.3 Best NREL co-evaporated $Cu_2ZnSnSe_4$ devices within the specified range of composition before AR coating. 42

Table 2.4 J-V parameters of devices, PCE, V_{OC}, J_{SC}, and F.F. Numbers in parentheses are results obtained after annealing bare absorber. 47

Table 3.1 Summary of the crystal structures of several monometallic and bimetallic hydrazine/hydrazinium compounds 66

Table 4.1 Experimental conditions of the CSS selenization runs. 86

Table 4.2 The current-voltage (J-V) parameters of the best device 98

Acknowledgments

The dissertation and the work behind were completed with the selfless support and guidance of many. I would like to express my deep appreciation to them and my sincere wish that even though the dissertation has come to a conclusion our friendships continue to thrive.

First, I owe sincerest thanks to Prof. Yang Yang, my Ph.D. research advisor, for the opportunity to participate in the dynamic and distinguished research of his group. His research guideline of always taking the challenges relevant to real-world issues, including the energy issue motivating this dissertation, has influenced me the greatest. During the years, I have never been short of encouragement, trust, and inspiration from by my advisor, for which I most thank him.

I also would like to thank my committee members, Prof. Richard Kaner, Prof. Eric Pei-Yu Chiou, and Prof. Mark Goorsky, for their mentorship.

I thank Ingrid Repins, my mentor of the research internship at National Renewable Energy Laboratory. The countless long and detailed discussions we had in her office about our projects and also about the device physics of solar cells have been inspiring and extremely useful for my career. I am lucky to meet such a role model in this early stage of my voyage.

I will not forget to thank my dearest partners in the Yang's Lab. Samuel Duan, Brion Bob, Letian Dou, Eric Richard, and Jing Gao joined the research group together with me back in 2009. I am glad that we had the chance to share the joys and hard times together. Renee and Kitty made my process of adapting to a new place and a new culture easy and

enjoyable. William Hou, Peter Li, Bao Lei, Wenbing Yang, and Choong-Heui Chung are first of the many people who guided me to enter the field. Huanping Zhou, Tze-Bing Song, Shenglin Ye, Song Luo, and Yao-Tsung Hsieh contribute tremendously to the nanoparticle project. Especially, the project will not be in shape without Huanping. Chia-Jung Hsu and Samuel Duan, also working on kesterite solar cells, have been extremely supportive.

I also appreciate Rommel Noufi for granting my internship at National Renewable Energy Laboratory. Glenn Teeter, Carolyn Beall, Clay DeHart, Jian Li, Miguel Contreras, Lorelle Mansfield, James Burst and many more have offered valuable technical supports and scientific discussions during my internship. I thank Hsiang-Yu Chen for the hospitality of introducing her friends and more in Denver to me.

I feel grateful to have many caring friends. I particularly thank Kuan-Teh Li for treating my goals like his own, Yu Chen for being not afraid of giving constructive/destructive advices, and Min-Ching Ho for his listening and company.

At last, I thank my parents, my grandparents, my aunt, and my other family members. I would not have reached this step without their belief in me.

VITA

2008	B.S. Materials Science and Engineering, National Tsing-Hua University, Hsinchu, Taiwan
2010	M.S. Materials Science and Engineering, University of California, Los Angeles, CA, USA
2011	Research Intern, National Renewable Energy Laboratory, Golden, Colorado, USA
2009-2014	Graduate Student Researcher, Department of Materials Science and Engineering, University of California, Los Angeles, CA, USA

Publications

Wan-Ching Hsu, Ingrid Repins, Carolyn Beall, Clay DeHart, Bobby To, Wenbing Yang, Yang Yang and Rommel Noufi. Growth mechanisms of co-evaporated kesterite: a comparison of Cu-rich and Zn-rich composition paths. *Progress in Photovoltaic: Research and Application*, **22**, 35 (2014)

Letian Dou, Yonghao Zheng, Xiaoqin Shen, Guang Wu, Kirk Fields, Wan-Ching Hsu, Huanping Zhou, Yang Yang, and Fred Wudl. Single-crystal linear polymers through visible light-triggered topochemical quantitative polymerization. *Science*, **343**, 272 (2014)

Huanping Zhou, Hsin-Sheng Duan, Wenbing Yang, Qi Chen, Chia-Jung Hsu, Wan-Ching Hsu, Chunchao Chen and Yang Yang. Facile single-component precursor for Cu_2ZnSnS_4 with enhanced phase and composition controllability. *Energy and Environmental Science*, **7**, 998 (2013)

Huanping Zhou, Tze-Bin Song, Wan-Ching Hsu, Song Luo, Shenglin Ye, Hsin-Sheng Duan, Chia-Jung Hsu, Wenbing Yang and Yang Yang. Rational Defect Passivation of $Cu_2ZnSn(S,Se)_4$ Photovoltaics with Solution-Processed Cu_2ZnSnS_4:Na Nanocrystals. *Journal of American Chemical Society*, **135**, 15998 (2013)

Huanping Zhou, Wan-Ching Hsu, Hsin-Sheng Duan, Brion Bob, Wenbing Yang, Tze-Bin Song, Chia-Jung Hsu and Yang Yang. CZTS nanocrystals: a promising approach for next generation thin film photovoltaics. *Energy Environmental Science*, **6**, 2822 (2013)

Wan-Ching Hsu, Huanping Zhou, Song Luo, Shenglin Ye, Tze-Bin Song, Yang Yang. Grain Growth of CZTS from Nanoparticle Selenization, *39th IEEE Photovoltaic Specialists Conference*, Tampa, FL. (2013)

Wenbing Yang, Hsin-Sheng Duan, Kitty C. Cha, Chia-Jung Hsu, Wan-Ching Hsu, Huanping Zhou, Brion Bob and Yang Yang. A molecular solution approach to synthesize electronic quality Cu_2ZnSnS_4 thin films. *Journal of American Chemical Society*, **135**, 6915 (2013)

Hsin-Sheng Duan, Kuo-Chun Tang, Wan-Ching Hsu, Brion Bob, Bao Lei, Pi-Tai Chou and Yang Yang. Studies of carrier recombination in solution-processed $CuIn(S,Se)_2$ through photoluminescence spectroscopy. *Applied Physics Letter*, **102**, 063902 (2013)

Wan-Ching Hsu, Ingrid Repins, Carolyn Beall, Clay DeHart, Glenn Teeter, Bobby To, Yang Yang, and Rommel Noufi. The effect of Zn excess on kesterite solar cells. *Solar Energy Materials and Solar Cells*, **113**, 160 (2013)

Wan-Ching Hsu, Ingrid Repins, Carolyn Beall, Glenn Teeter, Clay DeHart, Bobby To, Yang Yang, and Rommel Noufi. Growth kinetics during kesterite coevaporation. *38th IEEE Photovoltaic Specialists Conference*, Austin, TX (2012)

Ingrid Repins, Manuel J. Romero, Jian V. Li, Su-Huai Wei, Darius Kuciauskas, C.S. Jiang, Carolyn Beall, Clay DeHart, Jonathan Mann, Wan-Ching Hsu, Glenn Teeter, Al Goodrich,

Rommel Noufi. Kesterite successes, ongoing work, and challenges: a perspective from vacuum deposition. *IEEE Journal of Photovoltaics*, **3**, 439 (2013)

Huanping Zhou, Chia-Jung Hsu, Wan-Ching Hsu, Hsin-Sheng Duan, Choong-Heui Chung, Wenbing Yang, Yang Yang. "Non-hydrazine solutions in processing $CuIn(S,Se)_2$ photovoltaic device from hydrazinium precursors", *Advanced Energy Materials*, **3**, 328 (2013)

Wan-Ching Hsu, Brion Bob, Wenbing Yang, Choong-Heui Chung and Yang Yang. Reaction pathways for the formation of $Cu_2ZnSn(Se,S)_4$ absorber materials from liquid-phase hydrazine-based precursor inks. *Energy and Environmental Science*, **5**, 8564 (2012)

Ingrid Repins, Carolyn Beall, Nirav Vora, Clay DeHart, Darius Kuciauskas, Pat Dippo, Bobby To, Jonathan Mann, Wan-Ching Hsu, Alan Goodrich, Rommel Noufi. Co-evaporated $Cu_2ZnSnSe_4$ films and devices. *Solar Energy Materials and Solar Cell*s, **101**, 154 (2012)

Brion Bob, Bao Lei, Choong-Heui Chung, Wenbing Yang, Wan-Ching Hsu, Hsin-Sheng Duan, William Wei-Jen Hou, Sheng-Han Li, Yang Yang. The Development of Hydrazine-Processed $Cu(In,Ga)(Se,S)_2$ Solar Cells. *Advanced Energy Materials*, **2**, 504 (2012)

Jun Yang, Jingbi You, Chun-Chao Chen, Wan-Ching Hsu, Hai-ren Tan, Xing Wang Zhang, Ziruo Hong, and Yang Yang. Plasmonic Polymer Tandem Solar Cell, *ACS Nano*, **5**, 6210 (2011)

Chapter 1 Introduction of earth abundant kesterite solar cells

The introduction starts with the natural resource limitation on PV scaling, and explains how kesterite solar cells could be a solution (Sec. 1.1 ~ Sec. 1.2). Later, the current development status of kesterite solar cells and the basic structural, optical, and electrical properties of the kesterite material are then reviewed (Sec 1.3). After a brief introduction of the operation principle of kesterite solar cells (Sec 1.4), the chapter goes into the fabrication processing of the kesterite thin film (Sec. 1.5). Three processes – co-evaporation, hydrazine-based processing, and nanocrystal film selenization – are the main focuses of the thesis and therefore are discussed in better detail in this chapter. At last, to open the discussion in the next three chapters of the thesis, the importance of controlling film composition, secondary phases, point defects, and grain morphology are elaborated (Sec. 1.6).

1.1 Natural resource limitation: the obstacle for PV to meet the growing energy demand

The rapid growth of energy demand is a major challenge of this century. In order to prevent disastrous interferences to global climate and in the meanwhile support the growth of the population and economy, we soon have to restrain the usage of fossil fuel and instead replace with cost effective carbon-neutral energy resources. Just to reach the

less demanding IS92a scenario of carbon dioxide concentration in the atmosphere, 10 TW in the 28 TW of global power demands of year 2015 needs to be supplied by carbon-neutral energy resources. 10 TW is equivalent to the power generated by all resources in combine in year 1998. The required scale is orders of magnitude beyond today's available carbon-neutral resources.[1][2]

Within all the C-neutral energy sources, solar power has the greatest potential to achieve the 10TW goal based on the virtually unlimited amount of sunlight and its accessible distribution compared to the other resources under developing, including wind, geothermal, and sea waves. Photovoltaic (PV) is by far the most mature and fast growing technology to harvest solar power. US Department of Energy (DOE) report indicates that the maximum potential of power production by PV is as high as 7500 TW assuming that the highest efficiency PV devices are used.[2][3]

However, even though the sunlight itself is unlimited, the raw material consisting the PV device to harvest sunlight is not. The commercially available PV panels including crystalline silicon, and thin films (amorphous silicon, CdTe, and CIGS) all use one or more rare elements. For silicon solar cells, the use of silver is the major problem; for CIGS and CdTe, the use of indium and tellurium, respectively. Based on the total reserve of these limiting elements, crystalline silicon, CdTe, and CIGS in combine can only produce no more than 15% of the 10 TW needed by 2050.[4] Apparently, the natural resource limitation is a critical factor in the race of green energy source. The problem has not reflected in the price of solar panels in present stage only because the production scale today (around $50GW_p$[5]) has not even come close to what it will be when 10TW is urgently in need.

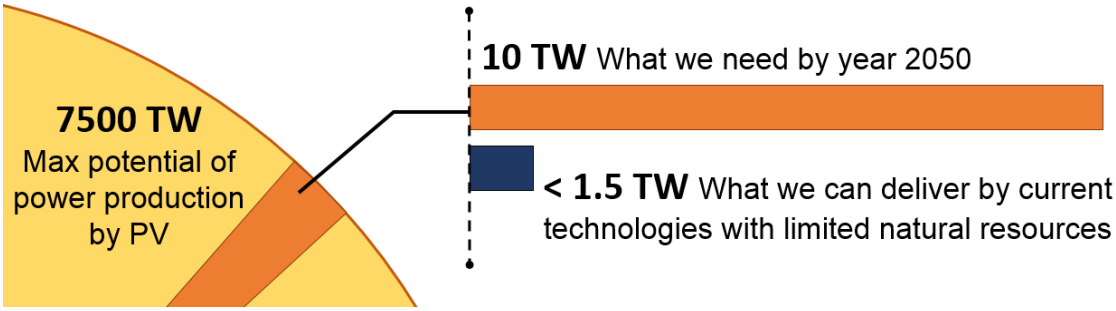

Figure 1.1 The maximum potential of power production by PV is as high as 7500 TW assuming that the highest efficiency PV devices are used. However, only 1.5 TW can be delivered with natural resource limitation based on current technologies, which is only 15% of what we need by year 2050.

1.2 Kesterite: the earth abundant alternative to CIGS solar cells

CIGS has the highest conversion efficiency in the thin-film family both in terms of laboratory-scale cell efficiency and commercially available panel efficiency.[6] The record cell efficiency has just reached 20.8%[7], which brakes the record cell efficiency of polycrystalline silicon solar cell, a moment before the completion of this thesis, rendering the efficiency only second to single crystalline III-V and silicon solar cells. Multiple manufactures have reported panel efficiencies beyond 15%[8][9][6]. Despite the success in performance, the deficient deposit of indium and secondly gallium in the earth crust and their finite production rate will eventually limit the up scaling of the technology. Tao et al[4] estimates, by depleting the earth deposit of indium, the limitation is 816 GWp of CIGS panel based on the existing production technologies, convertible to 100-130 GW of averaged output, which is less than 1.3% of the 10TW carbon-neutral energy source required by 2030.

Kesterite, Cu_2ZnSnS_4, has been treated as a potential earth abundant substitution to CIGS for its multiple similarities in structural, optical, and electrical properties (see Section 1.3). From CIGS (chalcopyrite) to CZTS (kesterite), group III indium and gallium are replaced by group II zinc and group IV tin. The relative abundance of zinc and tin by atom fraction in the Earth's upper continental crust can be found in Figure 1.2 reported by the US Geological Survey[10]. As shown in the figure, zinc and tin are three orders and two orders, respectively, more abundant than indium. By a rough estimation, assuming kesterite may reach the same efficiency as CIGS in the future, based on raw material reserve, we may expect the capacity of kesterite solar cell to be two orders above that of CIGS (100 ~ 130GW averaged power output), which is around 10TW averaged power output and possibly sufficient to satisfy or close to the goal of 2050.

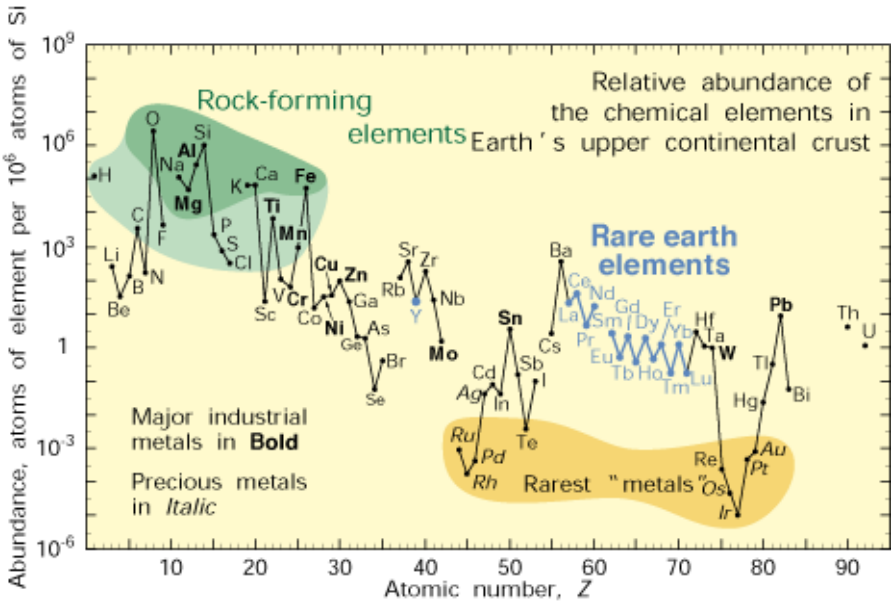

Figure 1.2 The relative abundance of elements by atom fraction in the Earth's upper continental crust according to US Geology Survey.[10]

Based on the confidence and experience gained from CIGS solar cells, the cell efficiency of kesterite has thrived in a rapid pace in the recent years. It is in general optimistic that the efficiency may catch up CIGS in near future. Cell efficiency of 7% - 12% has been realized by multiple processes ranging from vacuum deposition to direct solution casting in laboratory scale (see Sec 1.4). To date, the record efficiency is 12.6% via adirect hydrazine-based solution coating process by IBM T.J. Watson.[11] However, not all of the material developed in these processes are fully earth abundant. Se/S alloys have been often used (see Sec 1.3 and 1.4). Kesterite has also attracted interest of multiple industrial players including Stion, Solar Frontier, and Solexant. A 8.6% sub-module has been reported by Solar Frontier.[12] The up-to-date progress in both lab scale and panel scale are summarized in Table 1.1.

Next, we still have to further improve the small-area cell efficiency to be at least comparable to CIGS, and at the same time seeking fabrication processes with less energy input, lower cost, and higher throughput, in order to bring down the dollar/watt of the technology. Only cost effective carbon-neutral energy resource will be able to replace fossil fuels while maintaining the growth of economic system and population.

Table 1.1 A summary of lab-scale and sub-module best efficiencies. For the definitions of efficiency, V_{OC}, J_{SC}, and FF, see Sec 1.4.

Methods	Compound	Efficiency (%)	V_{OC} (mV)	J_{SC} (mA/cm2)	FF (%)	AR coating	Institute
Hydrazine-based processing	CZTSSe	12.6	513	35.2	69.8	Y	IBM[11]
Nanocrystal-based processing	CZTSSe	8.5	451	28.9	64.9	N	DuPont[13]
Single-step co-evaporation	CZTSe	9.15	377	37.4	64.9	Y	NREL[14]
Two-step evaporation*	CZTS	8.4	661	19.5	65.8	Y	IBM[15]
	CZTS	8.65%	711	20.7	58.7	N	Solar Frontier[12]

* Sub-module.

1.3 The structural, optical, and electrical properties of kesterite

Kesterite is very close to CIGS in terms of both crystal structure, and optical/electrical properties critical for the solar-cell application. In general, the optical properties of kesterite are as superior as those of CIGS, while the electrical properties still need to be improved. A comparison between these properties between the two materials is summarized in Table 1.2.

Table 1.2 A table compare the structural, optical and electrical parameters of kesterite to chalcopyrite (CIGS).

	Compound	Structure	Band gap	Opt. absorp. coefficient	Carrier concentration	Minority carrier lifetime
Chalcopyrite	$Cu(In,Ga)Se_2$	Zinc-blende based	1.05 ~ 1.65 eV[16]	10^{15} cm^{-1}[16]	$10^{15\text{-}16}$ cm^{-3}[17]	50 ~ 500 ns[17]
Kesterite	$Cu_2ZnSn(Se,S)_2$		0.94 ~ 1.45 eV[18] [19]	$10^{14\text{-}5}$ cm^{-1}[19]	$10^{15\text{-}16}$ cm^{-3}[17]	Several ns[17]

1.3.1 Crystal structure and optical properties

The crystal structure of kesterite as well as that of CIGS is based on a II-VI zinc-blende structure. By replacing half of the group II zinc by group I copper, and replacing the other half by group III indium and gallium, the zinc-blende structure becomes I-III-VI_2 or chalcopyrite structure. The chemical formula is Cu(In,Ga)Se_2. By further replacing half of the group III indium by group II zinc and replacing the other half by group IV tin, the chalcopyrite structure becomes I_2-II-IV-V_4, or kesterite structure. The chemical formula is $Cu_2ZnSnSe_4$ or Cu_2ZnSnS_4. The band gaps of I-III-VI_2 and I_2-II-IV-V_4 compound are narrower than those in II-VI compounds, and the resulting optical absorption range leads to better solar-cell performance. An optimized absorber band gap makes it possible to achieve a balance between the output current and voltage of the resulting solar cells. The model of the Shockley-Queisser detailed balance limitation indicates that an optimized band gap is located in the range 1.15-1.35 eV.[20] With a configuration of I_2-II-IV-V_4, kesterite compounds have a naturally suitable band gap. (A summary of the evolution of the electronic structure of multinary chalcogenide semiconductors can be found in a previous publication[21].) The crystal structure of chalcopyrite and kesterite are compared in Figure 1.3.

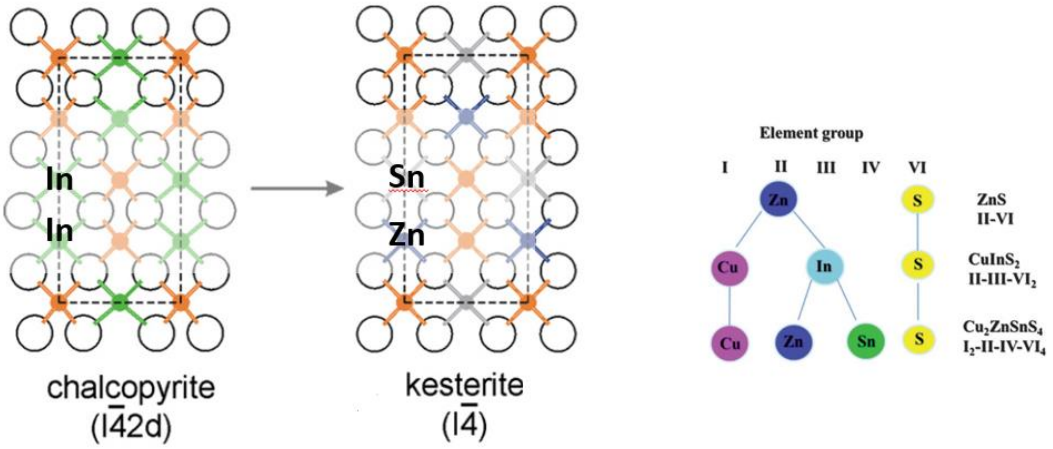

Figure 1.3 Comparison of the crystal structure of chalcopyrite and kesterite. Adapted with permission © 2011 Elsevier.

The band gap energy of kesterite can be further fine-tuned by common group ion substitution. In the CIGS system, common group ion substitution, between S and Se and between Ga and In, is a well-known strategy for optimizing the material's band gap. This approach has also been adapted by the kesterite system. $Cu_2ZnSnSe_4$, Cu_2ZnSnS_4, $Cu_2ZnGeSe_4$, and Cu_2ZnGeS_4 have increasing band gap energies of 0.94 eV[18], 1.45 eV[19], 1.51 eV[22], and 2.27 eV[21], respectively. An optimized band gap energy can be obtained by alloying these kesterite compounds. Another attractive optical property of kesterite is its high absorption coefficient. As a direct band gap material, the absorption coefficient is in the order of 10^{14} cm^{-1}[19], which requires less than 2 µm of absorption length for visible light, while silicon, an indirect band gap material, requires around 100 µm of absorption lengths. The reduction in required absorber film thickness is a key advantage of thin-film solar cells over crystalline silicon solar cells, because of the saving in raw material and, increasingly more importantly, the potential to build devices on light

weight, flexible substrates, especially when the installation labor cost of rooftop solar panels is more than 10% of the total system cost. (According to NREL's report, in 2013 in the US, residential system cost is 4.52/W and the installation labor is responsible for 0.55/W.[23]) Also, flexible substrates also mean that roll-to-roll (R2R or web) fabrication is adaptable, which has significant higher throughput and lower cost than batch-to-batch fabrication.

1.3.2 Electrical properties

Kesterite is a p-type semiconductor doped by intrinsic dopants.[24] First principle calculation based on density function theory shows that Cu_{zn} anti-site point defect has low formation energy and activation energy relative to thermal energy at room temperature therefore, it is probably the major acceptor.[25][26] It has also been suggested that the species of point defects serving as major acceptor is growth condition dependent. For example, Cu vacancies in certain growth conditions may serve as the major acceptor[24].

For solar cell absorber, the following two basic electric properties serve as figure of merit and directly determine the performance of the device: (1) free carrier concentration and (2) minority carrier lifetime.[27][28] Higher free carrier concentration not only results in a Fermi level closer toward the band edge, but also narrows the depletion region, creating a higher electric field across, which reduces the space-charge-region recombination. Longer minority carrier lifetime indicates a lower recombination rate and thus a smaller undesired recombination current. All these effects maximize the built-in potential of a p-n junction and the maximum power output of the device.

The free carrier density of kesterite has been reported in the range of 10^{15} to 10^{16} cm^{-3} and is a function of processing conditions and S/Se ratios.[29][17] The number is close to that of the state-of-art CIGS. The minority carrier lifetime of kesterite is less than 10 ns[30][31][17]. Comparing to the tens nanoseconds[32] and sometimes over 100 ns[17] lifetime of CIGS, the minority carrier lifetime is obvious a major urgent problem for kesterite. The problem of short minority carrier lifetime is shown clearly in the deficit of open circuit voltage (V_{OC}) of the solar cell.[30][33][34] The Eg/q-V_{OC} of CIGS is usually below 0.5V[17], while the number of the best kesterite solar cell is as high as 0.61V[11]. (For the definition of V_{OC}, see Sec. 1.4)

1.4 Operating principles of kesterite solar cells

The most commonly used device structure of kesterite solar cells is identical to that of the CIGS solar cells: a soda-lime glass substrate, a sputtered molybdenum back electrode, a kesterite absorber layer, a chemical-bath-deposited CdS layer, a sputtered resistive/conductive ZnO bi-layer or other transparent conducting oxides as top electrode, and evaporated metal grids (see Figure 1.4).

In operation, a range of solar spectrum is absorbed by the high-absorption-coefficient kesterite layer, where the electron/hole pairs are created. The n-type ITO/ZnO and p-type kesterite introduce a build-in potential by charge transfer to separate these electron and hole pairs and guide them into the top ITO electrode, and bottom molybdenum

electrode, respectively. A band diagram of the whole cell structure is also shown in Figure 1.4.

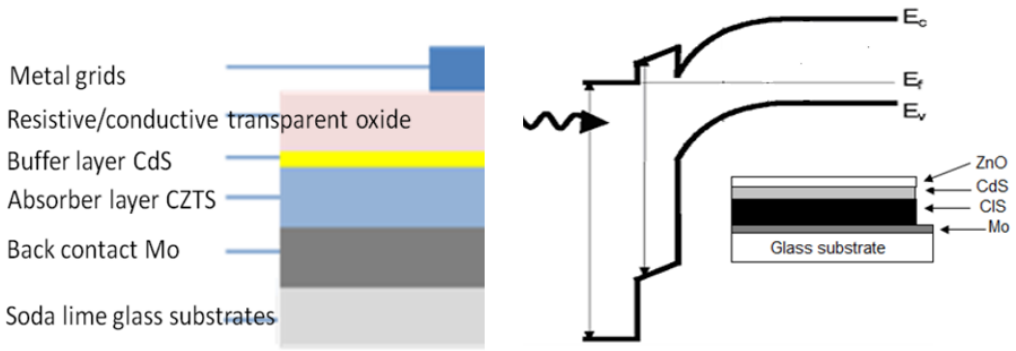

Figure 1.4 Device structure and band diagram of kesterite solar cells

The cell performance is evaluated by power conversion efficiency (PCE).

$$\mathrm{PCE} = \left(\frac{(\mathrm{V} * \mathrm{J}) at \max power\ point}{input\ light\ power\ per\ unit\ area}\right) = \left(\frac{Voc * Jsc * FF}{input\ light\ power\ per\ unit\ area}\right)$$

The maximum power point, open-circuit point, short-circuit point are indicated in a sample current -voltage (I-V) curve shown in Figure 1.5. The open-circuit voltage (V_{OC}) is the voltage at the open-circuit point. The short-circuit current density (J_{SC}) is the current density at the short-circuit point. The Fill Factor is the ratio between V*J at maximum power point and V_{OC}*J_{SC}.

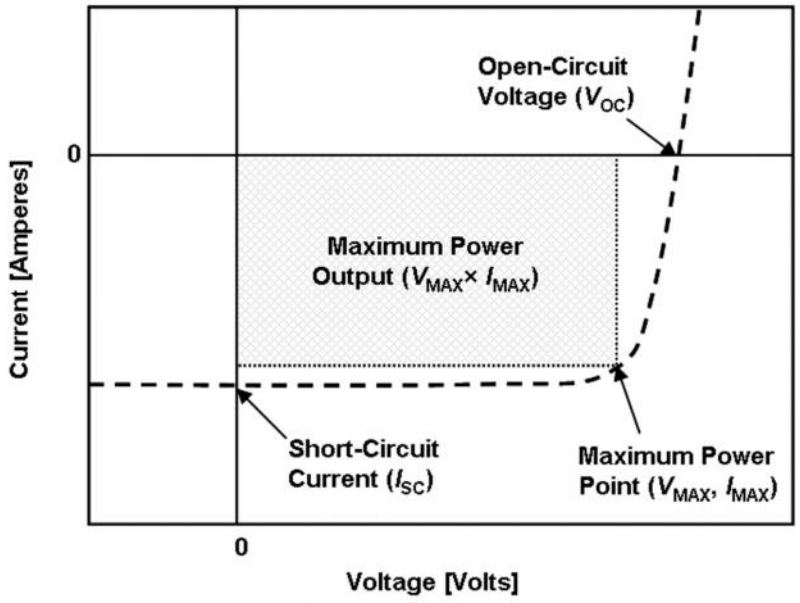

Figure 1.5 A sample current-voltage (IV) curve. I_{SC} = J_{SC} * device area.

1.5 Overview of successful developed processes and recent progress

Table 1.1 summarizes several successful processes for kesterite solar cells, including high-temperature co-evaporation, low-temperature evaporation, molecular-scale solution processing, and nanocrystal films selenization processing. There are many more processes not covered by Table 1.1, including electroplating, sputtering, etc. To help the readers to differentiate these various processes, the below comparisons are provided in Table 1.3. Also, detailed descriptions are given for the three processes involved in this study, co-evaporation, hydrazine-based solution processing, and nanocrystal film selenization.

Table 1.3 Comparison of the processes

	Single-step	Two-step
Vacuum-phase deposition	***Co-evaporation***[14] ***(9.15%)***	Low-temperature evaporation[15][35][36](8.4%) Sputtering[37][38][39](8.4%)
Liquid-phase deposition		***Hydrazine-based processes***[40][34][11][41][42]***(12.6%)*** ***Nanocrystal-based processes***[43] [13][44][45][46]***(9.85%)*** DMSO-based processes[47][48] (8.3%) Ethanol/water-based processes[49][50](5.36%) Electroplating[51](7.3%)

1.5.1 Single step vs two step:

Most of the above mentioned processes are two-step processes, which employ a low-temperature deposition step and a high temperature post-annealing step at atmospheric pressure. For most cases, the second annealing step is carried with presence of chalcogen vapor. The reasons behind this trend will be discussed in Chapter 2.

Co-evaporation, as one of the focus of this dissertation, is an exception. In co-evaporation, the material deposition and the phase formation take place simultaneously in a single step on a high-temperature substrate. In details, metals and chalcogens, Cu, Zn, Sn, Se/S are thermally evaporated and condensed on a substrate. The temperature of the substrate is set around 500˚C, which is high enough for the immediate formation of kesterite. Up to date, co-evaporation is the only processing capable of producing record-

efficiency CIGS solar cell in the last 20 years [52]; in the industry, multiple companies[53] have adapted co-evaporation and produced products in the market. However, the cost of co-evaporation of CIGS is often considered higher than the two-step sputtering technique, which has been widely accepted as a standard tool in various semiconductor industries[53].

1.5.2 Vapor phase vs liquid-phase deposition

The thin-film deposition techniques can be also divided into two categories. One is the vapor-phase deposition, such as evaporation and sputtering. The other is the liquid-phase deposition by spin coating, blade coating, slut coating, or spray coating. In addition to the vapor-phase co-evaporation deposition, this thesis also heavily involve two liquid-phase depositions, hydrazine-based and nanocrystal-based depositions.

A drawback of all the vapor-phase depositions is the requirement of high vacuum (at least 10^{-6} Torr) to provide long mean free path for the vapor atoms to insure a reasonable material utilization rate.[54] The high requirement on vacuum level boosts the capital investment in equipment and the input electricity. These investments eventually add up to the cost/watt of the products.

1.5.3 Molecular-scale solutions vs nanocrystal inks

The first step to develop a liquid-phase deposition technique is to invent a homogeneous and processible ink, either fully dissolved real solution or a colloidal suspension or even the mixture of the two.

In the hydrazine-based processing, hydrazine is used as a solvent to either totally dissolve the binary chalcogenide or disperse the metal chalcogenide-based nanoparticles. After casting the films, a subsequent thermal treatment is required but not necessary with chalcogen vapor. As solution-based, the hydrazine-based processing eliminates the need of high vacuum during film depositions. However, the highly explosive and toxic properties of hydrazine has kept the process from being scaled up.

In nanocrystal-based processing, a different strategy is adapted to create a processible homogenous ink. Instead of attempting to fully dissolving binary precursors, carbon-chain capped nanocrystals are synthesized and dispersed into organic solvents. In this way, large quantity of carbon is introduced into the system but aggressive solvents such as hydrazine can be avoided.

1.6 Influential factors to improve device performance

Various influential factors for kesterite cell performance have been discussed in the literature, such as band gap engineering[55][56], role of S/Se ratio[57], sodium doping concentration[58][59], conduction band offset between the kesterite layer and CdS layer[60][61][62], and molybdenum back contact properties[63][64]. Here, the importance of film composition, secondary phases, point defects, and grain morphology are highlighted, not only because these factors are highly related to the scope of the thesis, but also because they are considered some of the most important factors.

Previous studies[65][66][67] have shown clearly that the device performance of kesterite solar cell significantly depends on the film composition. Composition control is critical and nontrivial because kesterite is a quaternary compound (or even 5-elements counting both sulfur and selenium). More elements are involved, more possible secondary phases and more species of point defects may be introduced.

1.6.1 Composition and secondary phases

Even though kesterite and CIGS structures are both based on the zincblende structure, kesterite is known to be less tolerable in composition. It exhibits only a small single-phase region in the equilibrium phase diagram, according to experimental[68] and computational[26] results. Venturing out of this region leads to the formation of numerous binary and ternary phases such as $Cu_{2-X}S$, ZnS, SnS_x, and Cu_2SnS_3, or their selenide counterparts. Cu_xSe_y or Cu_xS_y is notorious as semi-metallic phases which creates shunting paths for the device. The effect of Cu_2SnSe_3/Cu_2SnSe_3 and $SnSe_x$/SnS_x and are relatively unclear, but since they have a smaller band gap than kesterite, presumably the existence of these phases may reduce the V_{OC} of the device. ZnSe/S has a higher conduction band and a lower valance band compared to kesterite, which indicates carrier blocking and increased resistance.[69] Some of these secondary phases have been observed in kesterite near the back molybdenum contact and considered responsible for large current loss of the device.[63]

However, there exist some inconsistency among the studies discussing the effect of ZnSe/ZnS. In a study[69], a reduction of cell efficiency by half has been ascribed to 24 volume % of ZnS in the Cu_2ZnSnS_4 absorber. While a large amount of ZnS has also been

observed on the back of an 8.4% Cu_2ZnSnS_4 solar cell[15] and was thus deemed electrically unimportant. Also, most studies to date, including all of the studies summarized in Table 1.1 and Table 1.3, have found their most efficient cells at compositions around Cu/(Zn+Sn)=0.9 Zn/Sn=1.25 and along the line between kesterite phase and ZnX phase in the CuX-ZnX-SnX_2 (X=S or Se) ternary phase diagram.[65] This statistical observation indicates that the ZnSe/ZnS is relatively benign. Considering the discrepancy within the literature, more specific criteria for the presence or lack of ZnSe/ZnS in efficient kesterite devices are desired.

1.6.2 Composition and point defects

In addition to the introduction of secondary phases, non-optimized composition also favor the formation of undesirable point defects. Because of the large number of elements involved in the system, there are numerous combinations of add atom, vacancies, and anti-site atoms. Particularly, Cu^+ and Zn^{2+} are isoelectric, so the inter-occupation of these two species of atom only required minimal of formation energy, rendering a high population of these anti-site defects. The activation energies of low-formation-energy defects have been extensively studied through first-principle studies to decide if they are benign or detrimental for device performance.[70][24][71][26][25][21] Multiple studies have agreed that energy level of Cu excess and Sn excess point defects locate deep inside the band gap and therefore considered as harmful recombination centers. Since the formation energies of these point defect are functions of material composition (chemical potential environment), undesirable defects may be avoided by moving toward Cu-poor, Zn-rich, and Sn-poor direction, which is consistent with the empirical sweet spot for device

performance previously mentioned. Figure 1.6 shows that the defect formation energy is a function of chemical potential and also shows the activation energies of the defects [24].

The above discussion on secondary phases and point defects have shone light on the importance of accurate composition control.

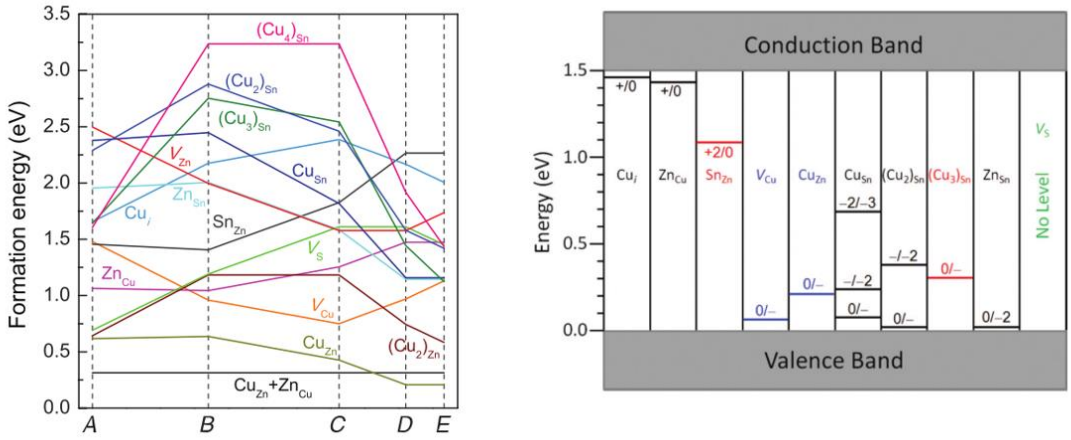

Figure 1.6 The defect formation energies (left) and activation energies (right) are shown here. The defect formation energy is a function of chemical potential. A, B, C, D, and E represent different chemical potential, i.e. different composition. Refer to the original publication for the exact definitions. Duplicated with permission from Physical Review B.[24] Adapted with permission © 2013 American Physical Society.

1.6.3 Grain morphology

Micron-scale grain size is required to avoid excessive recombination and carrier scattering from the boundaries between nanocrystals. Based on previous experience with CIGS, only films with micron sized grains have a chance to produce cells with reasonable power conversion efficiencies. Current progress on CZTS nanocrystal based solar cells has demonstrated that without a grain-growing thermal annealing step, solar cells are generally unable to reach 1% efficiency.[72] Therefore, even though the crystal structure of kesterite

has been formed in the as-deposited films, thermal annealing cannot be omitted due to its importance in ensuring grain growth.

In addition to size, voids or pores laterally distributed on the kesterite layer will create shunting paths for the device, which reduces the F.F. and V_{OC} significantly. Therefore, it is important to obtain closely-packed grains for the kesterite layer.

Chapter 2 Co-evaporated kesterite

As mentioned in Chapter 1, the composition and phase control are several of the most important factors which determine the performance of kesterite solar cells. Single-step high temperature co-evaporation is the only process affording a real-time control of composition and phase. However, when it comes to a new material like kesterite, a better understanding of phase evolution is still in need before control methods can be developed, especially when the accuracy is demanding as described in Chapter 1.

In this chapter, the strengths and challenges of composition and phase control for co-evaporation are first introduced (Sec. 2.1). Later, three deposition routes, Cu-rich, Zn-rich, and stoichiometric routes, designed to understand the phase evolution, are defined, and more experimental details are explained (Sec. 2.2). In the later section, the phase evolution is understood and the problem of Cu_xSe_y residual is pointed out for both Zn-rich, and stoichiometric routes (Sec. 2.3). Without eliminating the Cu_xSe_y residual, the resulting devices suffer from a serious shunting problem. A solution is then figured out according to the new understanding of phase evolution. The success of composition and phase control is evaluated by both composition/phase characterizations and the resulting solar-cell performance. In addition, the effect of growth mechanism on grain morphology is also discussed. In another part of the study, co-evaporation was used as a tool to prepare kesterite films with ZnSe secondary phase located in controllable positions. The effect of ZnSe position on device performance is illuminated (Sec. 2.4). Finally, the chapter is concluded and an outlook is given (Sec. 2.5).

2.1 Strengths and challenges of co-evaporation

1.1.1 Real-time composition and phase manipulation

Even though the successful devices are most often made by two-step processing (a low-temperature film-deposition step and a high-temperature phase-formation step at atmospheric pressure (see Section 1.5.1)), the single-step, high-temperature co-evaporation is still attractive for pursuing high cell efficiency for its unique strength. Co-evaporation, distinguishable from all the other available kesterite deposition processes, is the one process allowing the formation of the phases in the film to occur instantly when the materials are deposited. This signature implies that it is possible to manipulate the constitution of the film in real-time, and even design a phase evolution route or composition transition route. This also means that the composition and phase constitution of the film during growth do not have to be identical to those of the end point.

This strength of real-time manipulation has been found effective to make high-performance CIGS solar cells. To yield efficiency higher than 17%, the film composition is intentionally guided into a Cu-rich condition during certain period of the deposition, but in the end guided into an In/Ga-rich condition. For example, for a two-stage process[73], in the early stage, the film is composed of Cu_xSe_y:$Cu(In,Ga)Se_2$, and Cu_xSe_y is believed to conduct liquid-phase assisted grain growth near or above its low eutectic temperature[74], which increases the grain size and improves the device performance. In the later stage, the film composition is brought back to slightly Cu-poor by applying In/Ga rate only. Therefore, the presence of detrimental Cu_xSe_y at the end of deposition can be easily avoided. (For the detrimental effects of Cu_xSe_y, see Sec. 1.6.1.) This manipulation on film

composition has increased the grain size of the film from hundred nanometers to micron meters to assure there are no grain boundaries lying vertical to the carrier transport direction even when slightly lower substrate temperature was applied. Moreover, a three-stage process[75] which is extensively modified from two-stage process, creates a Ga/In gradient by inserting another In/Ga-rich stage in the beginning of the process. The Ga/In gradient produces a conduction band gradient, which introduces an electric field assisting the separation and the collection of carriers. Both V_{OC} and J_{SC} are increased as a result.[76][77] Three-stage co-evaporation has been continuously setting new record efficiencies for more than 20 years[52] and by far still holds the device performance record for CIGS solar cells.[78]

Inspired by the Cu-rich growth strategy of co-evaporated CIGS, a previous work has taken the same strategy to work on kesterite co-evaporation, based on the assumption that grain size and device performance will be improved when a Cu-rich growth is taken. A high cell efficiency of 9.2% has been achieved.[14] However, the actual phase evolution and its effect on grain morphology and device performance remain unclear. Also, other potentially beneficial deposition strategies which start from different initial composition while approach the same end-point in the end of deposition, have not been explored. One of the motivations of this work is to utilize the strength of the co-evaporation processing to explore different deposition strategies, and also to improve the understanding on the phase evolution in these different deposition routes.

Our knowledge on kesterite co-evaporation to date is summarized as follows. Redinger et al. investigated the substrate temperature range of 325℃-525℃ with selenium partial pressures up to $4x10^{-6}$ Torr, and pointed out the difficulty of low sticking

coefficients, especially for Sn[36]. Briefly, high selenium pressure enhances the sticking of Zn and Sn, but even with high selenium pressure, the sticking of Sn still requires a period of incubation time. In this incubation time, ZnSe and Cu_xSe_y are accumulated to allow the incident Sn to form kesterite instead of $SnSe_x$. The $SnSe_x$ is highly volatile and will be re-evaporated if it does not form kesterite.[80] NREL's study was done at substrate temperatures around 500℃ with a significantly higher selenium partial pressure ($8x10^{-5}$ Torr).[14] Under these conditions, $Cu_2ZnSnSe_4$ is stable, but Se, $SnSe_x$, and Cu_ySnSe_z either evaporate (Se and SnSe) or decompose into gaseous phases ($SnSe_2$ and Cu_ySnSe_z. The later decomposes into Cu_xSe_y and gaseous SnSe and Se).[36] When co-evaporating only Sn and Se at such temperatures, no material sticks to the substrate. When co-evaporating Cu, Sn, and Se, under such conditions, the deposited film is composed of only Cu and Se.[14] These observations indicate that the constitution of the co-evaporated film should be much simpler than that of the two-step processes, due to the absence of a number of unstable phases including Se, SnSe, $SnSe_2$, Cu_2SnSe_3, and Cu_4SnSe_4. In the 500℃ co-evaporated film, there can exist only ZnSe, Cu_xSe_y, and $Cu_2ZnSnSe_4$. This simple constitution is more likely to allow clear in-situ monitoring and feedback control of composition and phases, similar to what has been done widely for the co-evaporation of CIGS [81][82][83].

1.1.2 Difficulty of composition control by co-evaporation for kesterite

As discussed (Sec. 1.6), sensitive composition control for kesterite is critical to obtain high-performance devices. However, precise control is actually not straight-forward

for co-evaporation, due to limited accuracy of deposition rate control and/or the volatile nature of the numbers of elements and precursor phases.

A fairly good control has been found doable in the two-stage and three-stage co-evaporation of CIGS. Precursor phases Cu_xSe_y form in the Cu-rich stage, and since Cu_xSe_y has high emissivity due to its high hole concentration, the substrate temperature drops in this stage. Consequently, in the final stage, in which only In/Ga are deposited, the consumption of Cu_xSe_y can be in-situ observed by watching the recovery of the substrate temperature. It is known to us that once we saw the temperature has fully recovered and leveled off, the film has reached the right composition and the deposition is done. A typical logged substrate temperature in a three-stage CIGS co-evaporation can be found in Figure 2.1. An alternative method to temperature reading is the direct detection of IR emission by pyrometer.[84]

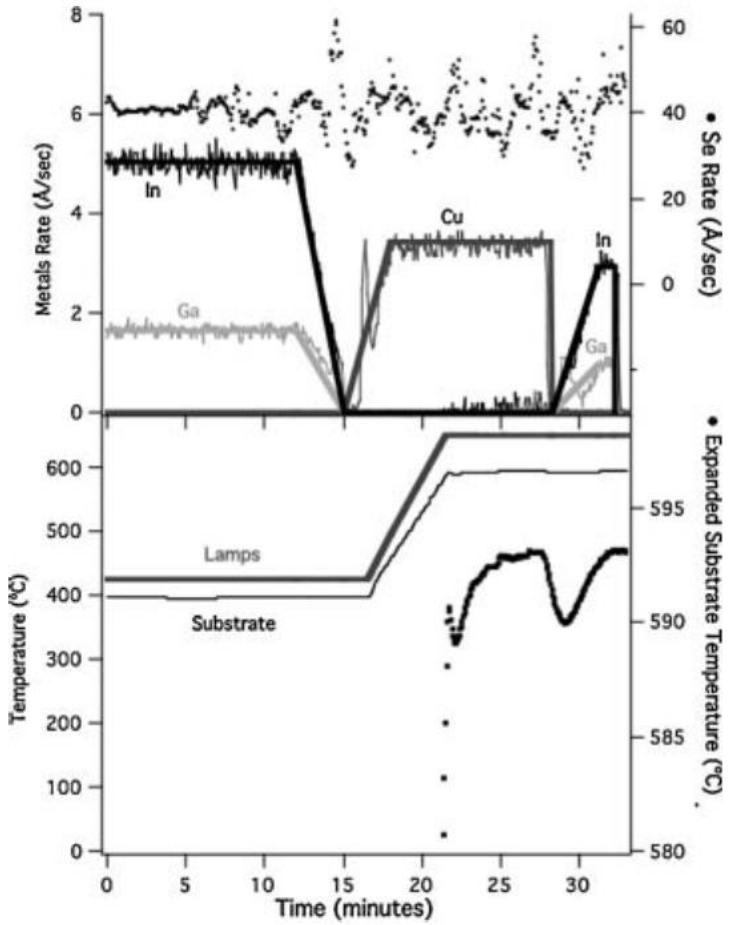

Figure 2.1 The logged deposition data of the co-evaporation run which yields a 19.9% CIGS solar cells.[79]

In the previous work of co-evaporated kesterite, which again adapted the Cu-rich growth strategy, the trick of temperature watching has been utilized to detect the suitable endpoint of a deposition which assure the production of Cu_xSe_y-free films. However, the correlation between the existence/absence of Cu_xSe_y and the drop/recovery of substrate temperature has not been experimentally established for kesterite co-evaporation as it was for CIGS. More importantly, it is not clear if composition control can be done effectively when other deposition strategies, such as Zn-rich growth or constant-rate growth, are taken.

2.2 Experimental methods

In this study, film growths starting from three different composition are investigated: a Cu-rich composition (Cu/Zn > 2), in which $Cu_2ZnSnSe_4$ is presumably evolved from Cu_xSe_y:$Cu_2ZnSnSe_4$, and Zn-rich composition (Cu/Zn around or < 1), in which $Cu_2ZnSnSe_4$ is presumably evolved from ZnSe: $Cu_2ZnSnSe_4$, and a constant composition which equals to the endpoint composition. The goal is to develop composition control methods which is precise enough to obtain high performance device for all three growth strategies. Also to understand the phase evolution during the growths. Each growth mechanism is analyzed by examining films obtained from a number of interrupted depositions, as well as by observing small variations in the substrate temperature in real time.

2.2.1 Film growth strategies

Kesterite depositions were conducted by four-source co-evaporation. Cu, Zn, Sn, and Se were deposited on 3 inch x 3 inch soda-lime glass (SLG) substrates, which were coated with a 1 μm sputtered Mo back contact and a 150 Å e-beam evaporated NaF precursor prior to absorber co-evaporation. During co-evaporation, the lamp temperature used to heat the substrate was set to a constant value, 555℃, until cooled down. The substrate temperature was measured and recorded in real time throughout the depositions. Films T1, T2, and T3 were deposited by recipes respectively belonging to the Type I Cu-rich growth, Type II Zn-rich growth, and Type III constant-rate growth. The deposition

time was around 25 minutes in total, giving a film thickness of roughly 1.6μm. The average total deposition rate was therefore about 10 Å/sec.

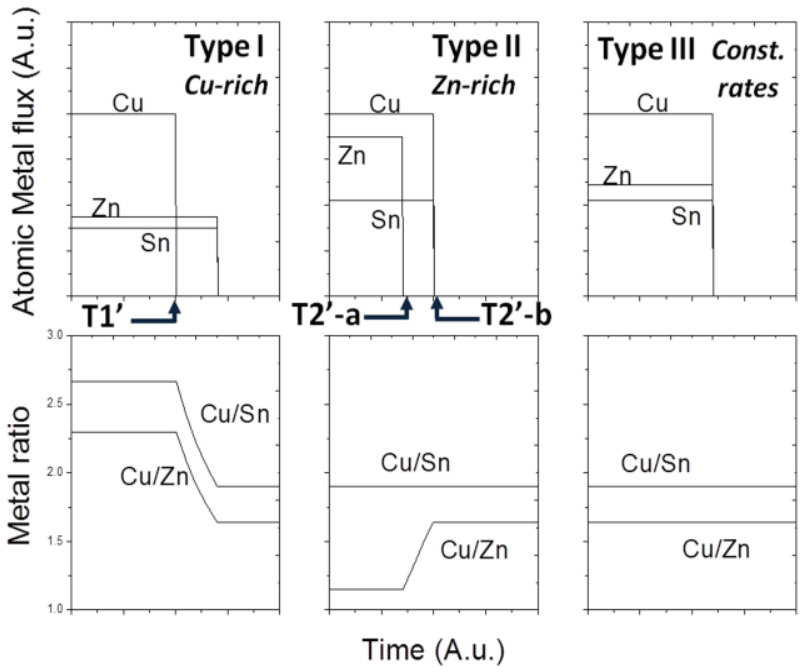

Figure 2.2 Three types of deposition recipes: type I starts Cu-rich, type II starts Zn-rich, and type III maintains constant rates throughout. The deposition rates in atom/unit time shown here are not precise numbers.

Figure 2.2 gives an idea of the major difference between the three deposition strategies. The top diagrams present the relative atomic deposition rates of metals versus time. The real-time film composition calculated based on these deposition rates are shown in the bottom. In each deposition, the films start from a different initial composition without moving the endpoint composition. For Type I, the deposition starts with high Cu rate, yielding a Cu-rich initial composition compared to Zn (Cu/Zn > 2). For Type II, a high initial Zn rate is applied, causing the initial composition to be Zn-rich compared to Cu (Cu/Zn close to or < 1). For type III, metal fluxes are constant throughout the deposition,

to attempt to maintain the endpoint composition throughout the film growth. By turning the initially high metal flows off earlier than the initially low metal flows in Type I and Type II depositions, the compositions were brought to Cu/Zn = 1.5 - 1.7, (Cu% = 46 - 47%, Zn% = 28 – 32%, Sn% = 24 - 25%. Se is not included) at the end point of each deposition, which has been empirically determined to produce high performance devices.

Note that the actual deposition recipes applied during cooling down for film T1, T2, and T3, included more details than the simple sketches shown in Figure 2.2. They are summarized as the followings: (1) although an abrupt termination in Sn rate is shown in Figure 2.2, in each actual deposition, the Sn rate was kept on and gradually reduced in careful control as cooling down to prevent either the rejection of Sn or the deposition of $SnSe_x$. (2) The substrate cool-down was paused at 450℃ for 4 minutes in order to replenish possible Sn vacancies. (3) An additional small Zn rate was applied from the beginning of the cool-down until 430℃, which took about 5 minutes. The resulting Zn-rich surface layer does not affect the bulk composition of the films but does enhance the performance of solar cells significantly. The effect of this Zn-rich layer is out of the scope of this paper and therefore evenly applied on every deposition except for the interrupted ones. (4) The selenium rate was kept over-pressured while cooling down. The actual recipes can be found in Appendix A. (The deposition rates shown in Appendix A are in Å/sec, which is different from the atomic deposition rates shown in Figure 2.2.)

Some depositions were performed the same as T1 and T2 but interrupted before the final endpoint composition was reached. The moments of interruption are marked by arrows in Figure 2.2 and the resulting films are named as T1', T2'-a, and T2'-b. At the indicated moments, the following cool-down procedure was applied to best preserve the

state of the film: (1) Zn rate and/or Cu rate were cut off abruptly; (2) the lamp was turned off to quench substrates (down to 300℃ within 5 minutes); (3) Sn rate was turned off at 455℃ substrate temperature; (4) Se rate was gradually ramped down and completely off at 300℃.

The deposition strategies and run record numbers of the films mentioned in this paper are listed in Table 2.1. Film compositions obtained by XRF (calibrated by ICP) are also listed in Table 2.1.

Table 2.1 Deposition types and film compositions.

Completed depositions:

Film No.	Deposition Strategy	Cu/Zn	Cu/Sn	Cu%	Zn%	Sn%	Se%	Run No.
T1	Cu-rich growth	1.71	1.88	22.9%	13.4%	12.2%	51.6%	M3530
T2	Zn-rich growth	1.54	1.93	22.4%	14.6%	11.6%	51.4%	M3512
T3	Constant rates	1.61	1.83	22.5%	14.0%	12.3%	51.2%	M3461

Interrupted depositions:

Film No.	Deposition Strategy	Cu/Zn	Cu/Sn	Cu%	Zn%	Sn%	Se%	Run No.
T1’	Cu-rich growth	2.31	1.88	25.0%	10.9%	13.4%	50.7%	M3529
T2’-a	Zn-rich growth	1.04	2.01	20.2%	19.5%	10.1%	50.2%	M3511
T2’-b		1.88	2.02	23.9%	12.8%	11.9%	51.4%	M3515

2.2.2 Film characterization and device fabrication

The phase components are characterized by Raman spectroscopy equipped with a 514.5 nm argon laser. The emissivity of the co-evaporated films was converted from reflectance measured by UV-VIS-IR spectroscopy. The film morphology and grain size are evaluated based on electron microscopy (SEM) images. The emissivity spectra were acquired by total reflectance measurements, as emissivity = absorbance = 1 – total reflection.

After kesterite deposition, the rest of the device structure is identical to the commonly used structure of CIGS solar cells: a chemical-bath-deposited CdS layer, a sputtered resistive/conductive ZnO bi-layer, e-beam-evaporated Ni/Al grids, photolithographic device isolation, and MgF_2 antireflective coating.

Internal quantum efficiencies (QE_{INT}) were calculated from measuring external quantum efficiency (EQE) and reflectance(R) as EQE/(1-R). The reflectance was obtained from the non-gridded area on samples.

2.3 Phase evolution and composition control

2.3.1 Logged temperature profile and the undesired Cu_xSe_y residual

In the vacuum chamber, since radiation governs the majority of heat dissipation from substrates, subtle changes in substrate temperature are due to changes in surface emission. The emission spectrum is different from that of a black body because of a

combination of factors, including the optical properties of film components, interference fringes at a given film thickness, and surface roughness.

Several logged temperature profiles are shown in Figure 2.3. The left most profile is from a deposition that started Cu-rich, producing sample T1 (deposition M3530). The center profile is from a Zn-rich deposition, producing sample T2 (M3512). The right profile is from a deposition made with all rates held constant, producing sample T3 (M3461). The solid arrows indicate the turn-off time for the Cu source and the dashed arrows indicate that of Zn. The interruption times that produced T1', T2'-a, and T2'-b are also noted.

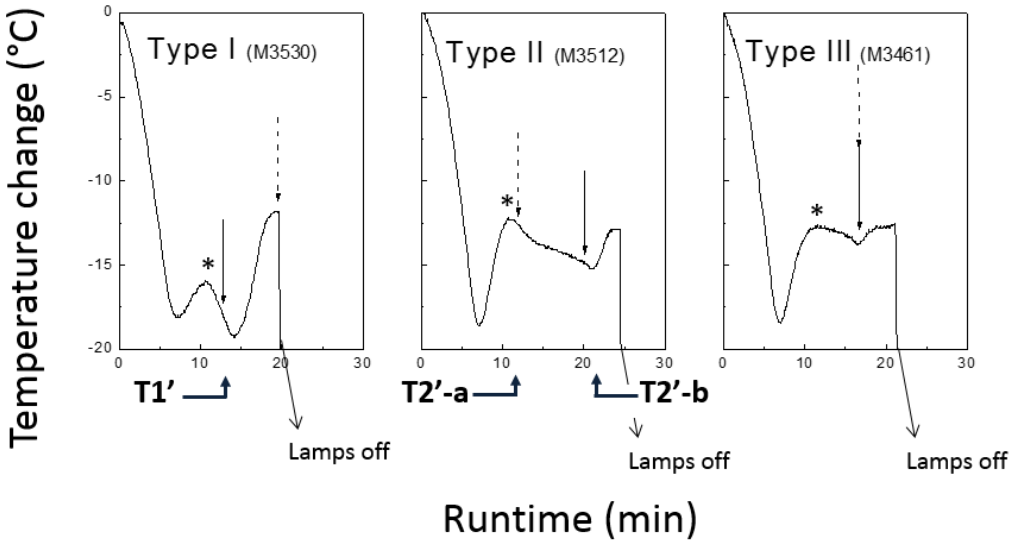

Figure 2.3 Logged temperature profiles of type I (Cu-rich), II(Zn-rich), and III(constant rate) films. Samples T1, T2, and T3 are the products of these depositions, respectively. The interruption times of T1', T2'-a, and T2'-b are also indicated in the figure. In each completed deposition, we waited for the temperature to become level before we started to cool down the substrates. The solid arrows indicate the turn-off time for the evaporation rate of Cu and dashed arrows indicate that of Zn. The temperature of the second turning points marked as "*" is strategy-dependent.

In the early part of the deposition (true for all profiles as well), the substrate temperature undergoes one large drop and two turning points before any metal evaporation rate has been adjusted. The large drop in substrate temperature signals the sample surface changing from the low emissivity of Mo to the higher emissivity of mixed phase semiconductors. The interpretation of the following two turning points remains unclear at this moment but the exact position of the turning point marked by "*" appears to be metal evaporation rate-dependent. This turning point occurs at a lower temperature in Type I and a higher temperature in Types II, and III. It is possible, with further investigation, that the shape of the substrate temperature profile be related to the deposition rate and therefore may become a useful supplement to existing rate monitors. Deeper discussion is out of the scope of the study and will not be discussed in this dissertation. In the later part of the deposition, after the turning point marked by "*", the temperature profile becomes quite meaningful in signaling in-situ film composition and phase constitution.

The behavior of substrate temperature in ***the Cu-rich Type I growth*** nicely follows the previous experience of CIGS co-evaporation. The substrate temperature sinks almost 20℃ compared from the initial temperature and later recovers by roughly 10℃ and subsequently levels off starting few minutes after the Cu rate is turned off. The temperature recovery indicates a reduction in surface emission, a typical symptom of Cu_xSe_y consumption. Several evidences of the existence and consumption of Cu_xSe_y have been acquired by interrupting the deposition before the substrate temperature fully levels off, and comparing the resulting T1' film to the ending film T1. (1) XRF measurement indicates that the composition changes from obviously Cu-rich (Cu/Zn =2.31) to slightly Cu-poor (Cu/Zn =1.71) from T1' to T1. (See Table 2.1) (2) Raman spectroscopy shows the existence

of $Cu_{2-x}Se$ in T1' film but the absence of Cu_xSe_y in T1 film (as shown in Figure 2.4). (3) If the deposition is interrupted before the substrate temperature fully levels off, the resistance of the resulting film measured by two-point probes will be as small as a few ohms, a typical symptom of Cu_xSe_y remaining. Also, the reduction in emissivity detected in real time during the deposition has been confirmed by ex-situ measurements. Figure 2.5 shows emissivity as a function of wavelength as deduced from total reflection measurements for several films in the study. As indicated, the Cu-rich T1' has a higher emissivity compared to the ending film T1. Therefore, it is believed that the final temperature recovery and fully level off is a behavior of emissivity reduction which signals the existence and the consumption of Cu_xSe_y. Consistently, if the Cu rate is not turned off, the substrate temperature decreases even more and never recovers.

On the other hand, the Zn-rich growth (Type II deposition) and the near-stoichiometric growth (Type III deposition) act different than expected.

For Zn-rich growth (Type II deposition), at the point the Zn-rate is shut down, the composition is ultra Zn-rich and Cu-poor as planed to be (the composition of film T2'a is Cu/Zn=1.04, Cu/Sn=2.01). With this composition, Cu_xSe_y was not expected. Surprisingly, Raman spectroscopy and SEM images found that at this point, the film is composed of Cu_xSe_y together with ZnSe and kesterite. T2'-a film exhibits clear $Cu_{2-x}Se$ characteristic Raman peak as shown in Figure 2.4. ZnSe (250 cm^{-1}) Raman peak is not apparent, since the 514.5 nm laser only has limited penetration depth, and according to SEM images of T2'-a (shown in Sec. 2.3.2), ZnSe is located on the bottom of the film and therefore not detected by Raman. After Zn rate is shut down, the substrate temperature goes down, which supports that the unexpected Cu_xSe_y does continue to exist in the ultra Zn-rich film while

exposing to incident Cu. After continuing supplying Cu and Sn rate for another ~5 min, the composition arrives at the endpoint Cu/Zn ratio (the composition of film T2'b is Cu/Zn = 1.88, Cu/Sn=2.02). And the substrate temperature has sunk to 15℃ less than the initial temperature and will sink continuous and never recover if the deposition continues. Raman spectroscopy has shown no $Cu_{2-x}Se$ characteristic peak but it is convincing that a small amount of Cu_xSe_y must exists since the substrate temperature has never recovered and devices made from the films of this stage suffered from serious leakage. The temperature decreases after the Zn rate is turned off is milder in ***near-stoichiometric growth*** (Type III, Figure 2.3c), suggesting a smaller amount of Cu_xSe_y. By **neither** Zn-rich growth nor near-stoichiometric growth, one can obtained $Cu_{2-x}Se$-free film even though the composition may be controlled more or less around the target.

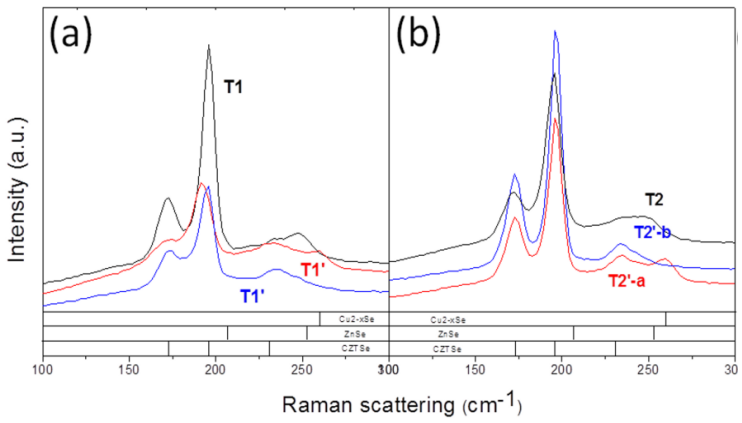

Figure 2.4 (a) Raman spectrum of two different spots of on T1' (in red and blue) and T1 (in black) (b) Raman spectrum of T2'-a (in red), T2'-b (in blue), and T2 (in black).

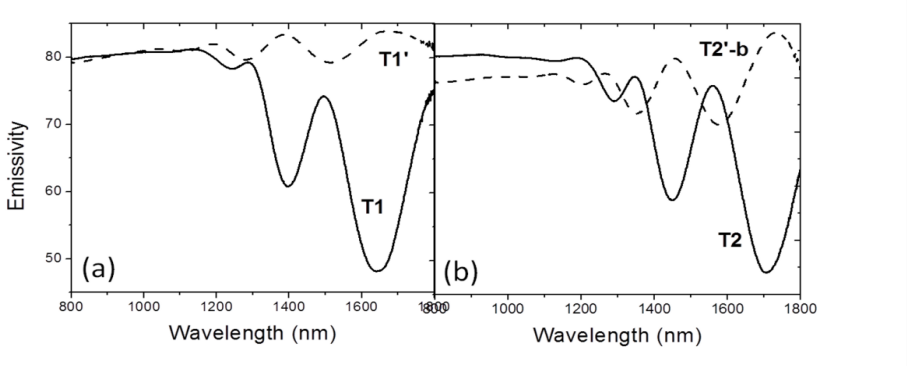

Figure 2.5 Emissivity of (a) film T1' (dashed line) and T1 (solid line) and (b) T2'-b (dashed line) and T2 (dashed line).

2.3.2 Solution to consume Cu_xSe_y residual and the discussion of its origin

A solution has been found to consume these residual Cu_xSe_y in Zn-rich Type II and near-stoichiometric Type III depositions. The depositions were not ended immediately after the endpoint Cu/Zn composition was achieved but kept at high temperature with Sn flow constantly applied. A recovery of substrate temperature then occurs. The composition of T2 is on the target (Cu/Zn=1.54, Cu/Sn=1.93 shown in Table 2.1). The phase constitution is kesterite and ZnSe according to Raman spectroscopy (shown in Figure 2.4). Ex-situ measurements (Figure 2.5) once again confirm the real-time temperature profile: the emissivity of T2 (after Sn soaking) is indeed reduced compared to that of T2'-b (before Sn soaking). This effect of Sn soaking makes us believe that the formation of kesterite is delayed by the difficulty in incorporating Sn during deposition. Experiments have also shown that this delayed reaction cannot be mitigated simply by raising the Sn rate by 1.5x. Providing enough time for the film to be soaked in Sn vapor at high temperature is essential to allow the reaction to complete.

Based on these observations, two candidates are suggested for the bottleneck in the reaction. First, since $SnSe_x$ is a volatile phase at the deposition temperature, Sn will stick only if the Sn atoms encounter Zn and Cu, leading to the immediate formation of kesterite before desorption. The sticking is presumably not as efficient as that of Cu and Zn, which have non-volatile binary phases. Second, kesterite formation might also be limited by the Zn diffusion rate. Depositions stopped earlier in the Zn-rich stage produced films with continuous layers of ZnSe on the bottom (see the Sec. 2.3.5). The required diffusion path of Zn to meet the freshly-deposited Cu is the entire micron-scale film thickness, and may be slow enough to allow for the existence of residual Cu_xSe_y during the Zn-rich growth, rendering a severe temperature reduction. During the near-stoichiometric constant-rate growth, instead of being buried on the bottom of the film, Zn atoms arrive together with Cu atoms, and presumably are able to react more quickly. As a result, the temperature reduction is shallower than in Zn-rich growth. By shutting the Cu rate off and keeping substrates at high temperatures with a Sn rate applied in both Zn-rich and constant-rate growths, both the diffusion of Zn and the incorporation of Sn are given extra time to occur, and therefore the Cu_xSe_y is consumed accompanied by the recovery of the measured substrate temperature.

T2'-a, and T2'-b are also indicated in the figure. In each completed deposition, we waited for the temperature to become level before we started to cool down the substrates. The solid arrows indicate the turn-off time for the evaporation rate of Cu and dashed arrows indicate that of Zn. The temperature of the second turning points marked as "*" is strategy-dependent.

2.3.3 The phase evolution

In Sec 2.3.1 and Sec 2.3.2, the composition and phase constitution in different growth strategies have been traced by ex-situ Raman and composition measurements of the films made by interrupted depositions and finished depositions. It is now realized that kesterite has been formed early in the deposition and shows discrepancy with Redinger et al's observation[36] that Sn cannot be deposited at all at this substrate temperature. The largely increased selenium partial pressure, which facilitates the formation of kesterite, is likely the critical difference between the two studies. In addition, the unstable phases SnSe, $SnSe_2$, Cu_2SnSe_3, and Cu_4SnSe_4 are indeed not observed by Raman spectroscopy. The actual phase evolution of Cu-rich growth and Zn-rich growth can be summarized as followed.

For Cu-rich growth: the film (T1') is Cu-rich and composed of kesterite and Cu_xSe_y at the point the Cu rate is turned off. It is also laterally inhomogeneous. In some spots, only a series of kesterite peaks is observed as in the blue curve of Figure 2.4(a). In other spots, the main 196 cm^{-1} kesterite peak shifts left[85][86], possibly as result of variation in localized surface composition. As the film is converted from Cu-rich to near-stoichiometric (T1), the kesterite peaks become more intense and $Cu_{2-x}Se$ is consumed. (SEM images are shown in Figure 2.6(a).)

For Zn-rich growth: While Cu_xSe_y is not expected intuitively in Zn-rich growth, the film is actually composed of kesterite, Cu_xSe_y, and ZnSe at the point the Zn rate is turned off. After continue to supply Cu and Sn rates for another ~10 min, the Cu_xSe_y content might has reduced in the film but the Cu_xSe_y + ZnSe → kesterite reaction is subtly

retarded, rendering the film not suitable for solar-cell absorber. After turning Cu rate off and continue to supply Sn rate for ~5 min, the Cu_xSe_y has been fully consumed by reacting with ZnSe and producing kesterite. (SEM images are shown in Figure 2.6(b). With multiple confirmations by EDS, we are convinced that the bright features in the images are grains of ZnSe which appears bright because of charging effect of a less conductive phase.[86])

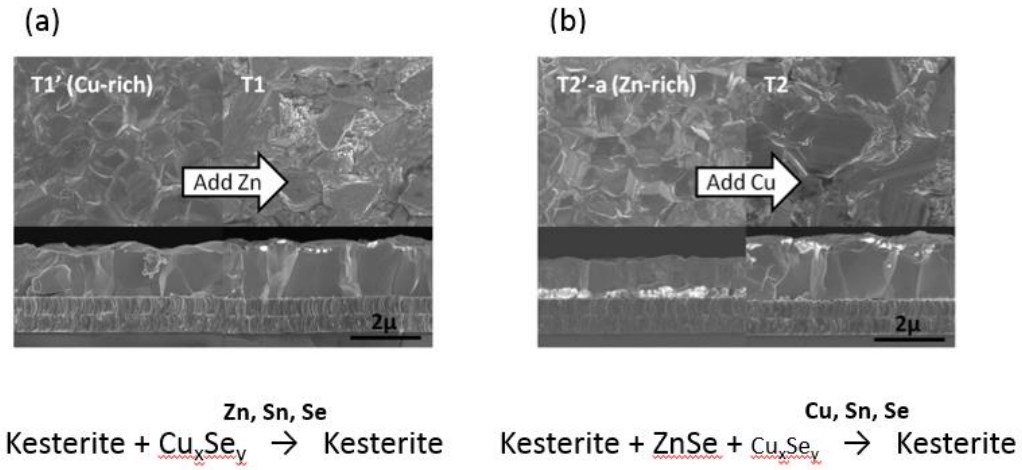

Figure 2.6 Morphology changes (a) from Cu-rich T1' to completed T1 for Type I and (b) from Zn-rich T2'-at to completed T2 of Type II. (Some bright features showing in T1 and T2 on the top of the films are due to the Zn cap applied during cool-down as discussed earlier.

2.3.4 Device performance from different strategies

Over 7.8-9.1% device performance has been obtained by three different processes without detailed optimization. The good device performance indicates that the composition and phase control are precise enough for this level of device performance.

The current density vs. voltage (JV) curves of one of the best devices fabricated by Type I (sample M3490), Type II (M3512), and Type III (M3461) are shown in Figure 2.7. The extracted parameters are given in Table 2.2: power conversion efficiency (PCE), open-

circuit voltage (V_{OC}), short-circuit current density (J_{SC}), fill factor (F.F.), series resistance (R_S), shunt resistance (R_{Sh}), ideality factor (A), and diode saturation current density (J_o).

As shown, the Zn-rich grown M3512 achieved 9.07% cell efficiency (measured in the PV testing group at the National Renewable Energy Laboratory by IEC standard) with 0.420 cm^2 total cell area, much like the 9.05% of the Cu-rich grown M3490, as well as the 9.15% of the reported M3464 in the previous publication[14]. M3512 has nearly identical V_{OC}, R_S, and slightly higher F.F. and smaller ideality factor compared to those of M3490. The lack of substantial deviation in J-V parameters indicates the similarity of these absorbers in terms of optical absorption, recombination losses, and parasitic losses. Constant-rate growth achieved 7.8% cell efficiency without antireflection coating, which is slightly less efficient than Cu-rich and Zn-rich growth. Since no efforts have been put in the optimization of these processes, it is more appropriate leave the question of what deposition route is the best open for now. None of the deposition routes should be excluded from the investigation of co-evaporated kesterite solar cells.

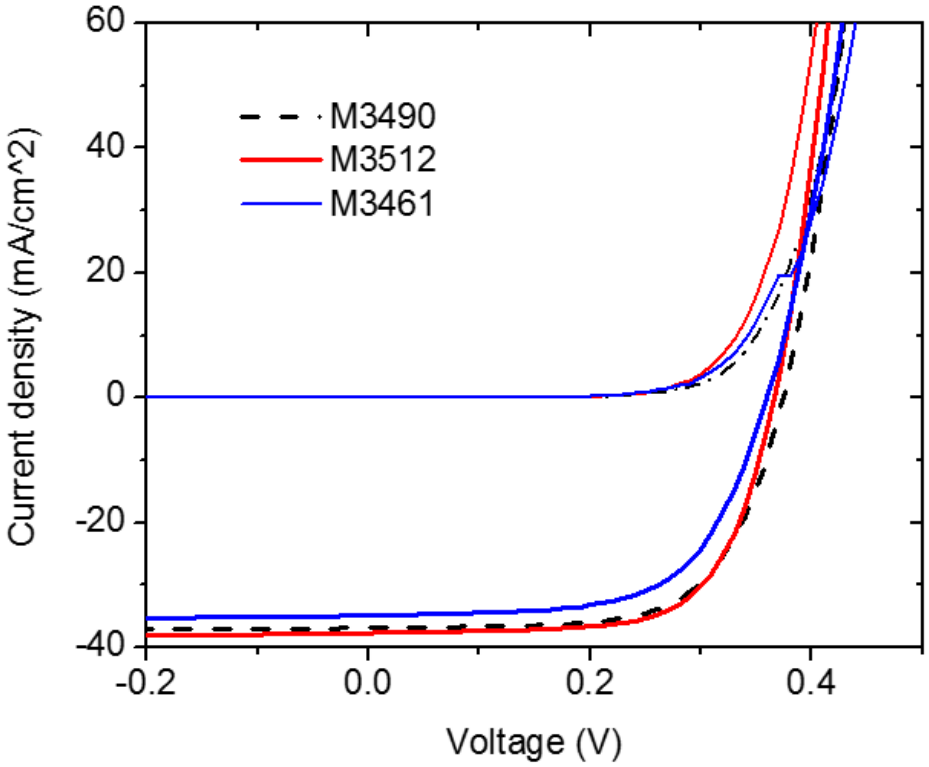

Figure 2.7 The current density vs. voltage (JV) curves of one of the best devices fabricated by Type I (sample M3490), Type II (M3512), and Type III (M3461). Note that M3461 has a lower current because AR coating was not applied.

Table 2.2 The extracted parameters of the curves shown in Figure 2.7.

Deposition route	Run numbers	PCE %	Voc mV	Jsc mA/cm^2	F.F. %
Cu-rich growth	M3490	9.05	375	36.7	65.8
Zn-rich growth	M3512	9.07*	371*	37.1*	67.0*
Near-stoichiometric growth	M3461$^{\#}$	7.86	360	34.9	62.6

* Numbers certified by NREL cell efficiency certification team. $^{\#}$ AR coating not applied.

2.3.5 Effect on grain size

Beyond the SEM images shown in Figure 2.6, within a large quantity (over 10) of films deposited by either type I, II, or III, the correlation of composition (Cu/Zn, Cu/Sn, Cu/(Zn+Sn), or Zn/Sn) to grain size is weak. All these kesterite depositions (around 500

℃) exhibit micron-scale columnar grains. This observation of large grain growth even under Cu-poor conditions does not agree with our experience on co-evaporated chalcopyrite. Chalcopyrite films grown in stoichiometric or indium-rich composition often exhibit sub-micron grain sizes.[87]

The formation of large grains in type I, II, and III depositions would seem to disprove the role of Cu_xSe_y in kesterite grain growth. However, we have shown that the existence of Cu_xSe_y is a general phenomenon in each deposition strategy due to the delayed reaction with ZnSe. This observable amount of Cu_xSe_y may naturally assist the grain growth even in non-Cu-rich conditions, and as a result, films deposited by different strategies do not exhibit diversity in grain size. Consistent with this hypothesis, in Tanaka et al's study[66], an obvious grain size dependency on composition from Cu/(Zn+Sn)=0.82-1.06 was observed for 500℃ co-evaporated $CuZnSnS_4$ with a deposition rate about 30 times lower than ours. The significantly longer reaction time may have allowed Cu to form kesterite with minimal formation of localized Cu_xSe_y, thus forming larger grains only when more Cu is present.

2.4 Effect of ZnSe distribution on device performance

As discussed in Sec 1.6, considering the discrepancy within the literature, more specific criteria for the presence or lack of ZnSe/ZnS in efficient kesterite devices are desired.

2.4.1 Effect of Zn/(Cu+Zn+Sn) ratio - bulk composition

It has been demonstrated in the literature that high efficiency devices may be produced with a wide range of Zn contents. Here, the same evaporator has been used in kesterite deposition over 100 times in a roll and the product films have been made into devices. The best devices within all these devices within different range of composition are selected and shown in Table 2.3. Their actual compositions and deposition run numbers are also provided. As long as the Zn/(Cu+Zn+Sn) ratio is not below 26.9%, the production of effective devices is possible. As shown in the table, 8% level before AR coating is achievable even when Zn/(Cu+Zn+Sn) ratio is as high as 37.1%. Since some of the films are extremely rich in Zn, there is no doubt that a large quantity of ZnSe coexists with kesterite in these efficient devices. Formation of metallic Zn is not possible because it is volatile in vacuum at the deposition temperature (around 500℃).

Table 2.3 Best NREL co-evaporated $Cu_2ZnSnSe_4$ devices within the specified range of composition before AR coating.

Zn/(Cu+Zn+Sn)	**Best PCE in the ranges**	**Actual metal % Cu/Zn/Sn**	**Run numbers**
35- %	8.45%	42.5/37.0/20.5	M3490
33-35 %	7.34%	43.7/33.8/22.5	M3433
31-33 %	8.21%	44.2/32.6/23.2	M3480
29-31 %	8.55% (w/AR 9.26%)	46.0/30.0/24.0	M3512
27-29 %	8.75% (w/AR 9.15%)	45.9/28.6/25.5	M3464
25-27 %	8.22%	46.5/26.9/26.6	M3503

The Zn/(Cu+Zn+Sn) of stoichiometric $Cu_2ZnSnSe_4$ is 25%. 8.45% device can be made even the film contains Zn/(Cu+Zn+Sn) as high as 37.0%. The PCEs of M3512 and M3464 after AR coating are shown in brackets.

2.4.2 Create ZnSe grains in different lateral positions

A more specific description on the status of ZnSe grains is desired. In this study, Zn excess at different lateral positions in the film is intentionally created. As discussed in Sec. 2.3.2, the ZnSe naturally forms on the back of the films when a relative high Zn evaporation flux was supplied from the beginning of deposition. This phenomenon has been utilized to create the Zn excess on the back of the film. To produce Zn excess at the front of absorber films, instead, additional Zn evaporation flux was applied at the end of depositions, specifically 5 minutes longer than the usual termination time.

Cross-sectional SEM images and AES depth profiles verify the positions of ZnSe in the film. Six films were studied in details. In the SEM images shown in Figure 2.8(a), ZnSe grains presented as the bright features are observed either on the top or the bottom of the film. (As discussed in Sec. 2.3.3, ZnSe appears bright because of the charging effect of a less conductive phase.) The films in category A (M3530, M3503) have a small but observable amount of bright spots on the top of the film as a result of the Zn cap mentioned earlier. Besides this Zn-rich layer on the top surface, no larger grains of ZnSe can be observed across the two films. For category B (M3480, M3490), in addition to the Zn cap, sub-micron to micron sized ZnSe grains are observed on the back of the films. All the other devices listed in Table 2.3 have cross-sectional images belong to either this category if it is rich enough in Zn, or category A if not rich enough. For category C (M3531, M3463),

ZnSe grains up to 300 nm in diameter are observed on the front of the films and protrude somewhat into the film along grain boundaries.

The distribution of Zn in the AES depth profiles further confirms the ZnSe positions observed by SEM images. One depth profile of Zn/(Cu+Zn+Sn) and Se/(Cu+Zn+Sn) out of each category is shown in Figure 2.8(b). Compared to the stoichiometric ratio of $Cu_2ZnSnSe_4$, the profiles are all Zn-rich throughout the films and even richer on the very surface of the films. The film shown representative of category B has an additional Zn-rich section near the Mo back contact, while the Zn-rich region for the category C film is on the front and penetrates more deeply into than that of the other two. The above description matches the observation of ZnSe locations from SEM images. In addition, the composition of Cu, Zn, and Sn (Cu and Sn are not shown in the paper) in the middle section of the profiles is relatively flat and exhibits little difference between three films. Since ZnSe grains are not located in the bulk of the film and SnSe, $SnSe_2$, Cu_2SnSe_3, and Cu_2SnSe_4 either evaporates or decomposes on high-temperature substrates (around 500℃)[14][88], the average AES composition derived from the middle section of the film can be attributed to the phase composition of $Cu_2ZnSnSe_4$, namely Zn/(Cu+Zn+Sn) = 0.265, Cu/(Cu+Zn+Sn) = 0.475 (identical to Cu/(Zn+Sn) = 0.94, Zn/Sn = 1.03). This composition is marked in the ternary phase diagram shown in Figure 2.9 together with the composition of the six films. Until now, no efficient devices have been found with bulk composition poorer in Zn than this phase composition.

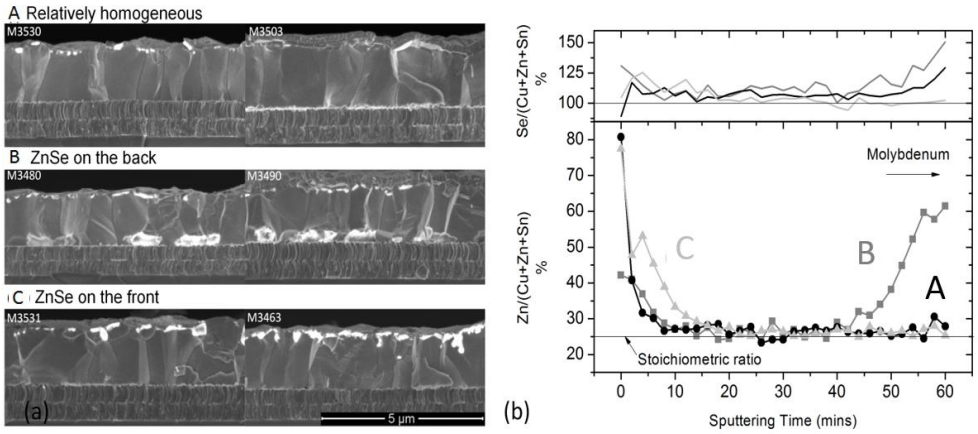

Figure 2.8 (a) Cross-sectional SEM images of films with A-relatively homogeneous composition (M3530, M3503), B-ZnSe grains on the back (M3480, M3490), and C-ZnSe grains on the front (M3531, M3463). (b) Depth profiles of Zn/(Cu+Zn+Sn) ratio derived from AES depth profile of M3530(A), M3490(B), and M3531(C).

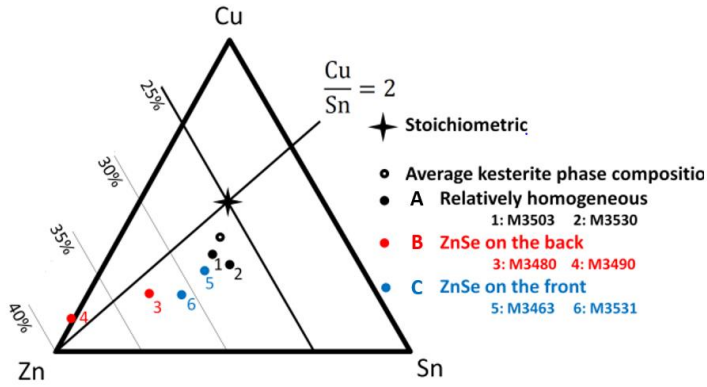

Figure 2.9 Compositons of the mentioned films obtained from XRF. Until now, we have not found efficient devices with bulk composition poorer in Zn than this phase composition. Adapted with permission © 2013 Elsevier

2.4.3 Effect of position of ZnSe grains on device performance

With better understanding on the position of ZnSe for these specific films, the effect of ZnSe position on their device performance now may be discussed. By comparing the J-

V parameters of devices listed in Table 2.4, it is found that when the amount of Zn is controlled well to that corresponding to single-phase kesterite (such as for samples M3530 and M3503), the cell efficiency attains ~8% without antireflection coating. If the film is much richer in Zn, and the ZnSe particles precipitate on the back of the absorber layer (such as for samples M3480 and M3490), the device performance is not affected. However, devices with large ZnSe grains on the front of the absorber layer have a much lower performance. Category C sample M3531, with a 6.51% efficiency, was deposited with deposition conditions identical to that of 8.28%-efficient category A sample M3530, except for the additional amount of Zn was added at the end of deposition. The reduced J_{SC} shown in Table 2 is responsible for half of the cell efficiency loss between these two samples, and the other half is due to the deficiency in V_{oc} and F.F. The internal quantum efficiency (QE_{INT}) shown in Figure 2.10(a) is defined as EQE/(1-R), where R = reflectance of devices. From M3530 to M3531, the loss in current is relatively independent of wavelength according to the QE_{INT} ratio shown in the same figure. The fact that the ratio between QE_{INT} of M3531 and QE_{INT} of M3530 does not decrease with longer wavelength suggests an issue locating on the front of the absorber instead of the bulk: bulk issues typically introduce difficulty in carrier collection from the back of the absorber, thus producing a stronger red than blue loss. The loss mechanism is therefore consistent with the observation of large ZnSe grains on the *front* of M3531. One possible reason behind the ZnSe position-sensitive current is a differential carrier blocking ability to electrons versus holes. ZnSe on the front of the absorber blocks electron and as a result reduces the photocurrent, while hole blocking by ZnSe on the back is negligible.

Table 2.4 J-V parameters of devices, PCE, V_{OC}, J_{SC}, and F.F. Numbers in parentheses are results obtained after annealing bare absorber.

Zn contents	Run numbers	PCE %	V_{OC} mV	J_{SC} mA	F.F. %
~ phase composition	M3503	8.22	351	35.9	65.3
	M3530*(-a)*	**8.02*(7.77)***	**359*(357)***	**34.4*(34.0)***	**64.9*(64.0)***
>Phase composition ZnSe on the back	M3480	8.21	360	36.1	63.1
	M3490	8.45	376	34.0	66.1
>Phase composition ZnSe on the front	M3463	6.60	338	31.7	61.7
	M3531*(-a)*	**6.51*(4.68)***	**337*(321)***	**31.5*(28.6)***	**61.3*(51.0)***

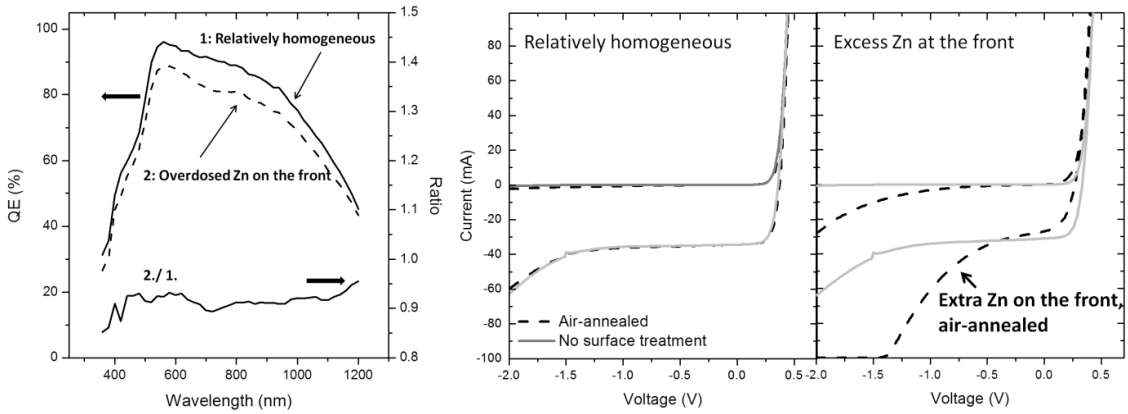

Figure 2.10 (a) QE_{INT} of cells without large ZnSe grains (category A, M3530), with ZnSe grains on the front of absorber (category C, M3531) and the ratio between the two. (b) JV curves of the same two devices (M3530, and M3531) and their air-annealed counterparts (M3530-a, M3531-a).

2.4.4 Blue-light induced breakdown

Diode breakdown is apparent in reverse bias range in all the light JV data of Figure 2.10(b), and is particularly severe in the category C (excess Zn at front) air-annealed devices. For the air-annealed category C devices, the breakdown occurs even in the dark JV data, and - in the light JV data - occurs at a smaller reverse voltage than for the other types of devices. In contrast, air-annealing a relatively homogeneous film did not make

considerable change to JV (M3530-a). Therefore, we conclude that the severity of the breakdown behavior is related to the excess of Zn on the front of the absorbers and appears obvious when the extra Zn layer is oxidized.

Air-annealed category C devices not only show increased reverse bias breakdown, but also severely decreased performance. The J-V parameters of M3530, M3530-a, M3531, and M3531-a are given in Table 2. The parameters of M3530-a and M3531-a are presented in parentheses after those of M3530 and M3531, respectively. The absorbers of M3530-a and M3531-a were cut from the same piece of M3530 and M3531, respectively, but were annealed at 175℃ for 5 minutes in air. While the device with relatively homogeneous composition (M3530) has only a slight reduction in cell efficiency, the one with excess Zn on the front of absorber (M3531) suffers from large degradation to V_{OC}, J_{SC}, and F.F., resulting in a great reduction of device efficiency (to 4.68%). Thus, we are motivated to further study the reverse voltage breakdown, not only to understand the role of Zn at the front of the device, but also because the most severe breakdown occurs in the devices with the poorest performance. Understanding and eliminating the effect may therefore help improve performance.

J-V measurements under the illumination of different wavelength ranges were conducted to study the mechanism of breakdown behavior. Figure 2.11(a) shows the results of simulated AM1.5 filtered by 570 nm, 530 nm and 495 nm long-pass filters, along with unfiltered white light. It appears that the breakdown is blue light-sensitive as the breakdown does not appear when the light is filtered by 570 long-pass filter. To understand the response of breakdown with better resolution in photon energy, reverse bias QE was measured. Data are shown in Figure 2.11(b). At reverse biases below 1.0 V, the QE

basically retraces the unbiased QE with slight enhancement at long wavelengths. Beyond 1.0 V, a peak appears between 360 nm - 530 nm. The magnitude of the peak rises abruptly with slight increase in the reverse voltage. It is important to realize that an apparent quantum efficiency exceeding 100% does not indicate actual generation of more carriers than photons incident. Rather, the reverse-biased QE measures the vertical distance (current) between light and dark JV curves at a given bias. Thus, the large apparent QE is an indicator of the light-activated breakdown or shunting.

The absorption edge to turn on the breakdown is identified as 530 nm by the leading edge of the peak in the QE. This analysis agrees with the findings from JV curves that a 495 nm long-pass filter does not turn off the breakdown, and a 530 nm filter nearly does. 530 nm matches accurately with the absorption edge of CdS[89]. Accordingly, the blue-photon induced breakdown is likely to be associated with the absorption of CdS. The 530 nm onset of the breakdown does *not* match with the absorption of ZnSe, even though it exists in large quantities for devices where the breakdown effect is most severe. Optical effects in ZnSe are expected to appear around 460 nm, based on the larger band gap of ZnSe. In addition, in the forward-biased QE, the wavelength onset of the peak (shown in Figure 2.11(b), 0.4V) matches well with that of a CIGS device with CdS as buffer layer[90] and fails to match with the one with ZnSe as buffer layer[91]. The photoconductivity of CdS has been previously reported in CIGS solar cells to result in the distortion of light JV curves in the fourth (power) quadrant under certain conditions[92]. This work is the first report of a blue-photon sensitive non-linear effect in the third quadrant.

One simple model that could possibly help us to understand how the behavior is related to CdS photo-conductance is the lateral distribution of shunting channels. When

shunting channels are laterally distributed on absorber, the current will be switched on when CdS is illuminated, turns conductive, and provides little spreading resistance for the current exiting the shunt paths. In this case, even though a simple metallic shunting behavior is sufficient to explain the on and off characteristics of the reverse current, it is still not enough to explain the magnitude of the reverse current being non-linear with voltage. In essence, the breakdown behavior is a result of problematic absorber which has lateral distributed defects and those defects must have *non-ohmic* contacts with photoconductive CdS.

The actual chemistry of these defects remains unclear to us. As described, the severity of blue-photon induced breakdown is related to the excess of Zn at the front of absorber. Therefore, even though ZnSe's absorption does not directly result in the behavior (instead, the absorption of CdS does), an effect involving both the absorption of CdS and the excess of Zn must be responsible. It has been demonstrated in the SEM images that, for category III films, the Zn excess produces grains of ZnSe that protrude into kesterite films along the grain boundaries. The penetration of excess Zn may at the same time produces other types of Zn-rich features along the grain boundaries. Alteration of the localized electrical property is possible. Air-anneal converts ZnSe on the surface into ZnO, which has much lower conduction band edge[93], and thus may facilitate current flow. The hidden electrical defects are accordingly exposed, exhibiting as severe breakdown and reduced F.F.

In brief, we think that the blue-light induced breakdown is a symptom of problematic absorbers. The generation of Zn-rich localized features followed by air-annealing is one of the ways to create or activate these defects. The same type of defect

contributing to the breakdown may be responsible for part of the parasitic loses at the PV working voltage as well and therefore deserves certain degree of attention.

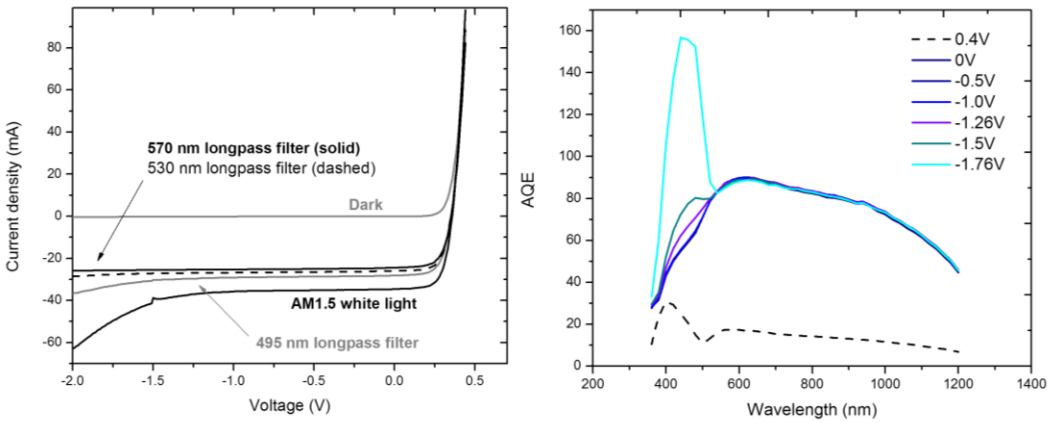

Figure 2.11(a) filtered JV of the device with relative homogeneous composition, (b)Non-equilibrium QE of M3530.

2.5 Summary and outlook

In this study, the strength of co-evaporation is utilized; the growth strategies have been extended from only the Cu-rich growth to Zn-rich growth, and near-stoichiometric growth. By investigating the phase evolution in the three different deposition routes, the methods to control film composition and phase constitution have been made precise enough to attain 8% to 9% efficient cells.

The absence of SnSe, $SnSe_2$, Cu_2SnSe_3, and Cu_4SnSe_4, which are unstable at the temperatures and pressures used here, simplifies the constitution of precursor, allowing easier in-situ control during deposition by monitoring the surface emissivity of the film. The major challenge to developing Zn-rich growth and near-stoichiometric growth is the

subtle reaction obstacle between Cu_xSe_y and ZnSe related to the volatile nature of Sn and/or the physical separation between the ZnSe in the film and incident Cu is observed. The remaining Cu_xSe_y will result in shunting devices if not removed. Leaving the film at high temperature with a continued supply of Sn vapor offers a chance for the residual to react to form kesterite phase. The endpoint detection by watching the substrate temperature leveling off, as commonly performed in the Cu-rich growth of CIGS co-evaporation remains applicable and necessary in the various strategies of kesterite co-evaporation. For these deposition rates, co-evaporated kesterite, in contrast with the chalcopyrite, generally has micron-scale grains regardless of the Cu-rich or poor deposition strategy. The lack of discrepancy in grain size is likely to be the result of the general existence of Cu_xSe_y in every growth strategy at the deposition rates explored in this study. Thus the Cu_xSe_y can conduct liquid-phase assisted grain growth around its eutectic temperature even when the average film composition is Cu-poor.

It is encouraging to learn that kesterite can be co-evaporated with precise control of composition and phase with deposition routes starting from different compositions and achieve 8-9% cell efficiency without any efforts in experimental condition fine-tuning. It is expected in the future, by playing to the strength of co-evaporation, the record efficiency of kesterite solar cells may be greatly improved.

Another major conclusion of the study is that, even though kesterite solar cells have a very large tolerance of ZnSe secondary phases (Zn/(Cu+Zn+Sn) ratio at least up to 37.1%, which is almost 1.5 times the stoichiometric Zn content), it is required that the ZnSe grains are at the back of the device. Large ZnSe grains on the front of the absorber, created by overdosing Zn at the end of deposition, are detrimental for device performance. A blue-

light induced reverse-bias breakdown related to the ZnSe grains on the front of the absorber is observed. Qualitatively, the effect is considered as a symptom of laterally distributed defects in the absorber (in this case ZnSe grains protruding into the absorber) through which current is regulated by the spreading resistance of the CdS.

Chapter 3 Hydrazine-processed kesterite

In Chapter 2, we emphasized how to play to the strengths of the co-evaporation processing, to produce high-performance kesterite cells with precise control of phase and composition. However, as mentioned in Chapter 1, the industry has experienced difficulty and a higher cost when scaling the co-evaporation processing when working on CIGS solar cells. Great efforts have been spent on the dream of solution processing, which may ultimately eliminate the need for expensive high vacuum equipment and batch processes.

Hydrazine-based solution deposition, as discussed in Chapter 1, has taken a leading role in producing high efficiency devices from this material system[11][40][34][41], even outperforming the high vacuum deposition methods. It is encouraging to imagine that a solution-based process of this kind may one day be scaled up to fulfill the dream of large scale manufacturing. There is still a long way to go since, first of all, hydrazine is a highly explosive solvent, which is probably not scalable. Therefore, it is significant to understand the reaction pathway of the processing, which may provide specific guidelines for the development of other solution-based processing methods based on benign solvents widely accepted by industry.

This study is the tracking of the reaction mechanisms involved in the overall transformation from precursor ink to solid state framework and finally to the CZTSSe phase during deposition and subsequent thermal treatment. General introduction of the hydrazine-based thin film processing (Sec. 3.1) and the experimental methods of this study (Sec. 3.2) are firstly given. The chapter later explains how X-ray diffraction and Raman

spectroscopy have been employed to track the various stages of the reaction pathway, and to mark the formation and consumption of precursor phases as they interact to form the final material. The reaction pathway from solution formation to dried precursor film, and the solid-reaction from dried precursor film to the annealed film are described in two stages (Sec 3.3 and Sec 3.4). Finally, the obtained reaction pathway is compared with the reaction pathways of other vacuum and non-vacuum processes (Sec. 3.5). It is found that the reaction pathway of hydrazine-processed kesterite contains far fewer steps than most deposition methods, which typically start with elemental or binary chalcogenides. As the formation of secondary phases such as $Cu_{2-x}S$, SnSe, and $SnSe_2$ is no longer necessary to produce the final $Cu_2ZnSn(Se,S)_4$ phase, the relative simplicity of this formation mechanism is likely beneficial for the performance of the resulting solar cells. At last, the final section concludes the chapter (Sec. 3.6).

3.1. Introduction to hydrazine-based processing

As a fabrication technique, hydrazine-based processing has also facilitated the deposition of a diverse array of commercially relevant materials[94], creating a low-cost and high throughput approach for producing high quality thin films for solar cells[95][96][97][98][99], field-effect transistors[100][101], and other optoelectronic devices. Successful examples include the monometallic chalcogenides SnS_2[101], $SnSe_2$[102], and In_2Se_3[100], the bimetallic chalcogenide $CuIn(Se,S)_2$[96][97], and the trimetallic chalcogenides $Cu(In,Ga)(S,Se)_2$[95] and $Cu_2ZnSn(S,Se)_4$[40][34][11][41].

During the ink formation step, hydrazine is used to dissolve chalcogenides in the presence of excess chalcogen by breaking them down into 0-D, 1-D, or 2-D precursor complexes. This dissolution mechanism has been termed dimensional reduction.[94] If not all of the precursor materials are fully soluble in the resulting liquid, then the use of such an ink to deposit films is colloquially referred to as slurry deposition. Both molecular-scale solution[96][97][95][11][41] and slurry-based precursor inks[98][99] are compatible with spin-coating, blade coating, and other common liquid deposition techniques.

As the deposited films are dried, the metal chalcogenide precursor complexes act as building blocks to construct a three dimensional framework incorporating both the chalcogenide material and an ordered number of solvent molecules.[94][103] If the ink only involves a single species of binary chalcogenide, the resulting framework will typically decompose back to the original chalcogenide after thermal annealing[100][101][102][104], if the ink involves more than one species of chalcogenide, the various species, at least in some cases[95][96][97][98][99], can combine into one multimetallic phase if the proper precursor ratio was applied. How these precursor complexes pack with solvent atoms to form extended ordered frameworks has drawn significant research interest for many years. Our understanding of the precursor structures of monometallic systems, such as SnS_2, $SnSe_2$, Cu_2S, In_2Se_3, has been improved by Single Crystal X-Ray Diffraction (SCXRD) measurements based on single crystals grown from supersaturated precursor solutions.[101][102][104] However, it remains unclear how multiple metallic chalcogenide complexes combine into a single multimetallic phase, such as $Cu_2ZnSn(Se,S)_4$, during the crystallization process.

This is a topic of interest since, to date, the highest performance CZTS and CZTSSe devices have been fabricated through hydrazine ink processing. The existence of a liquid-phase process capable of outperforming its vacuum-based counterpart is an unusual occurrence in the development of thin film solar cells. This study depicts the format of the dried precursors and details the solid reaction route during thermal treatment.

3.2 Experimental methods

3.2.1 Preparation of precursor solutions and inks

Cu_2S-S solution was prepared by dissolving Cu_2S powder (American Elements, 99.999%) and elemental sulfur (Aldrich, 99.998%) in hydrazine (Aldrich, anhydrous, 98%) with a Cu_2S:S ratio of 1:2 and [Cu] = 1.0M. $SnSe_2$-Se solution was prepared by dissolving $SnSe_2$ powder (American Elements, 99.999%) and elemental selenium (Alfa Aesar, 99.999%) in hydrazine with a $SnSe_2$:Se ratio of 1:3 (1:1 for solutions used in Raman spectrum acquisition) and [Sn] = 1.14 M. ***Caution:*** *hydrazine is highly toxic and should be handled with appropriate protective equipment to prevent contact with both the liquid and vapor.*

To prepare the CZTSSe precursor slurries, metallic zinc powder with a particle size smaller than 80 nm (Aldrich, 99.8%) was added into the $SnSe_2$-Se solution. After stirring for more than 10 hrs, Cu_2S-S solution was added to the mixture. The final precursor slurries targeted an atomic ratio of Cu/(Zn+Sn) = 0.80-0.85 and Zn/Sn = 1.2-1.3, (or Cu/(Cu+Zn+Sn) ~45%, Zn/(Cu+Zn+Sn) ~31%, Sn/(Cu+Zn+Sn) ~ 24%), in other samples

where zinc was absent. By centrifugation at 8000 rpm, the solution-phase component was partially separated from the solids present in the slurry. After multiple cycles of dilution and centrifugation and a final drying process, the precipitate was effectively isolated from any remaining solvent and soluble materials. The preparation of all involved solutions and slurries was conducted in a nitrogen-filled glove box with the oxygen and moisture levels each below 1 ppm.

3.2.2 Precursor drying

A series of powder samples to be used for precursor characterization was prepared by drying each solution. Powders consisting the of $Cu_7S_4^-$, $Sn_2Se_6^{4-}$, $Cu_2Sn(Se,S)_x$ and $Cu_2ZnSn(Se,S)_x$ hydrazinium frameworks were derived by drying the Cu_2S-S solution, $SnSe_2$-Se solution, Cu_2S-S and $SnSe_2$-Se mixed solution and final CZTSSe precursor slurry in vacuum for durations ranging from 1 day to 1 week.

Thin films of $Cu_7S_4^-$, $Sn_2Se_6^{4-}$, $Cu_2Sn(Se,S)_x$ and $Cu_2ZnSn(Se,S)_x$ hydrazinium frameworks were deposited by spin-coating each precursor solution or slurry at 800 rpm onto molybdenum substrates. The powders and films were either dried without heating or annealed on hot plate with durations between 5 and 30 minutes at temperatures ranging from 100 ℃ to 540℃.

3.2.3 XRD and Raman characterization

The X-ray diffraction patterns of the powdered hydrazinium frameworks as well as annealed powder samples were collected using a PANalytical X'Pert Pro X-ray Powder Diffractometer with a Cu-Kα x-ray source (λ=1.54050Å). For unstable samples such as the

dried hydrazinium compounds, multiple scans were conducted in order to confirm the reproducibility of the data under x-ray exposure. Polyimide films were applied to cover and seal the $Cu_7S_4^-$ hydrazinium compounds before their removal from a nitrogen atmosphere, and were kept in place during diffraction measurements. Without a layer of protective encapsulation, consistent results could not be attained from this type of sample during sequential scans.

Raman spectra of precursor solutions, pastes, and solid frameworks were acquired by a Renishaw inVia Raman system using a 514.5 nm Ar laser. The laser power was 25 mW for solutions and slurries, but was reduced to 5 mW when measuring solid samples in order to prevent the laser-induced annealing of unstable samples. All Raman samples that are unstable under atmospheric conditions were sealed to avoid air exposure. The detailed sealing methods can be found in a previous publication.[105] Thermogravimetric analysis (TGA) was performed with a ramp rate of 2 ℃/min in flowing argon. Metal ratios in the resulting powders were calculated according to compositional measurements based on Energy dispersive x-ray spectroscopy (EDS).

3.3 Precursor Species and Their Resulting Hydrazinium Frameworks

The precursor slurry of CZTSSe is composed of two components: Zn-Se-S, an insoluble phase, and a soluble Cu-Sn-Se-S phase. The Raman profiles of the precursor slurry and the XRD pattern of its dried CZTSSe hydrazinium framework are shown in

Figures 3.1(a.1) and (a.2), respectively. The two components are described separately in the following sections:

3.3.1 Zinc Species

$Zn(Se,S)(N_2H_4)$ is an insoluble species in hydrazine, typically existing as dispersed nanocrystals within the precursor ink.[98] The powder diffraction spectrum we obtained by centrifuging and drying the particles present in the CZTSSe precursor ink (Figure 3.1(b.2)) is analogous to the XRD spectrum of $ZnSe(N_2H_4)$ reported in a previous study.[98] $ZnSe(N_2H_4)$ remains one of the components after the CZTSSe ink is dried as its XRD peaks are still visible in the dried CZTSSe precursor slurry(Figure 3.1(a.2)).

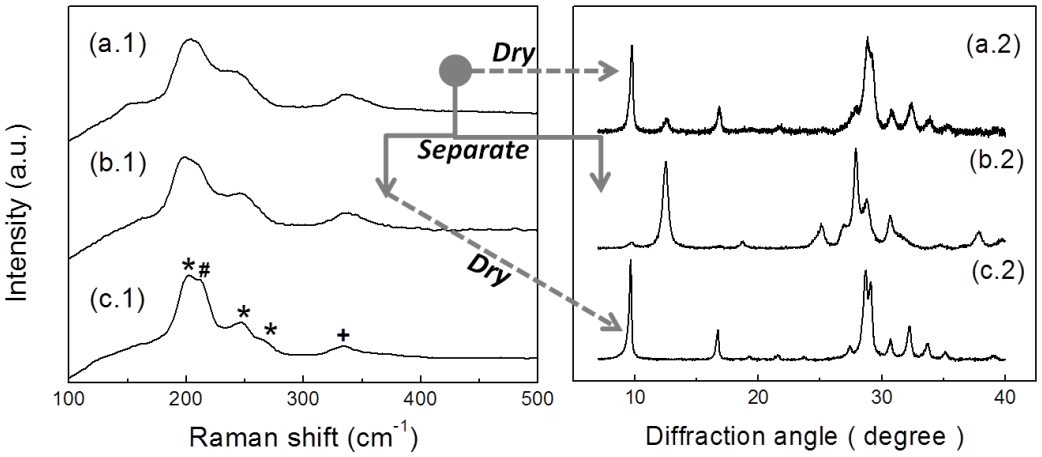

Figure 3.1 (a.1) Raman spectra of the Zn-Cu_2S-S-$SnSe_2$-Se precursor solution, (b.1) real-solution component of the Zn-Cu_2S-S-$SnSe_2$-Se precursor solution, and (c.1) Cu_2S-S-$SnSe_2$-Se mixed solution. $SnSe_2$-Se solution with $SnSe_2$: Se = 1: 1 was used. 200 cm^{-1}, 246 cm^{-1}, 268 cm^{-1} (marked by *) are vibrational modes of the double-centered $Sn_2Se_6^{4-}$ complexes. 335 cm^{-1} (marked by +) is the vibrational mode of Cu-S stretching. 214 cm^{-1} (marked by #) has not been observed from either Cu_2S-S or $SnSe_2$-Se solution. (a.2) XRD patterns of the CZTSSe precursor powder, derived from drying the Zn-Cu_2S-S-$SnSe_2$-Se precursor slurry, (b.2) $Zn(Se,S)(N_2H_4)$ powder, derived from drying the filtered precipitation of the slurry, and (c.2) $Cu_2Sn(Se,S)_x$ hydrazine/hydrazinium powder, derived from drying the real-solution component of the same slurry.

3.3.2 Copper and Tin Species

The soluble components of the CZTSSe precursor ink are a mixture of copper species and tin species. Energy Dispersive X-ray Spectroscopy (EDS) analysis of the dried solution-phase component indicates a composition with less than 3 atomic percent zinc after the solid particulates have been removed through repeated centrifugation. The near complete absence of zinc allows the separated solution phase to produce a Raman spectrum (Figure 3.1(b.1)) effectively identical to that of a mixed Cu_2S-S and $SnSe_2$-Se hydrazine solution (c.1). The solution phase contributes nearly all of the Raman signal detectable from the final slurry Figure 1 (a.1) in the range between 100 cm^{-1} and 500 cm^{-1}.

After being dried, this Cu-Sn-Se-Se solution-phase component remains structurally segregated from Zn-Se-S phase. The dominant XRD peaks of the dried solution-phase (Figure 3.1(c.2)) present clearly in the XRD spectrum of the dried CZTSSe precursor slurry (a.2), indicate that the ordering of the copper and tin species that occurs upon drying is unperturbed by the introduction of the zinc particulates. An isolated mixture of dried Cu_2S-S and $SnSe_2$-Se hydrazine solution with no additional Zn will produce identical XRD spectrum (Figure 3.2(a.1)).

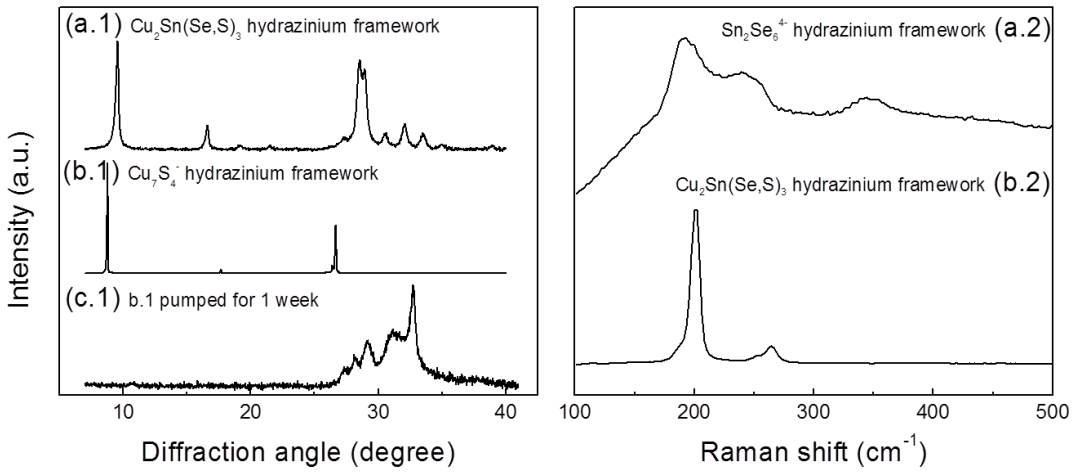

Figure 3.2 (a.1) XRD patterns of Cu-Sn-Se-Se precursor powder derived from pumping Cu_2S-S-$SnSe_2$-Se mixed solution for one week, (b.1) $(N_2H_4)(N_2H_5)$ Cu_7S_4 powder derived from pumping the Cu_2S-S solution overnight, (c.1) covellite (reference code 03-065-0603, P63/mmc), obtained by pumping the Cu_2S-S solution for 1 week. (a.2) Raman spectra of Cu-Sn-Se-S precursor film derived from pumping Cu_2S-S-$SnSe_2$-Se mixed solution for one week and (b.2) $(N_2H_4)_3(N2H5)_4$ Sn_2Se_6 film derived from pumping $SnSe_2$ –Se solution for 1 week.

3.3.3 Bimetallic Integration Process

Due to their unchanged nature before and after the addition of insoluble zinc species, further studies of the soluble Cu-Sn-Se-S phase present in the CZTSSe precursor slurry and the resulting solid precursor were conducted using analogously prepared mixtures of Cu_2S-S and $SnSe_2$-Se hydrazine solution.

When Cu_2S-S solution and $SnSe_2$-Se solution are mixed, neither Cu-Se nor Sn-S bonding interactions are evident in the combined Raman spectrum. However, when drying the mixed solution, these two complexes arrange themselves periodically into a solid framework that is distinctly different from their unmixed structures. Copper sulfide complexes dissolved in hydrazine typically exist with a formula of $Cu_6S_4^{2-}$. The Raman scattering mode associated with Cu-S stretching locates at 335 cm^{-1}.[105] Tin selenide

dissolved in hydrazine takes on a 0-D structure with the chemical formula $Sn_2Se_6^{4-}$.[102] The Raman scattering modes associated with this complex are located at 202 cm^{-1}, 248 cm^{-1}, and 270 cm^{-1}, indicating a double-centered molecule.[106] (The Raman spectra of the individual copper sulfide and tin selenide solutions can be found in Appendix B.) When Cu_2S-S and $SnSe_2$-Se solutions are mixed, the above mentioned peaks found in the spectra of the two individual solutions are preserved as shown in the Raman spectrum in Figure 3.1 (c.1). The 200 cm^{-1}, 246 cm^{-1}, and 268 cm^{-1} vibrational modes correspond to the double-centered $Sn_2Se_6^{4-}$ molecule, and the 335 cm^{-1} mode signals the presence of Cu-S stretching. The additional peak at 214 cm^{-1} does not agree with the expected vibration frequency of Cu-Se stretching, which occurs around 276 cm^{-1},[107] nor the vibration frequencies of the $Sn_2S_6^{4-}$ complex that are found at 281 cm^{-1}, 341 cm^{-1}, and 377 cm^{-1}.[108] Since their primary peaks were preserved, the two monometallic complexes presumably remain intact during the mixing process, and produce the observed new bonding interaction without costing the original copper and tin species and their characteristic structure.

A solidified hydrazinium framework was prepared by drying the mixed Cu_2S-S-$SnSe_2$-Se solution in roughing vacuum for 1 week. Figures 3.2(a.1) and (a.2) show the XRD pattern and the Raman spectrum of the dried mixture, respectively. As indicated by the pronounced peaks of the XRD pattern, the solid framework is a highly crystalline structure. The intense small-angle peak suggests a highly periodic arrangement between metal chalcogenide clusters separated by hydrazine or hydrazinium molecules. This combined structure is distinct from the hydrazinium frameworks derived by drying Cu_2S-S solution and $SnSe_2$-Se individual solutions, i.e. $(N_2H_4)(N_2H_5)Cu_7S_4$[104] and

$(N_2H_4)_3(N_2H_5)_4Sn_2Se_6$[102]. For brevity, the resulting mixed phase will be referred to as the $Cu_2Sn(Se,S)_y$ hydrazinium framework.

The structural differences between the $Cu_2Sn(Se,S)_y$ and $Cu_7S_4^-$ hydrazinium frameworks are readily visible in their XRD spectra. The solid $Cu_7S_4^-$ hydrazinium framework, prepared by pumping down Cu_2S-S solution overnight, has a series of XRD peaks, shown in Figure 3.2(b.1). The peak with smallest angle is located at 8.7681 degrees, corresponding to an interplanar distance of 10.0763 Å, which agrees accurately to the reported distance between 2-D $Cu_7S_4^-$ slabs within the $(N_2H_4)(N_2H_5)Cu_7S_4$ structure.[104] However, the dried $Cu_2Sn(Se_{1-x},S_x)_y$ hydrazinium framework has an entirely different peak list and peak widths, exhibiting significantly weaker crystallinity. Its small angle diffraction peak is located at 9.5474 degrees, corresponding to a lattice plane spacing of 9.2555 Å. None of the structural nature of $(N_2H_4)(N_2H_5)Cu_7S_4$ can be found in this new framework. If the $(N_2H_4)(N_2H_5)Cu_7S_4$ is further pumped down for as long as one week in order to match the preparation method of the mixed copper-tin sample, most of the hydrazine and hydrazinium ligands will escape and the structure eventually becomes covellite CuS with a dark blue color (reference code 03-065-0603, P63/mmc). The powder XRD pattern of the resulting material is shown in Figure 3.2(c.1). Based on the above observations, it is apparent that the $Cu_6S_4^{2-}$ species undergoes dramatic changes upon being mixed with $Sn_2Se_6^{4-}$, resulting in both an entirely different crystal structure and a much lower tendency to lose its hydrazine and hydrazinium spacer molecules during drying.

Similar to the case of copper sulfide, anticipated structural features typical of a $Sn_2Se_6^{4-}$ hydrazinium framework cannot be found when characterizing the mixed framework material. Quite distinct from $Cu_2Sn(Se,S)_y$, the $(N_2H_4)_3(N_2H_5)_4$ Sn_2Se_6

framework cannot be dried in vacuum even after pumping for as long as a week. It is highly unstable in air, and its diffraction pattern is effectively washed out by artifacts from the protective polyimide cover, so an accurate comparison between the $Sn_2Se_6^{4-}$ hydrazinium compound and the new phase via XRD is lost. Even so, we were able to acquire clear Raman spectra of the $Sn_2Se_6^{4-}$ hydrazinium compound, as shown in Figure 2(b.2). Although the vibration modes of $Sn_2Se_6^{4-}$ are both sharp and intense in this figure, they are not visible in the $Cu_2Sn(Se,S)_y$ hydrazinium framework, which can be found in Figure 2(a.2).

In summary, mixtures of $Cu_6S_4^{2-}$ and $Sn_2Se_6^{4-}$ complexes with [Cu]/[Sn] ≈ 2 have been observed to spontaneously arrange themselves into a new structure, $Cu_2Sn(Se,S)_y(N_2H_n)_z$, n = 4, 5 which is a bimetallic hydrazine/hydrazinium precursor. Other bimetallic compounds formed using a similar concept have also been reported, including $Mn_2SnSe_4(N_2H_4)_{10}$, $Mn_2SnSe_4(N_2H_4)_7$, $Mn_2SnS_4(N_2H_4)_6$, $Mn_2SnS_4(N_2H_4)_5$[109], $Mn_2SnS_4(N_2H_4)_2$[110], $Mn_2Sb_4S_8(N_2H_4)_2$[111], and $Mn_2Sb_2S_5(N_2H_4)_3$[96]. This mixed precursor complex can then serve as an advantageous starting point to the solid state reaction that will ultimately form the final CZTSSe phase.

One additional interesting fact to discuss shortly is the relatively higher crystallinity of the bimetallic hydrazinium compound compared to the amorphous type formed by the $CuIn(Se,S)_2$ (CISS) system(another successful example of a hydrazine-based ink-processed photovoltaic absorber material.[103]) The fact that both copper and tin species form crystalline structures individually[104][102] likely improves the chances of forming a highly crystalline mixed precursor. A brief overview of the degree of ordering typically

observed in frameworks formed from the precursor solutions that lead to CZTSSe and CISS inks can be found in Table 3.1.

Table 3.1 Summary of the crystal structures of several monometallic and bimetallic hydrazine/hydrazinium compounds

<table>
<tr><th>Precursor solutions</th><th colspan="3">Structures</th></tr>
<tr><td>In_2Se-Se (A)</td><td>$(N_2H_4)_2(N_2H_5)_2\ In_2Se_4$
Amorphous [9]</td><td rowspan="2">(A)+(B)

Amorphous [3][12]</td><td></td></tr>
<tr><td>Cu_2S-S (B)</td><td>$(N_2H_4)(N_2H_5)\ Cu_7S_4$
Crystalline [13]</td><td rowspan="2">(B)+(C)

Crystalline</td></tr>
<tr><td>$SnSe_2$/

SnSe-Se (C)</td><td>$(N_2H_4)_3(N_2H_5)_4\ Sn_2Se_6$
Crystalline [11]</td><td></td></tr>
</table>

3.4 Solid State Reaction Pathways

Through the studies of dried precursor complexes discussed above, the starting points of the formation of the kesterite phase has been identified as a $Cu_2Sn(Se,S)_y$ hydrazinium framework along with the solid phase $Zn(Se,S)(N_2H_4)$. Different from other two-step deposition processes, which start from pure elements or binary chalcogenides, the solid-state reaction route in the hydrazine-based processing starts from a previously formed Cu-Sn-Se-S complex along with Zn-Se before any thermal treatement has been done.

Figure 3.3 is the TGA data representing the decomposition of the hydrazinium frameworks and formation of the CZTSSe phase. The first stage of weight loss mainly corresponds to the removal of hydrazine and hydrazinium molecules and sulfur species, while the second stage is mostly from the loss of selenium. The metal compositions of samples annealed at different temperature are also presented in the same figure. Figure 3.4 displays the powder XRD patterns of CZTSSe precursors annealed at different temperatures for 30 minutes, corresponding to several data points on the TGA curve.

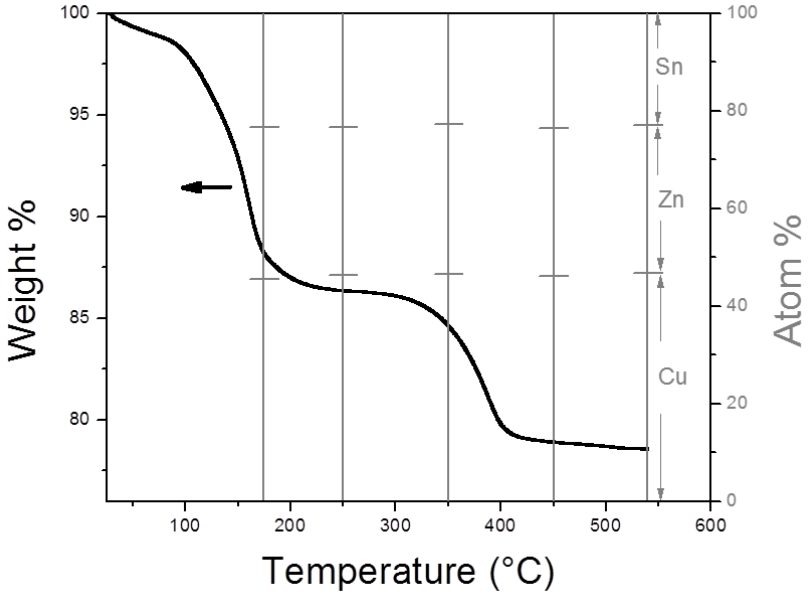

Figure 3.3 TGA of the Cu-Zn-Sn-Se-S precursor powder as it decomposes into $Cu_2ZnSn(Se,S)_4$ and the metal ratio of powder subjected to separated thermal processes with different annealing temperature.

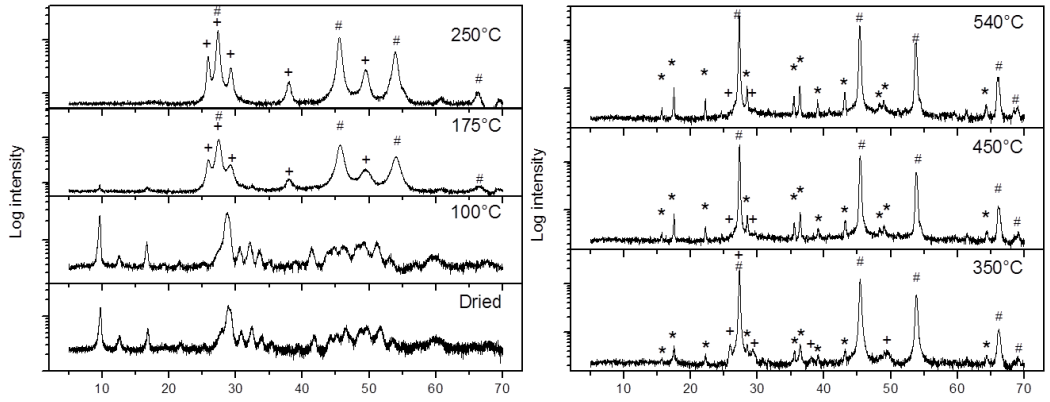

Figure 3.4. (a) XRD patterns of dried Cu-Zn-Sn-Se-S precursor, annealed at 100 ℃, 175 ℃, and 250 ℃, as well as (b) at 350 ℃, 450 ℃, and 540 ℃. Peaks marked with # are shared by tetragonal Cu_2ZnSnX_4 and cubic Cu_2SnX_3. Peaks marked with * are unique to tetragonal Cu_2ZnSnX_4. Peaks marked with + are wurtzite ZnX.

Suggested by TGA and XRD, the structure of hydrazinium frameworks is maintained at least up to 100℃ before subjecting to dramatic weight loss by rejecting hydrazine molecules and change in diffraction pattern. After annealing at 175 ℃, they have been decomposed. $Zn(Se,S)(N_2H_4)$ is mostly decomposed to wurtzite ZnSe (reference code 01-089-2940, P63mc), indicated by peaks marked with '+'. Most reports on the formation of Cu_2ZnSnX_4 (X= Se,S) from copper, zinc, and tin chalcogenide precursors observe the intermediate ZnX phase in its cubic form. However, the $ZnX(N_2H_4)$ precursors in our work and also nanowires synthesized from hydrothermal routes with hydrazine hydrate serving as the solvent[112][113] are reported as wurtzite after annealing at 175 ℃ - 180 ℃. According to Todorov et al[98], the ZnSe structure resulting from the decomposition of $ZnSe(N_2H_4)$ is stable at least to 540℃. At this temperature, the $Cu_2Sn(Se,S)_y$ hydrazinium framework is also decomposed. A series of peaks marked with '#' in the figure represent either $Cu_2Sn(Se,S)_3$ (reference code 01-089-2879, F-43m) or $Cu_2ZnSn(Se,S)_4$

($Cu_2ZnSnSe_4$ reference code 00-052-0868, I-42m; Cu_2ZnSnS_4 reference code 00-026-0575, I-42m). Since these two phases share primary diffraction peaks, it is not conclusive whether only the decomposition of $Cu_2Sn(Se,S)_y$ hydrazinium framework has taken place or if the $Cu_2ZnSn(Se,S)_4$ phase has begun to form simultaneously. Whichever the case, the transformation has already begun at 175 ℃, without the presence of copper and tin binary chalcogenides. Cu_2SnX_3 is frequently observed as an intermediate phase in various vacuum-based deposition processes. The initial formation temperatures range from 250 ℃ to 300 ℃ for methods that involve metal deposition followed by selenization[114][115], 150 ℃ for coevaporation[116], and 100 ℃ for the sputtering of a Cu_2Se + $SnSe_2$ compressed target[117]. For most of these processes, more than two hours of deposition, annealing, or selenization is required, and often the reaction route involves elemental metals, alloys, or binary chalcogenides. The complete conversion of these phases to Cu_2SnX_3 does not happen until an even higher annealing temperature is applied. While here, bimetallic (if not trimetallic) chalcogenides are formed immediately after the precursor slurry is dried and subjected to a mild thermal treatment.

An important note is that the presence of zinc species is critical for preventing the formation of tin and copper binary phases at 175 ℃. If one simply mixes and dries the Cu_2S-S and $SnSe_2$-Se solutions and anneals the resulting powder at 175℃, in the complete absence of zinc species, the XRD pattern shows as many as three phases: $Cu_2Sn(Se,S)_3$, $SnSe_2$, and Cu_2Se. If the dried powder comes from a filtered CZTSSe precursor slurry, which still retains a limited amount of zinc species, the small amount of zinc present is enough to prevent the formation of binary phases, producing a diffraction pattern similar to the 175 ℃ data shown in Figure 3.4, but with its ZnSe peaks much weaker. The observed

diffraction spectra are shown in Appendix B. The dominant mechanisms responsible for this phenomenon are not fully understood at present.

At 250℃, the (1 0 2) and (1 0 3) reflections of Zn(Se,S) are reduced compared to their observed intensities at 175 ℃, implying that the $Cu_2ZnSn(Se,S)_4$ phase has expanded at the expense of Zn(Se,S). At 350℃, with a large consumption of Zn(Se,S), the (1 0 1) and (1 1 0) reflections of kesterite appear, which are two of the few peaks that are distinct from those of $Cu_2Sn(Se,S)_3$. Thus, there is no doubt that kesterite has been formed at 350 ℃, although a small amount of wurtzite Zn(Se,S) is still visible in the spectrum. Beyond 450℃, the crystallinity of $Cu_2ZnSn(Se,S)_4$ is further improved and the phase is stable up to at least 540 ℃ without significant decomposition. Also, based on the compositional and weight loss analysis shown in Figure 3.3, there is no loss of metal elements upon high temperature annealing. A small amount of residual wurtzite Zn(S,Se) is present since an overall Zn-rich sample composition was chosen in this study, and creates the shoulders of the dominant XRD peak. Based on this progression of spectra, we can conclude that from 175℃ to 350℃, the reaction is proceeding from $Cu_2Sn(Se,S)_3 \rightarrow Cu_2ZnSn(Se,S)_4$. Above 350℃, $Cu_2ZnSn(Se,S)_4$ dominates and stays stable up to at least 540℃.

The Raman spectra shown in Figure 3.5 are supportive of these suggested reaction procedures and the absence of binary phases, except for a small amount of ZnX. The data of the sample annealed at high temperatures exhibits peaks at 175 cm^{-1}, 199 cm^{-1}, and 238 cm^{-1}, in good agreement with the reported vibrational modes of $Cu_2ZnSnSe_4$,[85] and another peak at 327 cm^{-1}, which corresponds to Cu_2ZnSnS_4[67]. Since this kesterite sample contains both sulfur and selenium, the Raman spectrum exhibits bimodal behavior with peaks slightly shifted toward the intermediate frequencies between the primary peaks of

$Cu_2ZnSnSe_4$ and Cu_2ZnSnS_4.[67] At lower annealing temperatures, the dominant peak is located at 187 cm^{-1} but begins shifting toward the 193-199 cm^{-1} range at 350 ℃ and above. This suggests a transformation from $Cu_2Sn(Se,S)_3$ to the $Cu_2ZnSn(Se,S)_4$ phase.[85] ZnSe can be observed at temperatures up to 350℃ by deconvoluting the shoulder of the peak located in the 230-250 cm^{-1} range.[118] The shoulder of this peak is most intense at 175 ℃ and then gradually decreases at higher annealing temperatures, which is consistent with what has been observed in the diffraction studies discussed earlier.

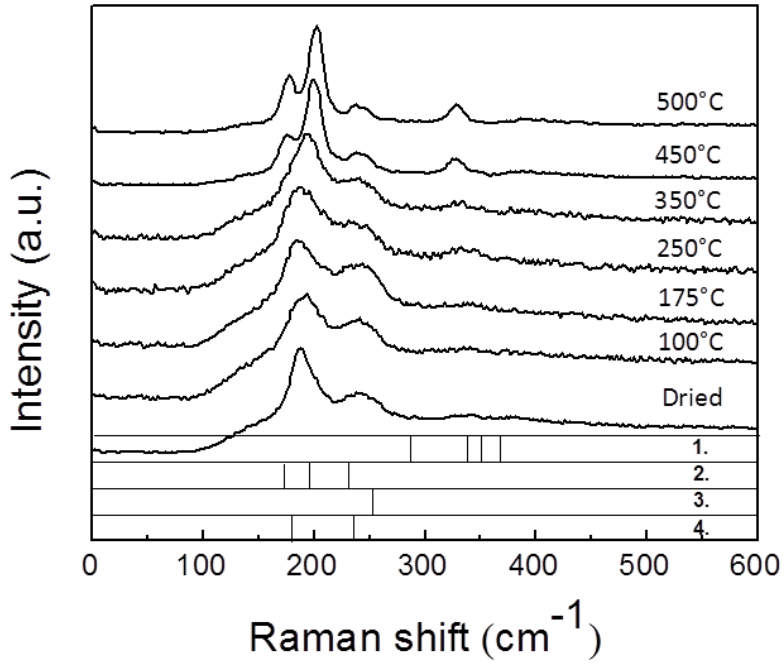

Figure 3.5 Raman spectrum of Cu-Zn-Sn-Se-S precursor dried, annealed at 100 ℃, 175 ℃, 250 ℃, 350 ℃, 450 ℃, and 500 ℃. Spectra of 1. Cu_2ZnSnS_4, 2. Cu2ZnSnSe4, 3. ZnSe, and 4. Cu_2SnSe_3 are also provided for reference.

3.5 Comparison to the reaction pathways of other processes

As predicted by simulation,[119] many reports[114][120][121] have detected Cu_2SnX_3 as an intermediate phase or have claimed that the formation of kesterite is governed by the following solid state reaction:

$$Cu + Sn + Zn + X \text{ or alloys} \rightarrow \text{Binary chalcogenides} \rightarrow Cu_2SnX_3 + ZnX \rightarrow Cu_2ZnSnX_4 ,$$
$$X= S, Se$$

If the process is initiated at the elemental stage, as is the case when depositing metallic layers by evaporation[114][122], sputtering[123], and electroplating[120][124][51], the reaction must progress through every step before CZTSSe is produced or in some processes, start from the second stage by stacking[125] or mixing[121] binary chalcogenides. At each intermediate stage, metal alloys, binary, and ternary chalcogenides (e.g. Cu_2X, CuX, ZnX, SnX_2, SnX, Cu_2SnX_3), each with different formation and decomposition activation energies, will be involved. Perhaps, because the atomic diffusion between intermediate phases is difficult, or the coordination between phases to go through the multiple reaction steps is discordant, the resulting material may retain a variable amount of intermediate phases. Compared to Cu_2ZnSnX_4 phase, the Sn-rich phases, SnX, SnX_2, Cu_2SnX_3, or Cu_4SnX_4, are either very volatile or more easily-decomposed.[126] The consequence of decomposition is the overall stoichiometry drifts

toward the Sn-poor direction, leaving behind detrimental Cu-rich phases, which has no chance to be eliminated from this point on.

Hydrazine-based processing, skipping any activation barriers associated with the first two reaction stages, steps directly into a state between Cu_2SnX_3 + ZnX and Cu_2ZnSnX_4 after the removal of hydrazine ligands. The remaining reaction route is hence kept short and simple. If the ease of kinetic obstacles has enhanced the formation of Cu_2ZnSnX_4 at sub-500℃ annealing temperature and minimized the amount of volatile binary and ternary phases (it is not possible to obtain direct crystallographic evidence that the material is indeed $Cu_2Sn(Se,S)_3$-free because of the difficulty of differentiation by XRD), the whole system will be able to better sustain annealing temperatures beyond 500 ℃ without being decomposed or suffering from the loss of tin but still takes the advantage of the benefits of high temperature annealing, such as the elimination of points defects and grain growth.

3.6 Conclusions and outlook

The hydrazine-based ink processing has been observed to integrate multiple monometallic chalcogenide compounds into a single bimetallic complex at room temperature. Here we have found that, by mixing Cu_2S-S solution and $SnSe_2$-Se solution, the metal chalcogenide complexes $Cu_6S_4^{2-}$ and $Sn_2Se_6^{4-}$ retain their short range vibrational characteristics as observed by Raman scattering. However, the complexes build up an

ordered $Cu_2Sn(Se,S)_y$ hydrazinium framework upon drying rather than constructing their own segregated frameworks.

Further study is needed in order to determine the specific structure of the $Cu_2Sn(Se,S)_x$ hydrazinium framework. However, we already know the structure is not amorphous but well-crystallized with hydrazine or hydrazinium spacer molecules separated by a distance of 9.2555 Å .

The $Cu_2Sn(Se,S)_x$ hydrazinium framework, together with $Zn(Se,S)N_2H_4$, provides a significantly advanced starting point for CZTSSe formation than the precursor materials employed in other deposition methods. Even at temperatures as low as 175℃, the solid state reaction has already begun to progress past the $Cu_2Sn(Se,S)_3$ and Zn(Se,S) stage, rendering the remaining reaction simple and neat compared with most vacuum processes. This reaction pathway is likely beneficial to the performance of the resulting solar cell: the formation of secondary phases such as $Cu_{2-x}S$, SnSe, and $SnSe_2$ is no longer necessary to produce the final $Cu_2ZnSn(Se,S)_4$ phase; the phase conversion is presumably more thorough as the kinetic obstacles of the reaction route are less severe. We believe a pristine $Cu_2ZnSn(Se,S)_4$ material is able to better take advantage of the benefits of high-temperature annealing on device performance while avoiding tin loss and the presence of residual of Cu-rich phases. A reaction pathway starting from an advanced starting point may serve as a general guideline in the search for new promising processes.

Chapter 4 Kesterite from the selenization of nanocrystal films

In Chapter 3, the reaction pathway of hydrazine-processed kesterite is discussed. It is suggested that a solid-state reaction starting from ternary or quaternary precursors is likely beneficial for the formation of kesterite phase. Opposed to that, elemental or binary precursors still have a long way to go before arriving the final stage.

Using nanocrystals to fabricate kesterite films can be described as an approach best realizing this principle. The Cu_2ZnSnS_4 phase is synthesized in liquid phase as nanocrystals capped with hydrocarbon ligands. In the consequent solid-state diffusion, only the growth of the grains needs to take place. In addition, the hydrocarbon ligands allow the nanocrystals to be dispersed in benign common organic solvents, which largely reduce the difficulty to scale up the process. Nevertheless, the increase of the grain size is not straightforward. For unclear reasons, supplying selenium vapor is a must; otherwise the size of grains will remain in nano scale, while selenium vapor is not pleasant to work with because of the toxicity and is much less abundant in the earth crust. The unavoidable selenization step also changes the surface composition of the film into Sn-rich/Zn-poor, which unfortunately favors the formation of those undesired point defects introduced in Chapter 1.

This chapter starts by introducing the basic processes to prepare kesterite films by the nanocrystal approach (Sec. 4.1) and goes into the experimental details of this study (Sec. 4.2). After that, the special grain growth triggered by the selenization step is analyzed and we also try to answer the question why selenium vapor is a must (Sec. 4.3). The focus is

then switched to the surface composition deviation created by the selenization process and the way to engineer the surface composition to favor better device performance (Sec. 4.4). Finally, an 8.6% cell performance is shown. Everything from the kesterite film to the top electrode is deposited without any high vacuum processing (Sec. 4.5). Conclusion and outlook is at last (Sec. 4.6).

4.1 Introduction and challenges of the nanocrystal selenization approach

4.1.1 Nanocrystal synthesis and film formation

Nanocrystal approach starts with the synthesis of metal chalcogenide nanocrystals, the deposition of nanocrystal films, and end with the post-thermal treatment of films.[46] Currently, cell efficiency of 7% to 9% have been achieved by similar processing conditions.[46][45][13][44][43] The record is only second to hydrazine-processed kesterite solar cells[11], and in compatible with co-evaporated kesterite solar cells[14].

The core of the nanocrystals are either quaternary Cu_2ZnSnS_4 nanocrystals[43] or the combination of binary ZnS nanocrystals and ternary Cu_2SnS_3 nanocrystals[127]. Up-to-date, the most successful kesterite devices based on nanocrystal approaches are fabricated from hydrophobic colloidal nanocrystals, which are composed of an inorganic crystalline core with specified composition and crystal phase that is coated with a chemisorbed layer of organic hydrophobic ligands, e.g., oleylamine (OM). (Hydrophilic CZTS nanocrystals are currently not as popular as their hydrophobic relatives and reported to produce inferior device performance.[6][7]) The hydrophobic ligands allow the

nanocrystals to be dispersed in nonpolar solvents and prevent the aggregation between the nanocrystals. Compared with hydrazine-based processing[98], which uses the explosive solvent hydrazine during ink formation and film deposition, there is an wide selection of common nonpolar solvents which can be applied in this processing, including many environmentally benign solvents. An TEM image of Cu_2ZnSnS_4 nanocrystals is shown in Figure 4.1. The resulting nanocrystal dispersed in organic solvent is used as ink to process into 1 to 2 μm films by spin-coating, rod-casting, or other wet coating processes.

The nanocrystal approach enables phase formation to occur prior to film deposition. (Figure 4.1)) In other solution-based processes and vacuum-based processes, including all the other processes listed in Table 1.3 (co-evaporation[14], low-temperature evaporation[15][35][36], sputtering[37][38][39], hydrazine-based processes[40][34][11][41][42], other molecular-scale solutions[47][48][49][50], or electroplating[51]), the kesterite forms either after or during the films form. Due to the difficulty of solid-state diffusion, binary, ternary, and quaternary secondary phases are more likely to form due to compositional non-uniformities throughout the film. As discussed in Chapter 3, the hydrazine-processed kesterite probably has less issues with secondary phases since its solid-state reaction route has an advanced starting point. However, most other processes do not have the luxury. The nanocrystal approach, with phase formation taking place in liquid phase in a carefully controlled environment, allows each constituent to have far greater diffusivity values in order to overcome the activation energy barrier to reach the thermodynamically stable phase.

High-temperature thermal annealing processes of the metal chalcogenide nanocrystal films isnecessary at present stage. As discussed in Sec 1.6, only films with

micron sized grains can avoid excessive recombination and carrier scattering from the grain boundaries and have a chance to produce cells with high power conversion efficiencies. The typical size of the nanocrystals dispersible in organic solvent is ~ 20 nm. Therefore, even though the crystal structure of kesterite has been formed, thermal annealing which leads to remarkable grain growth still cannot be omitted. Current progress has demonstrated that without a grain-growing thermal annealing process, solar cells are generally unable to reach 1% efficiency.[72],

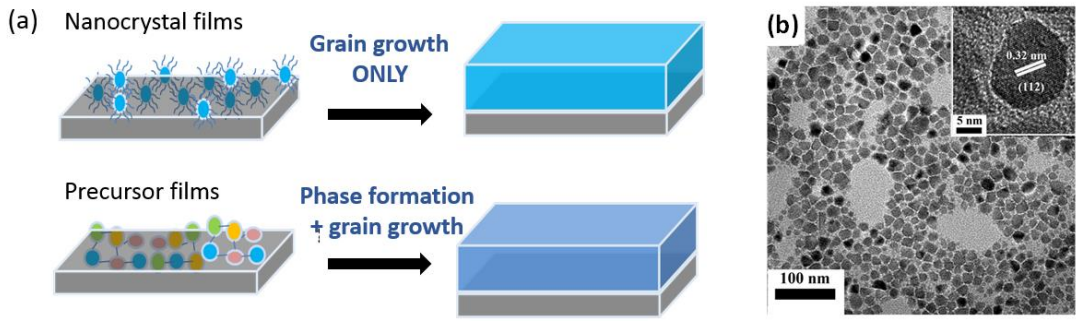

Figure 4.1 The nanocrystal approach enables phase formation to occur prior to film deposition. (a) Schematic illustration of the difference between nanocrystal approach and the others. (b) TEM and HRTEM of the as-synthesis Cu_2ZnSnS_4 nanocrystals.

4.1.2 Selenization and grain growth

Even though the nanocrystals already contain a significant amount of chalcogen (sulfur in most cases), the thermal annealing process of nanocrystal films requires the presence of chalcogen vapor. It is known that the presence of chalcogen vapor (sulfur or selenium vapor) prevents the decomposition of the kesterite phase, since the chalcogen vapor is the product of the decomposition reaction. [130][131] However, the prevention of

decomposition is not the major reason to supply chalcogen vapor in the thermal treatment. The kinetic theory[126] and an experiment example[34] have shown that decomposition can simply be prevented by annealing under environment of atmospheric base pressure even if chalcogen is not supplied. The major reason behind is that this is the only way to attain sub-micron grains out of the nano-sized crystals. Compared to the grain growth mechanism of purer precursor films, such as hydrazine-based precursors[98][41], the grain growth of nanocrystal films is not as straight forward because of the considerable amount of carbon contributed by the nanoparticles hydrocarbon ligands, which presumably hinders the diffusion of atoms. Without supplying chalcogen vapor in the annealing process, the crystals remains mostly nano-sized and the appearance of the film is almost unchanged.

While supplying sulfur (sulfurization) or selenium (selenization) are both reasonable options to prevent the decomposition of CZTS and CZTSe, to-date, successful devices are all made via selenization processes, which replace over 90% of S by Se according to Auger Emission Spectroscopy (AES).[127] The main differences between sulfurization and selenization lie in their ability to initiate and propagate grain growth.

The selenization setup usually makes use of a graphite box holding the as-deposited nanoparticle films and some elemental selenium pellets. The graphite box is placed into a quartz tube furnace with a slow continuous inert gas flow. The finite space inside of the graphite box is critical because it assures that a large selenium pressure will be provided. The annealing temperature is typically reported between 500 ℃ and 560 ℃ for more than 20 minutes.

Selenization of the nanocrystal film produces a bizarre bi-layer structures, with a large-grained layer on top and a fine-grained layer on the bottom and, in some cases, another large-grain layer at the bottom a tri-layer structure. The SEM image shown in Figure 4.2(a) is one of the examples of the double-layer structure and is fairly similar to data reported elsewhere[44], [46]. Figure 4.2(b)[43] is an example of the tri-layer structure. The large-grained layer is the kesterite, and the fine-grained layer is a mixture of kesterite nanocrystals and binary chalcogenide nanocrystals embedded in a matrix of carbon[127]. The carbon is apparently residues of the hydrocarbon chains of the nanocrystals. A similar morphology has also been observed in a different ink-processed CIGS film (Figure 4.6(c))[132], which also involves a significant amount of carbon. (Ethylcellulose was added to improve the coating behavior of the ink.)

These bi-layer or tri-layer structures made from the selenization of nanocrystal films are distinctive and intriguing. The large grains have only presented on the interfaces, which is highly distinguishable from the structures of the films made by carbohydrate ligand-free processes[40][34][11][41][42][49][50][51]. As the example of hydrazine-processed kesterite shown in Figure 4.6(d)[98], grains stacking on each other form everywhere throughout the film. No fine-grained layer is observed. Compared to these structure, the new structure apparently is suggesting an interesting grain growth mechanism.

Previous works have only focused on obtaining reasonable closely-packed large grains to demonstrate a good device efficiency, but unfortunately overlooked the investigation of such growth mechanism, and also had not asked and answered the big question: “why selenium vapor will be necessary to kick off the grain growth?”

It is of interest to understand the growth mechanism by varying the amount of selenium partial pressure in the selenization process. However, with the tubular furnace setup, where the selenium source and the nanocrystal films are placed in a single temperature zone, it is difficult to control selenium vapor pressure and virtually not possible to create pressure higher than the saturated vapor pressure of the substrate temperature. New selenization tool need to be designed.

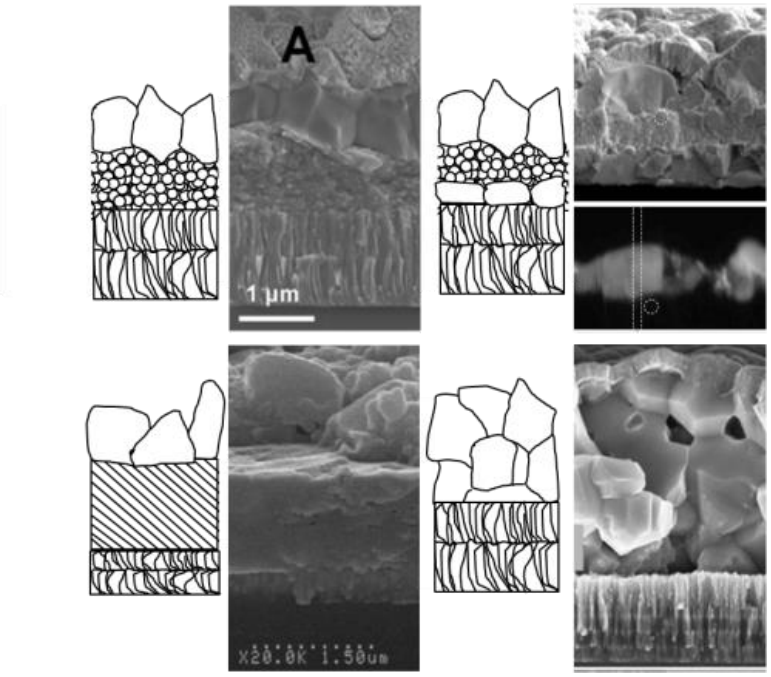

Figure 4.2 Cross-sectional SEM images of annealed films by (a) (b)nanocrystal approach[43], [127] with the EBIC map of the identical area. The dotted lines in (b) are the benchmarks to indicate the same physical location on the sample in each image. Also, cross-sectional SEM images of (c) an organic ink-processed CIGS film [132] and (d) a hydrazine-processed CZTSSe film[98]. Adapted with permission © 2013 The Royal Society of Chemistry.

4.1.3 Composition change during selenization

Selenization not only has a profound effect on grain morphology, but also changes the composition distribution vertically in the film. Generally, as discussed in Sec. 4.1.2,

the change in bulk composition is mild because the decomposition rate is restricted by the atmospheric pressure and the significant amount of selenium vapor present during the annealing process. A more noticeable phenomenon is the production of a vertically non-uniform distribution of metallic elements as a result of the complex bi-layer or tri-layer morphology [127]. Variation of composition is not surprising since the constitution of the thermodynamic system is complex throughout the vapor / large-grain kesterite / nano-sized grains-carbon mixture / $MoSe_2$ structure during selenization. So far, there are no studies showing how the composition distribution has been changed before/after the selenization step and how to adjust the distribution to favor the device performance.

It is worth to note that, in general, the open circuit voltage (V_{OC}) of kesterite solar cell is limited by interfacial recombination.[30][34] It is particular interesting to investigate the composition on the surface of the film. Further optimization of the surface composition may reduce the localized defect density, weakening the recombination process around the p-n junction and, in result, gaining the value of V_{OC} and cell efficiency.

4.2 Experimental methods

4.2.1 Synthesis of nanocrystals

In a typical synthesis of Cu_2ZnSnS_4 nanocrystals, proportional amounts of copper acetylacetonate ($Cu(acac)_2$), zinc acetylacetonate hydrate ($Zn(acac)_2$), tin(IV) bis(acetylacetonate) dichloride ($Sn(acac)_2Cl_2$) were mixed in 10 mL of oleylamine under vacuum from room temperature to 130 ℃, and held at 130 ℃ for 30 minutes; then, the

reaction was heated to 225 ℃ under argon atmosphere, where 2M of sulfur solution in 2 mL oleylamine was injected at 225 ℃, and the temperature was kept at 225 ℃ for 1 hr. The reaction was cooled down to room temperature quickly, and the precipitated products were obtained by adding ethanol as precipitant. The dissolve/precipitation procedure was repeated one more time, and the nanocrystals were acquired and fully dispersed in a non-polar solvent, e.g. toluene. The metal precursor ratio has been adjusted based on the device performance.

4.2.2 Absorber layer fabrication

To prepare the CZTSSe absorber layers, the nanocrystal inks were spin-coated in air on Mo coated soda-lime glass. A soft baking at 300 ℃ for 2.5 minutes on a hotplate in air was applied after each spin-coating run. The thickness of the as-deposited film was adjusted to be 1.1 to 1.2 um by several spin-coating iterations. X-ray Fluorescence was used to check whether the nanocrystal film contains the desired composition prior to further fabrication.

The following selenization was carried out in to different configurations. The first one is named as the “tubular furnace“ setup. The tubular furnace setup is in general identical to the conventional setup discribed in the previous works[13][44][45][46]. The as-deposited films together with several hundred mg of selenium shot were put into a graphite box, and heated in a quartz tube by a tubular furnace. The optimized selenization conditions was carried out at 560 ℃ for 20 minutes, under high pressure (1.15 atm), with argon atmosphere.

The other setup up named as close-space selenization (CSS) decoupled the substrate temperature and selenium source temperature. CSS is a furnace equipped with two face-to-face arrays of heating elements—one heats the source container and one heats the substrates. The working distance between the two arrays is less than 1 cm. Two thermal couples in direct contact with the back of the source container and the back of the substrates allow for accurate control on the two temperatures in separation. The chamber was filled with argon gas with a base pressure of 1.05 atm. The duration of the selenization runs was 15 min. A skeptical drawing of the configuration of CSS furnace is shown in Figure 4.3.

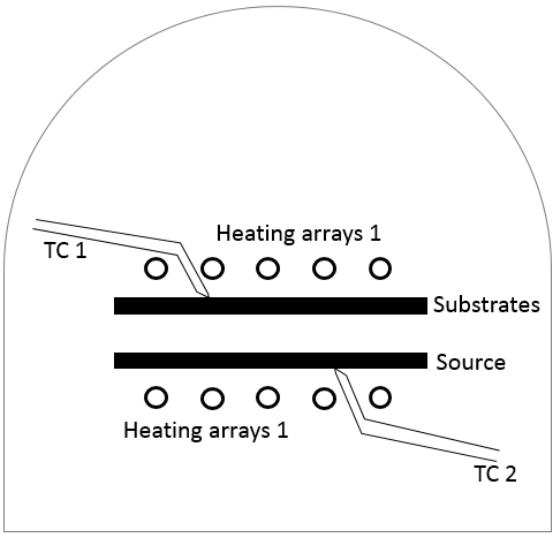

Figure 4.3 Configuration of CSS chamber.

4.2.3 Device Fabrication

The typical procedure was as followed: first, deposition of molybdenum (Mo, around 350 nm) onto a Corning 2947 glass side by DC sputtering in argon. Then, the kesterite absorber layer was deposited according to the above procedure. Next, the

cadmium sulfide (CdS) layer was deposited onto the kesterite layer by chemical bath deposition. Finally, AgNW/ITO-NP film was spin-coated onto the devices as a transparent top electrode. The area of each cell was 0.12 cm^2.

4.2.4 Characterization

Since the commonly used Energy dispersive spectroscopy (EDS) or X-ray Fluorescence (XRF) can only give the bulk metal ratios of the large-grain layer, X-ray photoelectron spectroscopy (XPS) with depth profiling is used in this study. Scanning electron microscope (SEM) is used to characterize the morphologies of the films.

4.3 Selenium pressure-dependent grain morphology

As mentioned in Sec 4.1, in previous works[13][44][45][46], only one heating source was applied to the graphite box containing the films, which supplies the heat to both evaporate the selenium source and allow the selenium vapor to react with the nanocrystal films. In such case, multiple parameters, involving selenium partial pressure and atomic diffusivity were bound together. In this study, the CSS furnace equipped with two arrays of face-to-face heating elements as described in Sec. 4.2 was used. The selenium source temperature and substrate temperature were decoupled and the effects of these two temperature on grain morphology have been demonstrated separately.

Table 4.1 shows the various source and substrate temperatures applied and the assigned sample names. The source temperature and substrate temperature each range from 430 ℃ to 580 ℃.

Table 4.1 Experimental conditions of the CSS selenization runs.

Source temperature (℃)		**Substrate temperature (℃)**				
		580	530	500	480	430
	580		A	II		
	530	a	B/b		c	d
	500	III		I		
	480		C			
	430		D			

4.3.1 Planar-type growth and inhomogeneous-type growth

By varying the source and substrate temperatures, two different types of morphologies of the large-grained layer have been observed. In the “planar type”, the large kesterite grains on top of the film almost fully cover the surface of the fine-grained layer. These grains are flat in shape and packed closely with each other in the way of soap-bubble membranes. In another type, the “inhomogeneous type”, grains are multifaceted in three dimensions and only have contact with the neighboring grains on the base of the grains, leaving an incomplete coverage and occasional exposure of the fine-grained layer. Since these grains have more facets exposed than the flat grains of the planar type, the film surface is also rougher.

The source temperature and substrate temperature both decide whether the resulting morphology falls in the planar type or the inhomogeneous type, whereas the trend is in opposite directions. Figure 4.4 shows the planar and the cross-sectional SEM images of the results of selenization run I, II, and III. By applying 500 ℃ to both the source and the substrate, closely packed grains are obtained, but voids can still be spotted (run I). By raising the source temperature from 500℃ to 580℃, the morphology is shaped into a typical planar type. The grains are larger and also flatter judging from the clear-cut surface in the cross-sectional SEM image; they are also packed even tighter so that no voids can be seen in the planar SEM image (run II). However, by raising the substrate temperature by the same amount, even though the grains still grow bigger, the morphology is shaped into the inhomogeneous type. The height of the grains varies by several times according to the cross-sectional image, and even the voids are enlarged, as indicated by the planar SEM image (run III).

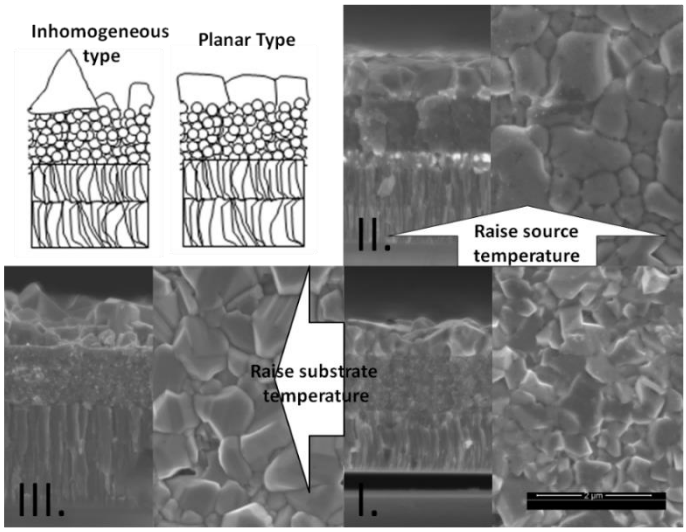

Figure 4.4 The sketches of typical Planar Type and Inhomogeneous Type morphology and the cross-sectional and planar SEM images of the resulting films of selenization runs I, II, and III.

Figure 4.5 presents the consistent phenomena in a wider temperature range down to 430 ℃. A series of selenization A-D were conducted with a fixed substrate temperature at 530 ℃ and a source temperature ranging from 430 ℃ to 580 ℃. It shows that the continuity of the grains increases with increasing source temperature, which indicates that the higher the selenium partial pressure, the more the grains tend to grow like flat soap bubble membranes, instead of individual multifaceted islands. Another series of selenization a-d, in which source temperature was fixed at 530℃ and substrate temperature was varied from 430 ℃ to 580 ℃, shows that the grain growth falls into the planar type regardless of the substrate temperature.

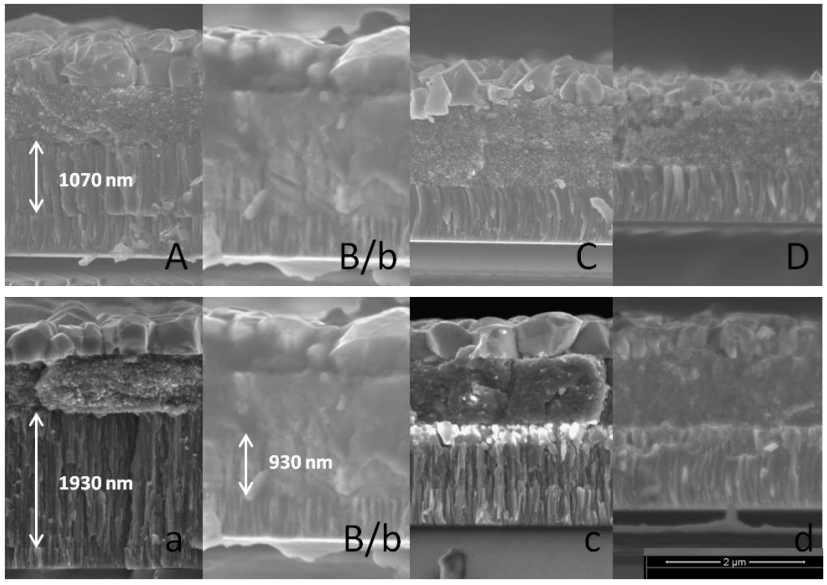

Figure 4.5 The cross-sectional SEM images of the resulting films of selenization runs A, B, C, D; a, b, c, and d.

4.3.2 Other effects on film morphology

The effects of source/substrate temperature on the thickness of $MoSe_2$, the thickness of fine-grained layer, and also the appearance of the second large-grained layer are discussed as followed.

First, the substrate temperature has a greater effect on the thickness of $MoSe_2$ compared to the rapidness of selenium source evaporation. As shown in Figure 4.5, while raising the source temperature from 530℃ to 580℃ increases the $MoSe_2$ thickness by only 15%, raising an equal amount to the substrate temperature almost doubles the thickness.

Second, it is worth to note that neither changing the substrate nor the source temperature in the investigated temperature range noticeably affects the thickness of fine-grain layer.

The last eye-catching effect is the appearance of the second large-grained layer at the bottom of fine-grained layer, which is only observed when low substrate temperatures (480℃ and 430℃) was applied in the case of 530℃ source temperature. Selenization runs with lower source temperature does not yield this second large-grained layer.

4.3.3 How selenium vapor trigger the grain growing process?

After understanding the selenium pressure-dependent grain morphology, now, we try to answer the question: why selenium vapor is necessary to kick of grain growth?

Since the formation of the large grains only occur on the interfaces, it apparently did not start with the sintering between the nano-sized particles, but the heterogeneous nucleation of new grains. Nucleation occurs preferably on the interfaces where the surface energy is the highest, making the nucleation barrier low enough to pass. While once the

nucleus are born on the interfaces, grains can grow into one or more microns in diameter, the simple sintering or ripening of nanocrystals in the bulk of the film proceeds incredibly slow, that even after hours no change in size can be observed with the resolution of SEM. A previous in-situ XRD study on the process of selenization also has indicated supportive evidence. The XRD peaks of the original Cu_2ZnSnS_4 phase does not turn gradually into the new $Cu_2ZnSn(S,Se)_4$ peaks; instead, the new peaks representing the large grains show abruptly when the temperature rises to a certain level.[133]

Here, two possible models are proposed to explain how selenium vapor results in the formation of micron-sized grains. Model 1, the introduction of selenium vapor had modified the film/vapor interface and somehow increased the surface energy and reduced the nucleation barrier.[134] Model 2, the introduction of the selenium vapor has increased the diffusivity of atoms in the film, facilitating the significant growth of the nucleus. According to the grain morphology study summarized in Sec. 4.3.1 and Sec 4.3.2, Model 1 is in better consistency with the observations.

If we assume Model 2 − selenium vapor increases the diffusivities of atoms − is true, in theory, raising source temperature, which bring up the selenium pressure, should have produced the same effect as raising the substrate temperature does: experienced higher atom diffusivity, obvious grain agglomeration, and the formation of multifaceted three-dimensional grains to reduce surface energy, and even leave part of the fine-grained layer surface exposed. However, it is not what have been observed experimentally. Instead, raising substrate temperature leads to the inhomogeneous growth, which matches our expectation on the growth with higher atomic diffusivities; raising source temperature leads

to entirely opposite result, the flat, close packed planar growth, in which the surface energy of the grains have not been minimized.

Model 1 is more consistent with the observation. The selenium vapor in contact with the nanocrystal films possibly increases the surface energy of the nanocrystal films, reducing the nucleation barrier for the new kesterite grains. However, it is not yet understood why a lower substrate temperature coupled with a higher source temperature would promote the nucleation of kesterite grains on the nanocrystal film/Mo interface. It is for sure that, increased atomic diffusivity is again not the trigger of the event, since if so, raising substrate temperature would instead promote the process.

This studies has improved our understanding but not fully realize how grain growth is encouraged by selenium vapor during the thermal treatment. However, the suggested model may point out possible ways to trigger grain growth process without the involvement of selenium vapor.

4.4 Inhomogeneous vertical composition distribution and altered surface composition

4.4.1 Composition depth profiling and Sn-rich surface composition

After realizing the nucleation and growth mechanism of the films, the low uniformity of elemental distribution is not surprising. Since during the selenization of the nanocrystal films, the nucleus are only formed on the surface of the films, metal elements

have to diffuse out from the nanocrystal films to reach the surface and join the growth of nucleus.

Figure 4.6(a) shows the composition depth profile of a selenized film acquired by XPS. The selenization setup used was the "tubular furnace" described in Sec. 4.2. A non-uniform distribution of Cu, Zn, and Sn vertically through the film is observed. It is found that Sn is slightly concentrated towards the front of the film, Cu is concentrated in the middle of the large grain layer, and Zn is slightly concentrated near the boundary between the large and small grained layers. Deeper into the film, near where the large and fine grains intersect, Zn shows signs of accumulation compared to Cu and Sn. Crossing the boundary between large and fine grains and further into $MoSe_2$ layer, all three metallic elements drop continuously.

As discussed in Sec. 4.1.3, the surface composition is particularly of interest. To get more insights into the composition deviation at the surface, we analyzed the film surface by XPS depth profiling with higher resolution (Figure 4.6(b) and (c)). In this view, a trend of Cu/Zn deficiency and Sn abundancy at the front of the absorber layer is evident. From the bulk (~ 300 nm deep into the film) to the top surface, the Sn content increases significantly, while both Cu and Zn contents fall. Compared to the bulk of the film, the surface is poorer in Cu by 3.6%, poorer in Zn by a slight 1.2%, and richer in Sn by a good 4.8%. In result, the Zn/Sn ratio on the surface has reduced down to 1.05, which is much lower than the 1.31 of the bulk composition. The same trend of composition deviation is observed repeatedly in multiple samples. No evidence of secondary phases such as $SnSe_2$ and SnSe can be found by SEM planar view and Raman spectroscopy. One possible

explanation is that the surface of the film favors a construction which has a composition richer in Sn and poorer in Zn compared to the bulk composition.

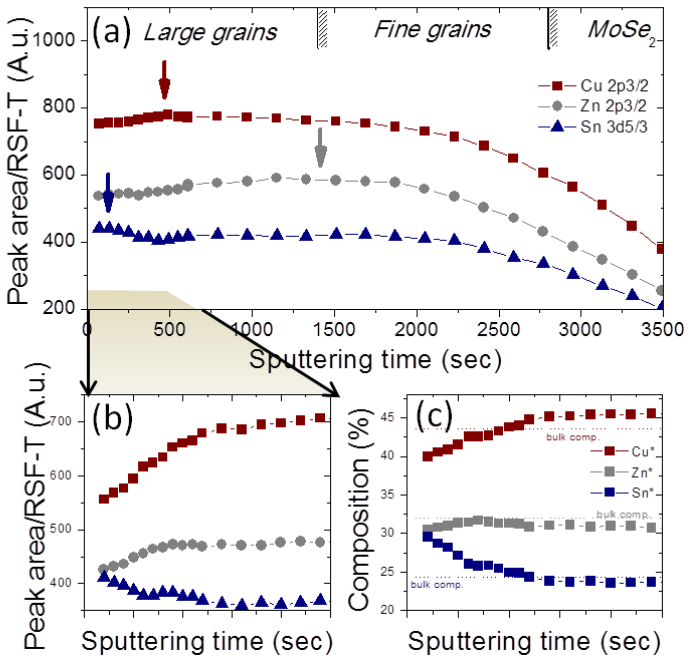

Figure 4.6 XPS depth profiles of a selenized film with bulk composition typical of other works in literature. (a) Peak area corrected for transmission, energy dependence, and RSF of Cu-2p3/2, Zn-2p3/2 and Sn-3d5/3. The arrows indicate where the elements are most concentrated. The margins of large grains/fine grains and $MoSe_2$ were estimated by comparing the depth profiles to SEM cross-sectional images. (b) High resolution scans of the surface region of each absorber layer. (c) The composition Cu*, Zn*, and Sn* profiles of the top ~ 300 nm of absorber. The dotted lines represent the bulk composition acquired by XRF.

To understand if the Sn-rich/Zn-poor surface is a result of selenization, composition depth profiles before and after selenization are given. An additional film was prepared by spin-coating an extra Sn poor nanocrystal ink onto a normal film. Their composition depth profiles before and after selenization are presented in Figure 4.7. It is found that no matter the as-deposit film has a Sn-rich/Zn-poor surface (Figure 4.7(a)) or a Sn-poor/Zn-rich surface (Figure 4.7(b)), the resulting selenized films always have a Sn-rich/Zn-poor surface

(Figure 4.z(c) and (d)). It is therefore confirmed that the Sn-poor/Zn-rich surface is a result of selenization. Presumably, during the growth of large grains, Sn tends to diffuse more rapidly upwards compared to the other two metals, whereas Zn diffuses the most slowly upwards and is more easily trapped at the interface between large and fine grains. Such redistribution renders the first ~300 nm of the absorber in the vicinity of the junction slightly Sn-rich relative to the targeted bulk composition, and the composition deviation on the surface especially evident.

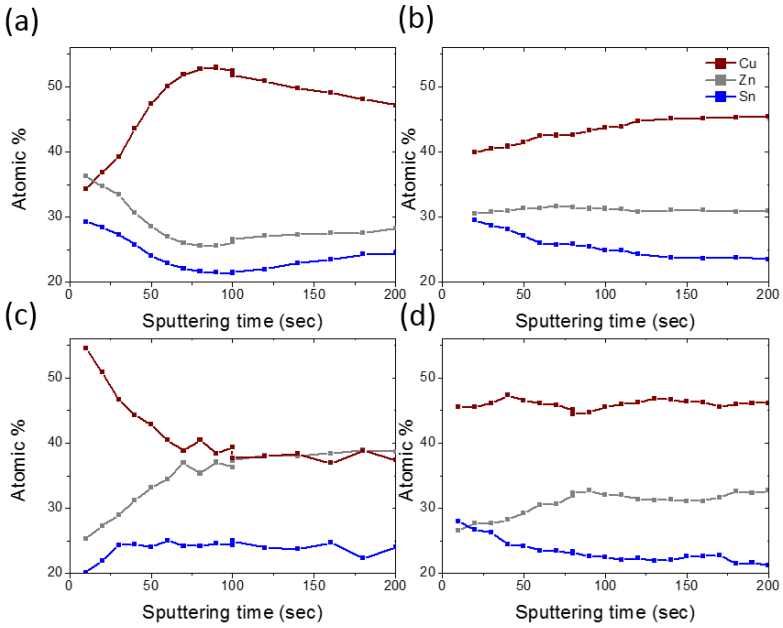

Figure 4.7 Surface depth profiles before and after selenization. (a)(b) A regular nanocrystal film before and after selenization. (c)(d) An modified nanocrystal film before and after selenization.

The relatively Zn-poor and Sn-rich surface composition here is distinguishable from other studies by the hydrazine-based processing, in which large grains grow in a post annealing step with sulfur vapor[135] and the co-evaporation processing, in which large grains grow at the same time elements are deposited on substrates[136]. In both cases, the

kesterite thin films exhibit Cu-poor, Zn-rich, and Sn-poor surfaces. Clearly, there is not only one kind of surface composition deviation for annealed kesterite films. Even two films are both chalcogenized during thermal treatment (either sulfurization or selenization) (for example, ref [135] and this study), the resulting surface composition could be very different, depending on the actual grain growing process during the chalcogenization.

4.4.2 Surface composition engineering

As previously discussed, Sn-rich Zn-poor composition is in general not favorable because of the involvement of the Sn_{Zn} and other deep carrier traps. More specifically, electronic structure calculation specializing the defects on surface configurations points out that the energy level of the Sn_{Zn} as surface configuration is also below the conduction band edge of the bulk, acting as recombination centers for carriers. [70] These concerns motivate the modification of the surface composition to avoid or reduce advert Sn-enriched Zn-depleted defects.

To modify the surface composition, a nanocrystal film with a 1.5 X extra heavy dose of Zn has been used. This strategy is chosen because, first, it is already known that partially changing surface composition of an as-deposited film will not change the trend on surface composition deviation caused by selenization. Second, as concluded in Chapter 2, a heavier dose of Zn as much as 1.5X will not cause device-performance issue once the Zn(Se,S) grains aggregate on the back of the film.

The Cu*, Zn*, and Sn* composition of the nanocrystal film used is 38.63%, 39.43%, and 21.93%, respectively (Cu* = Cu/(Cu+Zn+Sn), Zn* = Zn/(Cu+Zn+Sn), and Sn* =

Sn/(Cu+Zn+Sn)). The composition depth profiles of the selenized film are shown in Figures 4.8. Accordingly, not all of the extra Zn has been incorporated into the large grains. As expected, a significant portion of Zn are stored deeper in the film where the carbon-rich fine-grain layer is formed. As a result, the Zn composition of the bulk of the large-grain layer is around 34.5%, which is higher than the 31.7% of the previous sample. Basically, the trend of Sn-rich and Cu-poor has remained the same, however, because of the overdose of Zn, the surface has been forced to appear Zn-neutral. As a result, the Zn/Sn ratio on the surface is increased from 1.05 in the low-Zn film to 1.25 in this high-Zn film. In summary, by introducing additional Zn in the nanocrystals, the Zn-poor and Sn-rich composition at the front of the absorber can been prevented.

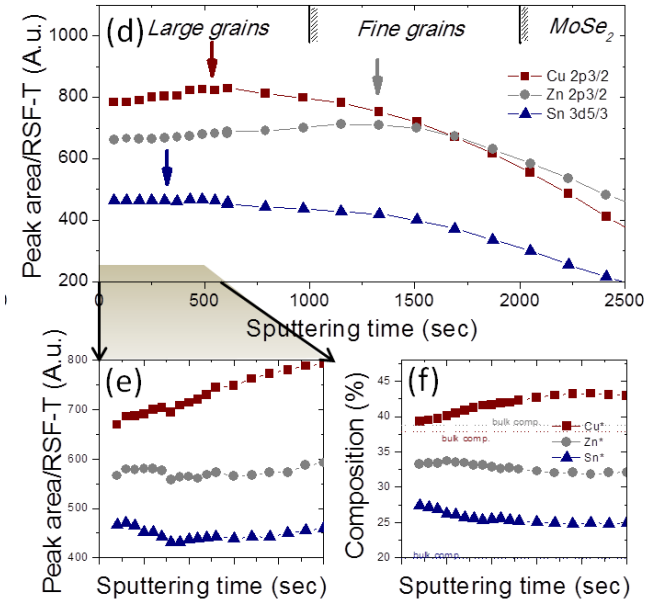

Figure 4.8 XPS depth profiles of a selenized film with significantly higher Zn content. (a) Peak area corrected for transmission, energy dependence, and RSF of Cu-2p3/2, Zn-2p3/2 and Sn-3d5/3. The arrows indicate where the elements are most concentrated. The margins of large grains/fine grains and $MoSe_2$ were estimated by comparing the depth profiles to SEM cross-sectional images. (b) High resolution scans of the surface region of each absorber layer. (c) The composition Cu*, Zn*, and Sn* profiles of the top ~ 300 nm of absorber. The dotted lines represent the bulk composition acquired by XRF.

First-principle calculations[70] also indicate that the thermodynamically stable surface reconstruction is a dependence of chemical potential environment, i.e. film composition during the growth. By growing the film under off-stoichiometric condition toward Zn-rich Cu-poor, the surface energy of the surface constructed by Zn-enriched Cu-depleted defects reduces and that constructed by Sn-enriched Zn-depleted defects (like Sn_{Zn}) increases. At certain point, the Zn-enriched Cu-depleted reconstructed surface is more favorable than the Sn-enriched Zn-depleted reconstructed surface. The calculation may partially explains why in this study when a more Zn-rich Cu-poor Sn-poor composition is chosen, the surface of the film has a higher Zn/Sn ratio. However, a population of undesired Sn-enriched Zn-depleted defects may still exists, since a 1.25 Zn/Sn ratio does not sound high enough, especially when compared with that of the hydrazine-processed kesterite films and co-evaporated kesterite films.

4.5 All-solution processed device

Finally, after correcting the surface composition and optimizing the condition of tubular-furnace selenization, a best cell efficiency of 8.6% is achieved. The composition of the nanocrystal film used is Cu*, Zn*, and Sn* = 39.2%, 38.4%, 22.4%, respectively. The precursor composition was marked in a Cu-Zn-Sn ternary diagram in Figure 4.9(a), alongside several reported compositions that have produced high-performance kesterite solar cells. These previous reports favor slightly Zn-rich compositions, whereas the present absorbers are way much further along the Zn-rich direction.

The photovoltaic devices was fabricated by all-solution processing, which sequentially employed the spin-coating of CZTS nanocrystals, chemical-bath deposition of CdS buffer layer, and spin-coating of a silver nanowire and ITO nanoparticle composite as the top electrode. The use of silver nanowire-ITO nanoparticle composite as transparent electrodes for CISS solar cells are suggested and demonstrated in a previous work.[137] A typical SEM cross-sectional image of the device was shown in Figure 4.9(b). Detailed performance parameters were listed in Table 4.2, including V_{OC} of 0.435V, J_{SC} of 32.5 mA/cm2, and F.F. of 61.0%. When sputtered ITO (anti-reflection layer was not applied) was used to replace the solution processed ITO nanoparticles, the cell efficiency obtained was 6.56%, with comparable V_{oc} but lower J_{sc} and FF, which indicates the R_S contributed by the silver nanowire and ITO nanoparticle composite is actually lower than this particular in-house sputtered ITO.

Table 4.2 The current-voltage (J-V) parameters of the best device

PCE (%)	**V_{OC}(V)**	**Jsc (mA/cm^2)**	**F.F. (%)**
8.62	0.435	32.5	61.0

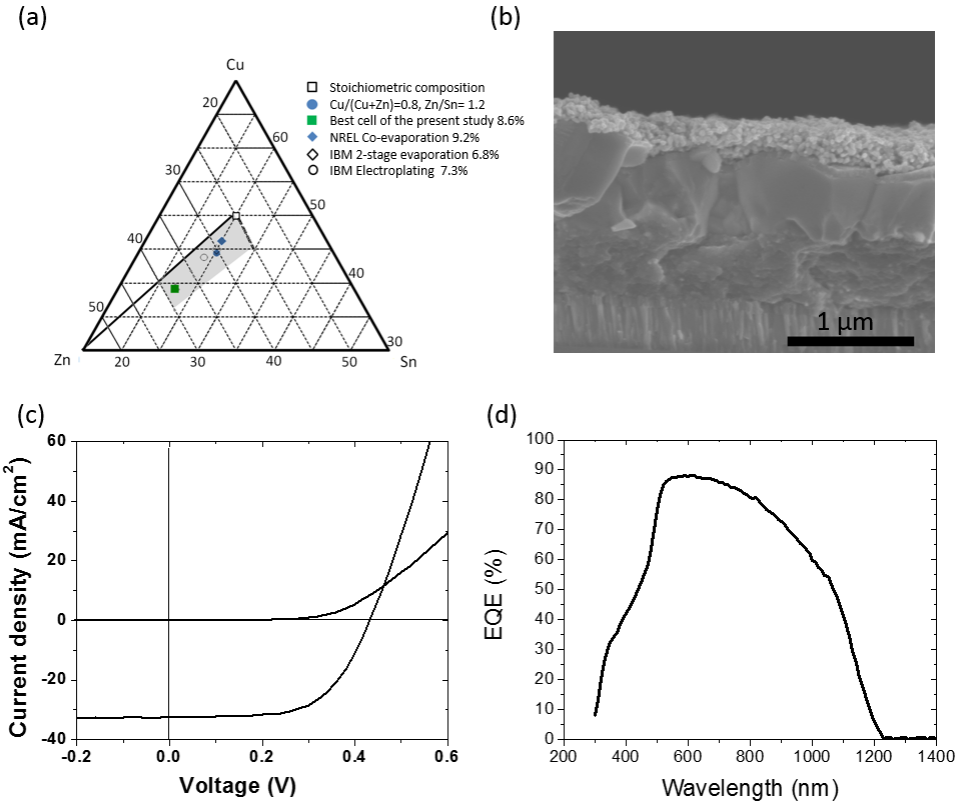

Figure 4.9. (a) A Cu-Zn-Sn ternary diagram showing the stoichiometric composition of kesterite (hollow square), the commonly adopted composition in the literature (solid circle), the composition of the best cells in the present study (solid square) and the compositions of several high-efficiency devices reported in the literature (diamonds and hollow circles). (b) The SEM cross-sectional image of the highest performance device cell. (c) Light and dark J-V curves of the highest performance device. Their bandgaps and J-V parameters are listed in Table 4.2. (d) The external quantum efficiency (EQE) spectra of the device.

4.6 Conclusion and Outlook

Via the study of selenium pressure-dependent and substrate temperature-dependent grain morphology, the process of grain growth during selenization is better understood. A model is suggested to explain why growth is triggered only when selenium vapor is supplied at the studied annealing temperatures. That is: the exposure of the nanocrystal films to selenium vapor increases the surface energy of the films, and thus reduces the

heterogeneous nucleation barrier of the new kesterite grains. While more studies are required to test the suggested model, at minimum, it is certain that the major effect of selenium vapor is not the increase of atomic diffusivities since this assumption clearly contradicts the acquired experimental trend of grain morphology. If the model suggested by this study is correct, it is possible that by additional surface modification, the film surface energy maybe increased and the growth of the grains can be kicked off even without selenium vapor present in the thermal treatment.

As expected, since the selenization step involves the diffusion of atoms up from the nanocrystal films to supply the growth of the nucleus on the top surface, the vigorous vertical movements might have introduced an inhomogeneous vertical composition distribution. In this study, a Sn-rich Zn-poor surface has been found related to the presence of the selenization step. Since such surface composition in theory favors the formation of undesired defect species, surface composition engineering is needed. A simple strategy of using high Zn-dosed nanocrystal films is effective. Possibly, the chemical potential environment of such nanocrystal films has increased the energy of the undesired reconstructed surface and reduced that of the desired reconstructed surface.

At last, by applying surface composition engineering, an 8.6% cell has been achieved. Remarkably, this particular device is made without using any high-vacuum deposition methods all the way from the kesterite layer to the transparent electrode. The high performance of the all-solution processed device illustrates the potential to manufacture low-cost, high-throughput, and high-performance solar cells in the future.

Chapter 5 Summary

As the global population and economy grow rapidly, energy has been an increasingly difficult issue. We not only have to set our minds to developing new technologies to deliver carbon-neutral energy to prevent disastrous interference in the global climate, we also have to consider if the scale of the new energy is large enough to fulfill the growing demands, which will reach 28 TW by year 2050, nearly double today's. Photovoltaics (PVs) certainly use the most abundant energy resource on the earth, sunlight. However, the materials comprising the photovoltaic devices are not always abundant. It is expected that the scale up of the current PV technology will bump into the ceiling of natural resources even before the needed scale has been reached. The topic of this thesis, the kesterite solar cell, has attracted great attention in recent years since the material is composed of earth abundant elements, and therefore free of this concern.

To make kesterite solar cells realistic and cost-effective, both the cell performance and the manufacturing processes have to be effective enough, i.e. high power conversion efficiency, low cost and high throughput. This dissertation has covered the engineering challenges for three different processes on the way to reach these goals − co-evaporation, hydrazine-based coating, and nanocrystal film selenization. In-depth growth mechanisms, including the phase evolutions, reaction pathways, and morphology transitions, have also been studied to help to manage the challenges.

Co-evaporation, distinguishable from all the other available kesterite deposition processes, is the one process allowing the formation of the phases in the film to occur

instantly when the materials are deposited. This signature implies that it is possible to design a phase evolution route or composition transition route, and execute the deposition as planned. Processes using this strategy ("two-stage" and "three-stage" co-evaporation) have set records and broken their own records of CIGS solar cells for more than 20 years. This study has adapted the experience from CIGS and played to the strengths of the deposition of kesterite films. A challenge of how to precisely control the composition/phase of the films is encountered. The major problem is the subtle reaction obstacle between Cu_xSe_y and ZnSe, which is possibly related to the volatile nature of Sn and/or the physical separation between the ZnSe in the film and incident Cu atoms. The remained Cu_xSe_y results in low-performance devices if not removed. Fortunately, an effective solution has been found, and eventually 8-9% cell efficiency is demonstrated via the multiple different deposition routes designed in this study. This work has not determined what kind of deposition route will be the best, and is only the beginning of the search.

The focus of the dissertation, afterwards, moves to non-vacuum solution-based processing, which potentially affords greater scalability and lower cost than co-evaporation processing.

Hydrazine-processed kesterite to-date yields the highest cell efficiency. However, the explosiveness of hydrazine has prevented the process from being realized in industry. It is hoped that by understanding the reaction pathway, all the way from the transformation of liquid-phase precursors to solid-state precursors and finally to the kesterite phase, useful guidelines to select precursors for solution-based processing can be suggested. This work has found that drying the precursor ink at room temperature results in the integration of copper and tin chalcogenide complexes to form a bimetallic framework, with hydrazine

and hydrazinium molecules as spacers. After mild thermal annealing, the spacers are removed and the $Cu_2Sn(Se,S)_3 + Zn(Se,S) \rightarrow Cu_2ZnSn(Se,S)_4$ reaction is triggered. This reaction pathway has an advanced starting point and contains far fewer steps than most deposition processes, which typically start with elemental or binary chalcogenides. As the formation of secondary phases such as $Cu_{2-X}S$, SnSe, and $SnSe_2$ is no longer necessary to produce the final $Cu_2ZnSn(Se,S)_4$ phase, the relative simplicity of this formation mechanism is likely beneficial for the performance of the resulting solar cells.

Using nanocrystals to fabricate kesterite films can be described as an approach best realizing the guideline: adapting an advanced starting point. The kesterite phase is synthesized in liquid phase as nanocrystals and capped with hydrocarbon ligands. In the consequent solid-state diffusion, only the scaling of the grains need to take place. In addition, the hydrocarbon ligands allow the nanocrystals to be dispersed in a wide range of common organic solvents, avoiding the need for dangerous or toxic selections. However, for previously unclear reasons, supplying selenium vapor (in the process named "selenization") is a must to trigger the growth of micron-sized grains in the studied temperature range. This work, on one hand, attempts to answer the question of why selenium vapor is required by studying the mechanism of nucleation and growth, which will be helpful to seek the possibility of avoiding the use of this toxic vapor and further simplify the processes. On the other hand, this work also has found that the selenization step changes the surface composition of the film to Sn-rich/Zn-poor, which unfortunately favors the formation of undesired electrical defects. Through a Zn compensation approach, surface composition has been engineered, and cell efficiency has been improved.

At last, to demonstrate the possibility to fabricate kesterite solar cells without the involvement of high-vacuum deposition processes, a device finished by all-solution process all the way from kesterite deposition to transparent electrode deposition has been prepared. The cell efficiency is 8.6%. The high performance of this all-solution processed device shows the great potential to manufacture low-cost, high-throughput, and high-performance kesterite solar cells in the future.

Appendix A

Logged deposition datasheet for co-evaporation runs described in Chapter 2

The top diagram:

	Cu	**Zn**	**Sn**	**Se**
Color	Red	Green	Blue	Pink

The middle diagram:

	Temperature set point	**Logged temperature**
Color	Red	Black

Note that the logged deposition rates shown here include background counts originated from the cross talks between the evaporants.

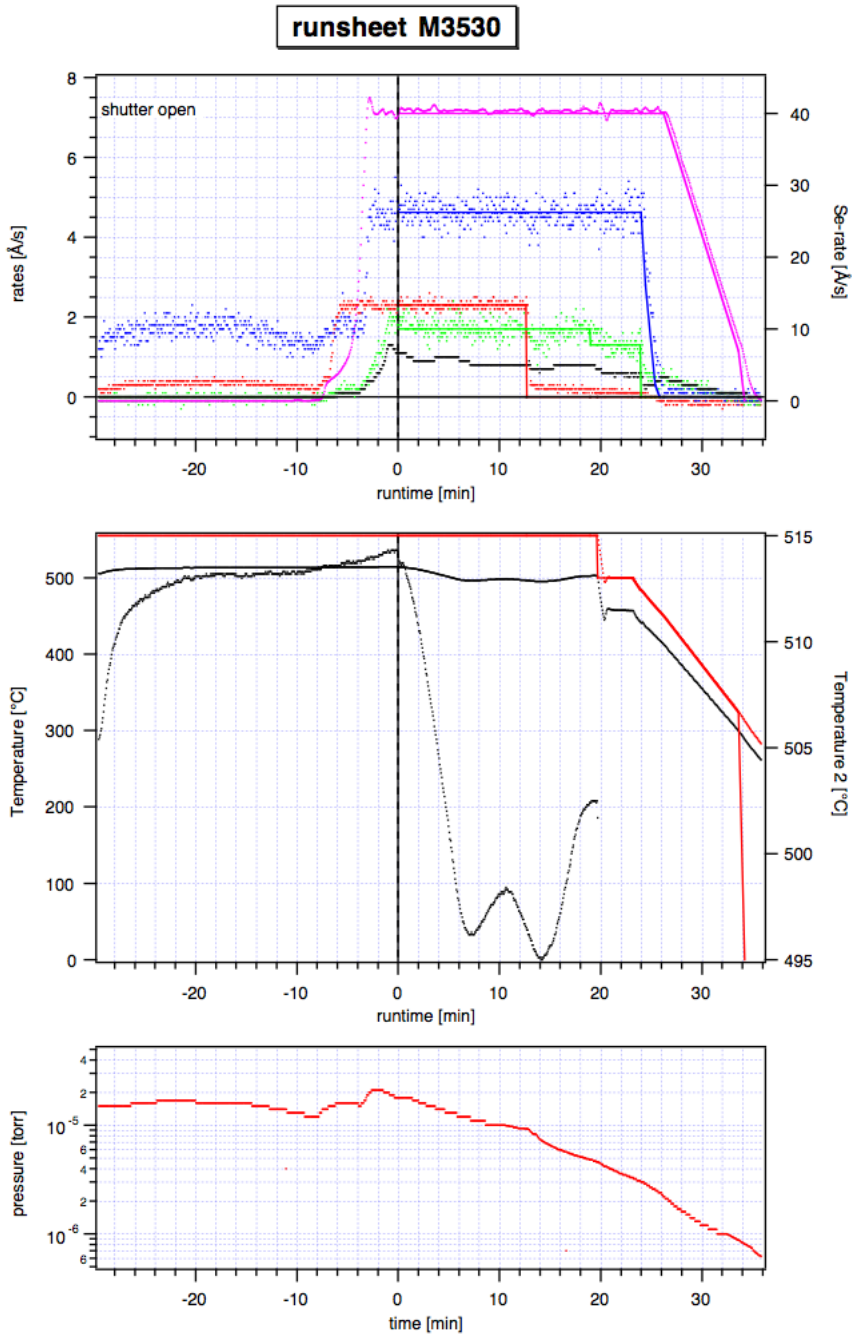

Figure A.1 M3530 a Cu-rich-growth run.

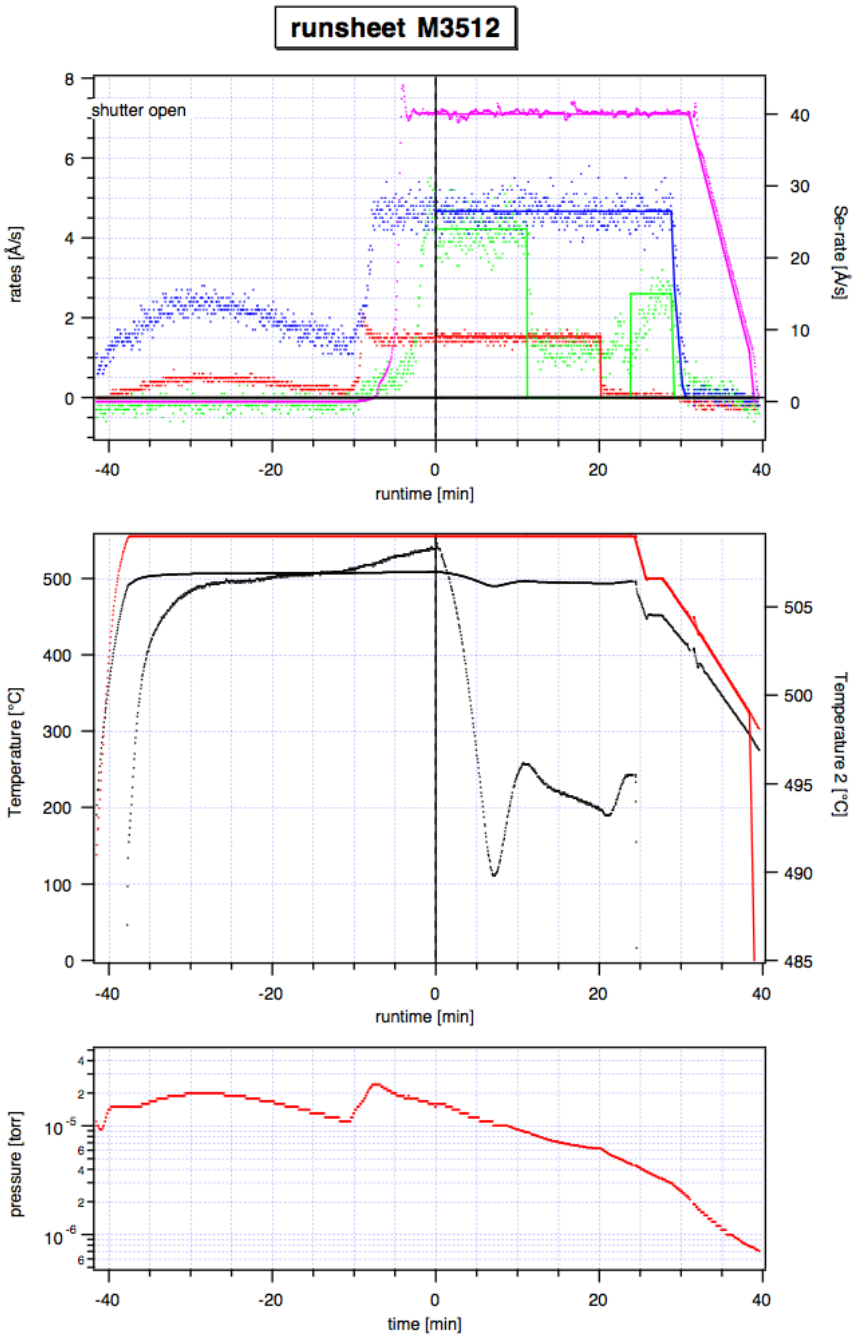

Figure A.2 M3512 a Zn-rich-growth run.

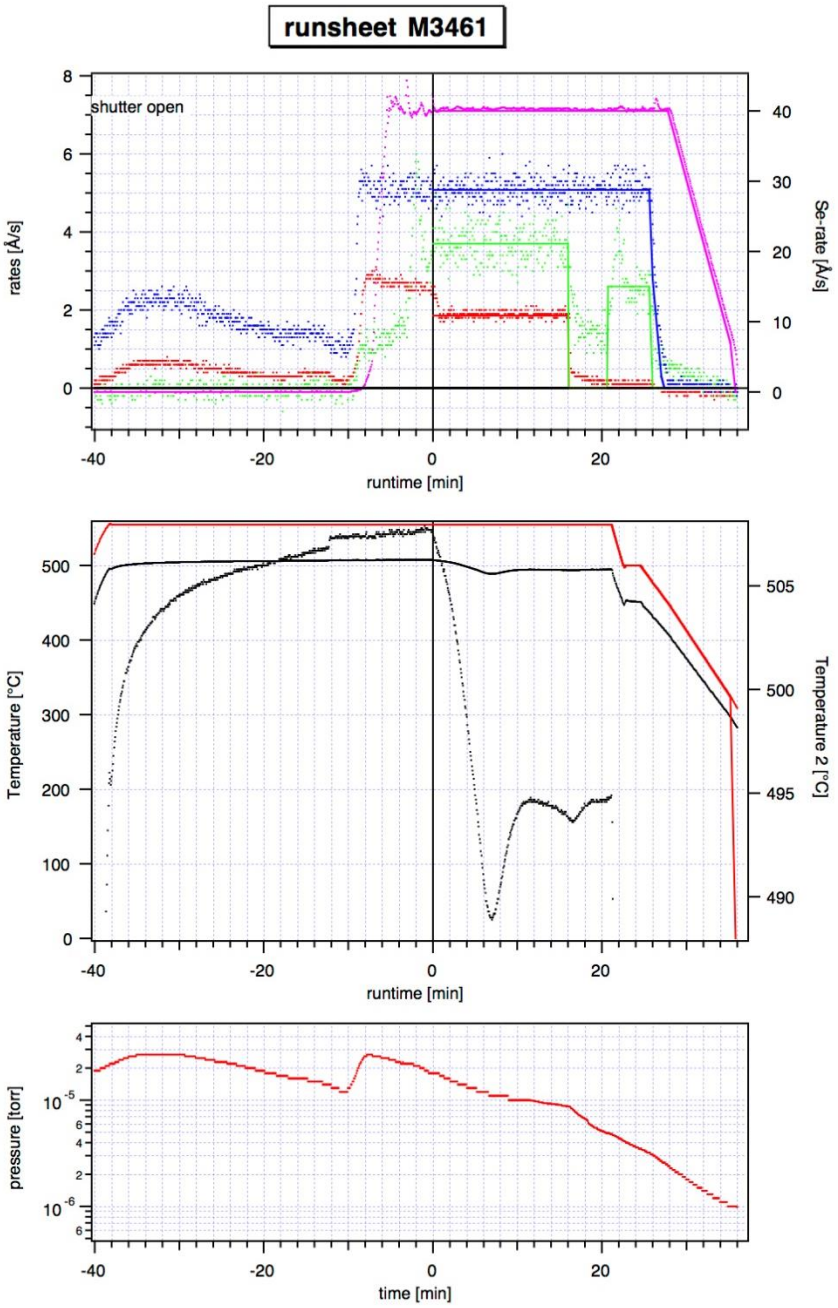

Figure A.3 M3461 a near-stoichiomtric-growth run.

Appendix B

Supporting information for Chapter 3

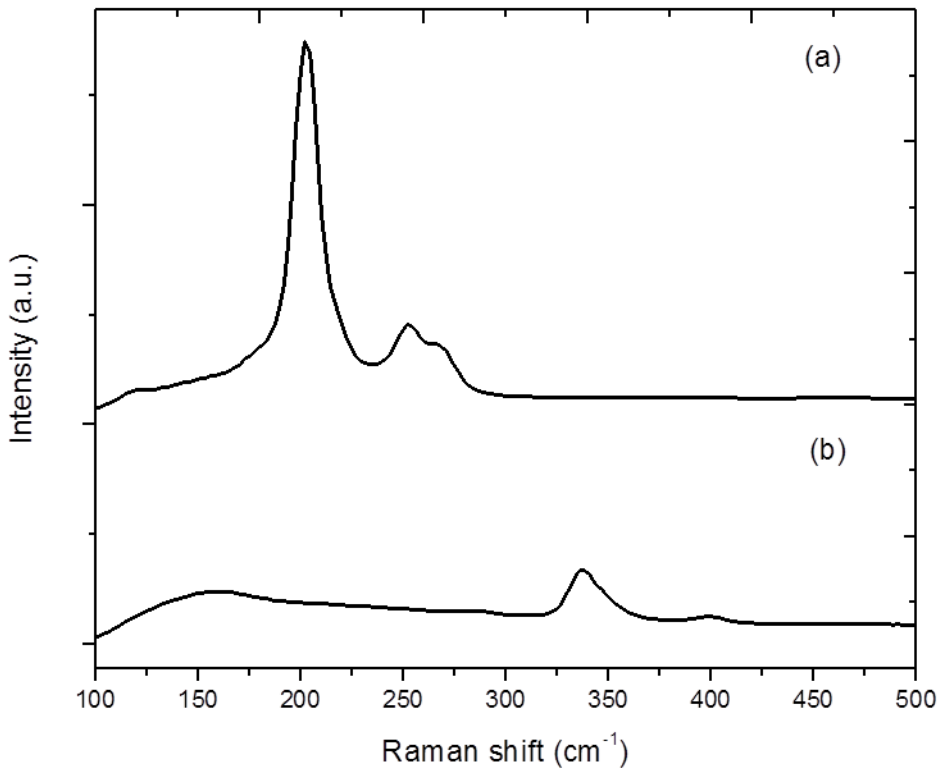

Figure B.1 Raman spectra of (a) $SnSe_2$-Se solution with $SnSe_2$: Se = 1: 1 and (b) Cu_2S-S solution with Cu_2S : S = 1: 2.

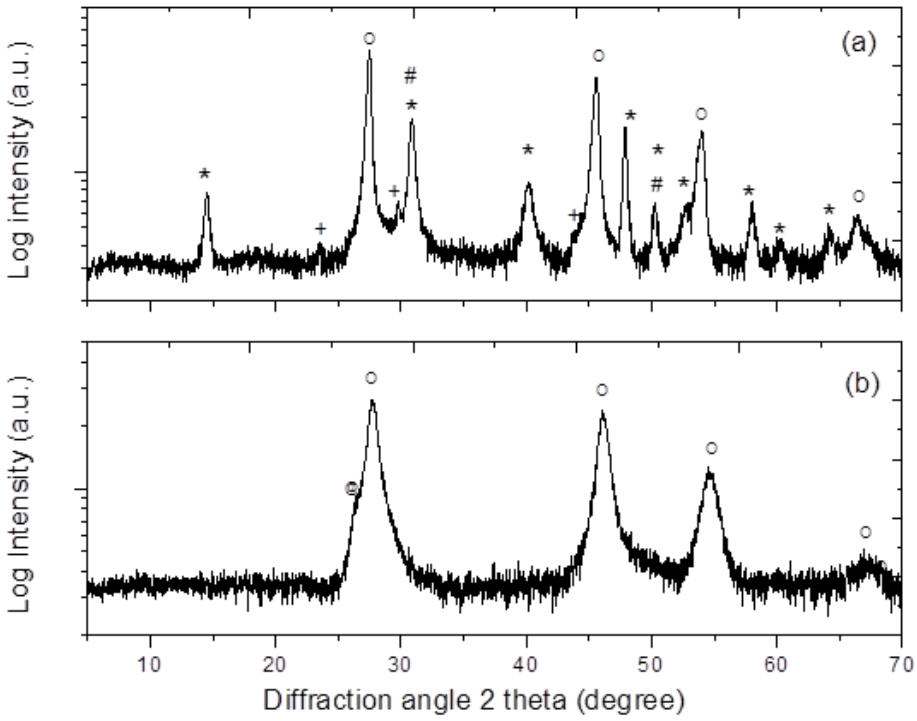

Figure B.2 Powder XRD pattern of the powder prepared by (a) drying Cu_2S-S and $SnSe_2$-Se mixed solution annealing at 200℃, and (b) filtering and drying CZTSe precursor solution. $Cu_2Sn(Se,S)_3$ or kesterite is marked by "o" (reference code 01-089-2879); $SnSe_2$ is marked by "*" (reference code 00-023-0602); CuSe is marked by "#" (reference code 00-049-1457); Se is marked by "+" (reference code 00-042-1425); hexagonal ZnX is marked by "@"

References

[1] M. I. Hoffert, K. Caldeira, A. K. Jain, E. F. Haites, L. D. D. Harvey, S. D. Potter, M. E. Schlesinger, S. H. Schneide, R. G.Watts, T. M.L.Wigley, and D. J.Wuebbles, "Energy implications of future stablization of atmospheric CO2 content," *Nature*, vol. 395, no. October, pp. 881–884, 1998.

[2] J. Tsao, N. Lewis, and G. Crabtree, "Solar FAQs," 2006. [Online]. Available: http://www.sandia.gov/~jytsao/Solar FAQs.pdf.

[3] "Basic Research Needs for Solar Energy Utilization, Report of the Basic Energy Sciences Workshop on Solar Energy Utilization April 2005," *Argonne National Laboratory*, 2005. [Online]. Available: http://www.sc.doe.gov/bes/reports/files/SEU_rpt.pdf.

[4] C. S. Tao, J. Jiang, and M. Tao, "Natural resource limitations to terawatt-scale solar cells," *Sol. Energy Mater. Sol. Cells*, pp. 1–5, Aug. 2011.

[5] "Global marked outlook for photovoltaics," *European Photovoltaic Industry Association*, 2013. [Online]. Available: http://www.epia.org/news/publications/global-market-outlook-for-photovoltaics-2013-2017/.

[6] M. A. Green, K. Emery, Y. Hishikawa, W. Warta, and E. D. Dunlop, "Solar cell ef fi ciency tables (version 43)," *Prog. Photovoltaics Res. Appl.*, vol. 22, pp. 1–9, 2014.

[7] "ZSW achieves record lab CIGS cell efficiency of 20.8%," *PV Tech*. [Online]. Available: http://www.pv-tech.org/news/zsw_achieves_record_lab_cigs_cell_efficiency_of_20.8.

[8] "TSMC records 15.7% champion module," *PV Magazine*, Jun-2013. [Online]. Available: http://www.pv-magazine.com/news/details/beitrag/tsmc-records-157-champion-module_100011749/#axzz2p24VaUwpTSMC records 15.7% champion module.

[9] "Samsung Now the New CIGS Solar Module Efficiency Record Holder," *Greentech Media*, Dec-2013. [Online]. Available: http://www.greentechmedia.com/articles/read/Samsung-Now-the-New-CIGS-Solar-Module-Efficiency-Record-Holder.

[10] "Rare Earth Elements—Critical Resources for High Technology, 087-02, U.S. Geological Survey Fact Sheet." [Online]. Available: http://pubs.usgs.gov/fs/2002/fs087-02/.

[11] W. Wang, M. T. Winkler, O. Gunawan, T. Gokmen, T. K. Todorov, Y. Zhu, and D. B. Mitzi, "Device Characteristics of CZTSSe Thin-Film Solar Cells with 12.6% Efficiency," *Adv. Energy Mater.*, Nov. 2013.

[12] H. Sugimoto, H. Hiroi, N. Sakai, S. Muraoka, T. Katou, and S. F. K. K, "Over 8 % Efficiency Cu2ZnSnS4 Submodules with Ultra-Thin Absorber," vol. 4, pp. 2997–3000, 2011.

[13] Y. Cao, M. S. Denny, J. V Caspar, W. E. Farneth, Q. Guo, A. S. Ionkin, L. K. Johnson, M. Lu, I. Malajovich, D. Radu, H. D. Rosenfeld, K. R. Choudhury, and W. Wu, "High-Efficiency Solution-Processed Cu2ZnSnS,Se4 Thin-Film Solar Cells Prepared from Binary and Ternary Nanoparticles.," *J. Am. Chem. Soc.*, vol. 134, no. 38, pp. 15644–7, Sep. 2012.

[14] I. Repins, C. Beall, N. Vora, C. DeHart, D. Kuciauskas, P. Dippo, B. To, J. Mann, W.-C. Hsu, A. Goodrich, and R. Noufi, "Co-evaporated Cu2ZnSnSe4 films and devices," *Sol. Energy Mater. Sol. Cells*, vol. 101, pp. 154–159, Feb. 2012.

[15] B. Shin, O. Gunawan, and Y. Zhu, “Thin film solar cell with 8.4% power conversion efficiency using an earth-abundant Cu2ZnSnS4 absorber,” *Prog. Photovoltaics Res. Appl.*, vol. 21, no. 1, pp. 72–76, 2013.

[16] S. R. Kodigala, *Cu(In1-xGax)Se2 Based Thin Film Solar Cells*. Elsevier, 2010.

[17] I. L. Repins, M. J. Romero, J. V. Li, S.-H. Wei, D. Kuciauskas, C.-S. Jiang, C. Beall, C. DeHart, J. Mann, W.-C. Hsu, G. Teeter, A. Goodrich, and R. Noufi, “Kesterite Successes, Ongoing Work, and Challenges: A Perspective From Vacuum Deposition,” *IEEE J. Photovoltaics*, vol. 3, no. 1, pp. 439–445, Jan. 2013.

[18] G. Zoppi, I. Forbes, R. W. Miles, P. J. Dale, J. J. Scragg, and L. M. Peter, “Cu2ZnSnSe 4 Thin Film Solar Cells Produced by Selenisation of Magnetron Sputtered Precursors,” *Prog. Photovoltaics Res. Appl.*, vol. 17, pp. 315–319, 2009.

[19] K. Ito and T. Nakazawa, “Electrical and Optical Properties of Stannite-Type Quaternary Semiconductor thin films,” *Jpn. J. Appl. Phys.*, vol. 27, pp. 2094–2097, 1988.

[20] W. Shockley and H. Queisser, “Detailed balance limit of efficiency of p-n junction solar cells,” *J. Appl. Phys.*, vol. 1640, pp. 510–519, 1961.

[21] S. Chen, X. Gong, A. Walsh, and S.-H. Wei, “Electronic structure and stability of quaternary chalcogenide semiconductors derived from cation cross-substitution of II-VI and I-III-VI2 compounds,” *Phys. Rev. B*, vol. 79, no. 16, pp. 1–10, Apr. 2009.

[22] C. Lee and C. Kim, “Optical Properties of Undoped and Co 2 + - doped Cu 2 ZnGeSe 4 Crystals,” vol. 37, no. 3, pp. 364–367, 2000.

[23] B. Friedman, K. Ardani, D. Feldman, R. Citron, and R. Margolis, “Technical Report NREL/TP-6A20-60412 , Benchmarking Non-Hardware Balance-of-

System (Soft) Costs for U.S. Photovoltaic Systems, Using a Bottom-Up Approach and Installer Survey – Second Edition," 2013.

[24] D. Han, Y. Y. Sun, J. Bang, Y. Y. Zhang, H.-B. Sun, X.-B. Li, and S. B. Zhang, "Deep electron traps and origin of p-type conductivity in the earth-abundant solar-cell material Cu2ZnSnS4," *Phys. Rev. B*, vol. 87, no. 15, p. 155206, Apr. 2013.

[25] S. Chen, J.-H. Yang, X. G. Gong, A. Walsh, and S.-H. Wei, "Intrinsic point defects and complexes in the quaternary kesterite semiconductor Cu2ZnSnS4," *Phys. Rev. B*, vol. 81, no. 24, pp. 35–37, Jun. 2010.

[26] S. Chen, X. G. Gong, A. Walsh, and S.-H. Wei, "Defect physics of the kesterite thin-film solar cell absorber Cu2ZnSnS4," *Appl. Phys. Lett.*, vol. 96, no. 2, p. 021902, 2010.

[27] J. Sites and J. Pan, "Strategies to increase CdTe solar-cell voltage," *Thin Solid Films*, vol. 515, no. 15, pp. 6099–6102, May 2007.

[28] S. S. Hegedus and W. N. Shafarman, "Thin-film solar cells: device measurements and analysis," *Prog. Photovoltaics Res. Appl.*, vol. 12, no. 23, pp. 155–176, Mar. 2004.

[29] O. Gunawan, T. Gokmen, C. W. Warren, J. D. Cohen, K. Teodor, D. A. R. Barkhouse, S. Bag, J. Tang, B. Shin, and D. B. Mitzi, "Electronic properties of the Cu2 ZnSn(Se,S)4 absorber layer in solar cells as revealed by admittance spectroscopy and related methods," vol. 253905, pp. 14–17, 2012.

[30] O. Gunawan, T. K. Todorov, and D. B. Mitzi, "Loss mechanisms in hydrazine-processed Cu2ZnSn(Se,S)4 solar cells," *Appl. Phys. Lett.*, vol. 97, no. 23, p. 233506, 2010.

[31] D. A. R. Barkhouse, O. Gunawan, T. Gokmen, T. K. Todorov, and D. B. Mitzi, “Device characteristics of a 10.1% hydrazine-processed Cu2ZnSn(Se,S)4 solar cell,” *Prog. Photovoltaics Res. Appl.*, vol. 20, pp. 6–11, 2012.

[32] I. L. Repins, W. K. Metzger, C. L. Perkins, J. V Li, M. A. Contreras, and A. Trpl, “Correlation Between Measured Minority-Carrier Lifetime and Cu(In,Ga)Se2 Device Performance,” *IEEE Trans. Electron Devices*, vol. 57, no. 11, pp. 2957–2963, 2010.

[33] B. Shin, K. Wang, O. Gunawan, K. B. Reuter, S. J. Chey, N. A. Bojarczuk, T. Todorov, B. Mitzi, and S. Guha, “High efficiency Cu2ZnSn(SxSe1-x)4 thin film solar cells by thermal co-evaporation,” in *IEEE Photovoltaic Specialists Conference (PVSC) 37th*, 2011, pp. 2510–2514.

[34] S. Bag, O. Gunawan, T. Gokmen, Y. Zhu, T. K. Todorov, and D. B. Mitzi, “Low band gap liquid-processed CZTSe solar cell with 10.1% efficiency,” *Energy Environ. Sci.*, vol. 5, pp. 7060–7065, 2012.

[35] K. Wang, O. Gunawan, T. Todorov, B. Shin, S. J. Chey, N. a. Bojarczuk, D. Mitzi, and S. Guha, “Thermally evaporated Cu2ZnSnS4 solar cells,” *Appl. Phys. Lett.*, vol. 97, no. 14, p. 143508, 2010.

[36] A. Redinger and S. Siebentritt, “Coevaporation of Cu2ZnSnSe4 thin films,” *Appl. Phys. Lett.*, vol. 97, no. 9, p. 092111, 2010.

[37] H. Katagiri, K. Jimbo, S. Yamada, T. Kamimura, W. S. Maw, T. Fukano, T. Ito, and T. Motohiro, “Enhanced Conversion Efficiencies of Cu2ZnSnS4-Based Thin Film Solar Cells by Using Preferential Etching Technique,” *Appl. Phys. Express*, vol. 1, p. 041201, Apr. 2008.

[38] J. Scragg and T. Ericson, “Rapid annealing of reactively sputtered precursors for Cu2ZnSnS4 solar cells,” *Prog. Photovoltaics Res. Appl.*, vol. 22, no. 1, pp. 10–17, 2014.

[39] C. Platzer-Björkman, J. Scragg, H. Flammersberger, T. Kubart, and M. Edoff, “Influence of precursor sulfur content on film formation and compositional changes in Cu2ZnSnS4 films and solar cells,” *Sol. Energy Mater. Sol. Cells*, vol. 98, pp. 110–117, Mar. 2012.

[40] T. K. Todorov, J. Tang, S. Bag, O. Gunawan, T. Gokmen, Y. Zhu, and D. B. Mitzi, “Beyond 11% Efficiency: Characteristics of State-of-the-Art Cu2ZnSn(S,Se)4 Solar Cells,” *Adv. Energy Mater.*, vol. 3, no. 1, pp. 34–38, Aug. 2012.

[41] W. Yang, H.-S. Duan, B. Bob, H. Zhou, B. Lei, C.-H. Chung, S.-H. Li, W. W. Hou, and Y. Yang, “Novel solution processing of high-efficiency Earth-abundant Cu2 ZnSn(S,Se)4 solar cells.,” *Adv. Mater.*, vol. 24, no. 47, pp. 6323–6329, Dec. 2012.

[42] C.-J. Hsu, H.-S. Duan, W. Yang, H. Zhou, and Y. Yang, “Benign Solutions and Innovative Sequential Annealing Processes for High Performance Cu2ZnSn(Se,S)4 Photovoltaics,” *Adv. Energy Mater.*, Nov. 2013.

[43] C. Leidholm, C. Hotz, A. Breeze, C. Sunderland, and W. Ki, “Final Report : Sintered CZTS Nanoparticle Solar Cells on Metal Foil Final Report : Sintered CZTS Nanoparticle Solar Cells on Metal Foil, NREL/SR-5200-56501,” 2012. [Online]. Available: http://www.osti.gov/bridge Available.

[44] Q. Guo, G. M. Ford, W.-C. Yang, C. J. Hages, H. W. Hillhouse, and R. Agrawal, “Enhancing the performance of CZTSSe solar cells with Ge alloying,” *Sol. Energy Mater. Sol. Cells*, vol. 105, pp. 132–136, Oct. 2012.

[45] G. M. Ford, Q. Guo, R. Agrawal, and H. W. Hillhouse, “Earth Abundant Element Cu2Zn(Sn1-xGex)S4 Nanocrystals for Tunable Band Gap Solar Cells: 6.8% Efficient Device Fabrication,” *Chem. Mater.*, 2011.

[46] Q. Guo, G. M. Ford, W.-C. Yang, B. C. Walker, E. A. Stach, H. W. Hillhouse, and R. Agrawal, “Fabrication of 7.2% Efficient CZTSSe Solar Cells Using CZTS Nanocrystals.,” *J. Am. Chem. Soc.*, vol. 132, pp. 17384–17386, Nov. 2010.

[47] H. Xin and H. W. Hillhouse, “8.3% Efficient Copper Zinc Tin Sulfoselenide Solar Cells Processed from Environmentally Benign Solvent,” in *IEEE Photovoltaic Specialists Conference (PVSC) 39th*, 2013.

[48] T. Schnabel, M. Löw, and E. Ahlswede, “Vacuum-free preparation of 7.5% efficient Cu2ZnSn(S,Se)4 solar cells based on metal salt precursors,” *Sol. Energy Mater. Sol. Cells*, vol. 117, pp. 324–328, Oct. 2013.

[49] Y. Sun, H. Zheng, X. Li, K. Zong, H. Wang, J. Liu, H. Yan, and K. Li, “Reaction routes for the formation of a Cu2ZnSnS4 absorber material from homogenous ethanol-based solution,” *RSC Adv.*, vol. 3, no. 44, p. 22095, 2013.

[50] Y. Sun, Y. Zhang, H. Wang, M. Xie, K. Zong, H. Zheng, Y. Shu, J. Liu, H. Yan, M. Zhu, and W. Lau, “Novel non-hydrazine solution processing of earth-abundant Cu2ZnSn(S,Se)4 absorbers for thin-film solar cells,” *J. Mater. Chem. A*, vol. 1, no. 23, p. 6880, 2013.

[51] S. Ahmed, K. B. Reuter, O. Gunawan, L. Guo, L. T. Romankiw, and H. Deligianni, “A High Efficiency Electrodeposited Cu2ZnSnS4 Solar Cell,” *Adv. Energy Mater.*, vol. 2, pp. 253–259, Nov. 2012.

[52] “Best Research-Cell Efficiencies,” *National Renewable Energy Laboratory*, 2014. [Online]. Available: http://www.nrel.gov/ncpv/images/efficiency_chart.jpg.

[53] D. Jimenez and W. Williams, “CIGS manufacturing : Promises and reality,” *Photovolt. Int.*, pp. 76–85, 2013.

[54] J. E. Mahan, *Physical Vapor Deposition of Thin FilmsPhysical Vapor Deposition of Thin Films*. Wiley, 2000.

[55] J. Moore, C. Hages, M. Lundstrom, and R. Agrawa, “Influence of Ge Doping on Defect Distributions of CU2Zn(SnxGe1-x)(SySe1-y) Fabricated by Nanocrystal Ink Deposition with Selenization,” in *IEEE Photovoltaic Specialists Conference (PVSC) 37th*, 2011, pp. 1475–1480.

[56] S. Bag, O. Gunawan, T. Gokmen, Y. Zhu, and D. B. Mitzi, “Hydrazine-Processed Ge-Substituted CZTSe Solar Cells,” *Chem. Mater.*, vol. 24, no. 23, pp. 4588–4593, Dec. 2012.

[57] H.-S. Duan, W. Yang, B. Bob, C.-J. Hsu, B. Lei, and Y. Yang, “The Role of Sulfur in Solution-Processed Cu2ZnSn(S,Se)4 and its Effect on Defect Properties,” *Adv. Funct. Mater.*, vol. 23, no. 11, pp. 1466–1471, Oct. 2013.

[58] H. Zhou, T.-B. Song, W.-C. Hsu, S. Luo, S. Ye, H.-S. Duan, C.-J. Hsu, W. Yang, and Y. Yang, “Rational Defect Passivation of Cu2ZnSn(S,Se)4 Photovoltaics with Solution-Processed Cu2ZnSnS4:Na Nanocrystals.,” *J. Am. Chem. Soc.*, Oct. 2013.

[59] J. V. Li, D. Kuciauskas, M. R. Young, and I. L. Repins, “Effects of sodium incorporation in Co-evaporated Cu2ZnSnSe4 thin-film solar cells,” *Appl. Phys. Lett.*, vol. 102, no. 16, p. 163905, 2013.

[60] A. Nagoya, R. Asahi, and G. Kresse, “First-principles study of Cu(2)ZnSnS(4) and the related band offsets for photovoltaic applications.,” *J. physics. Condens. matter*, vol. 23, no. 40, p. 404203, Oct. 2011.

[61] R. Haight, A. Barkhouse, O. Gunawan, B. Shin, M. Copel, M. Hopstaken, and D. B. Mitzi, "Band alignment at the CuZnSn(SxSe1−x)4/CdS interface," *Appl. Phys. Lett.*, vol. 98, no. 25, p. 253502, 2011.

[62] M. Bär, B. -a. Schubert, B. Marsen, R. G. Wilks, S. Pookpanratana, M. Blum, S. Krause, T. Unold, W. Yang, L. Weinhardt, C. Heske, and H.-W. Schock, "Cliff-like conduction band offset and KCN-induced recombination barrier enhancement at the CdS/Cu2ZnSnS4 thin-film solar cell heterojunction," *Appl. Phys. Lett.*, vol. 99, no. 22, p. 222105, 2011.

[63] J. J. Scragg, T. Kubart, J. T. Wa, T. Ericson, M. K. Linnarsson, and C. Platzer-bjo, "Effects of Back Contact Instability on Cu2ZnSnS4 Devices and Processes," *Chem. Mater.*, vol. 25, no. 15, pp. 3162–3171, 2013.

[64] S. López-Marino, M. Placidi, A. Pérez-Tomás, J. Llobet, V. Izquierdo-Roca, X. Fontané, A. Fairbrother, M. Espíndola-Rodríguez, D. Sylla, A. Pérez-Rodríguez, and E. Saucedo, "Inhibiting the absorber/Mo-back contact decomposition reaction in Cu2ZnSnSe4 solar cells: the role of a ZnO intermediate nanolayer," *J. Mater. Chem. A*, vol. 1, no. 29, p. 8338, 2013.

[65] H. Katagiri, K. Jimbo, M. Tahara, and H. Araki, "The influence of the composition ratio on CZTS-based thin film solar cells," *Mater. Res. Soc. Symp. Proc.*, vol. 1165, pp. M04–01, 2009.

[66] T. Tanaka, A. Yoshida, D. Saiki, K. Saito, Q. Guo, M. Nishio, and T. Yamaguchi, "Influence of composition ratio on properties of Cu2ZnSnS4 thin films fabricated by co-evaporation," *Thin Solid Films*, vol. 518, no. 21, pp. S29–S33, Aug. 2010.

[67] D. B. Mitzi, O. Gunawan, T. K. Todorov, K. Wang, and S. Guha, "The path towards a high-performance solution-processed kesterite solar cell," *Sol. Energy Mater. Sol. Cells*, vol. 95, no. 6, pp. 1421–1436, Jun. 2011.

[68] I. Olekseyuk and P. L. Olekseyuk ID, Dudchak IV, “Phase equilibria in the Cu2S–ZnS–SnS2 system,” *J. Alloys Compd.*, vol. 368, no. 1–2, pp. 135–143, Apr. 2004.

[69] J. Just, D. Lützenkirchen-Hecht, R. Frahm, S. Schorr, and T. Unold, “Determination of secondary phases in kesterite Cu2ZnSnS4 thin films by x-ray absorption near edge structure analysis,” *Appl. Phys. Lett.*, vol. 99, no. 26, p. 262105, 2011.

[70] P. Xu, S. Chen, B. Huang, H. J. Xiang, X.-G. Gong, and S.-H. Wei, “Stability and electronic structure of Cu2ZnSnS4 surfaces: First-principles study,” *Phys. Rev. B*, vol. 88, no. 4, p. 045427, Jul. 2013.

[71] S. Chen, A. Walsh, J.-H. Yang, X. Gong, L. Sun, P.-X. Yang, J.-H. Chu, and S.-H. Wei, “Compositional dependence of structural and electronic properties of Cu2ZnSn(S,Se)4 alloys for thin film solar cells,” *Phys. Rev. B*, vol. 83, no. 12, pp. 1–5, Mar. 2011.

[72] C. Steinhagen, M. G. Panthani, V. Akhavan, B. Goodfellow, B. Koo, and B. a Korgel, “Synthesis of Cu2ZnSnS4 nanocrystals for use in low-cost photovoltaics,” *J. Am. Chem. Soc.*, vol. 131, no. 35, pp. 12554–5, Sep. 2009.

[73] M. A. Contreras, J. Tuttle, A. Gabor, and A. Tennant, “High efficiency graded bandgap thin-film polycrystalline Cu(In,Ga)Se2-based solar cells,” *Sol. Mater. Sol. cells*, vol. 41, pp. 231–246, 1996.

[74] J. R. Tuttle, M. Contreras, M. H. Bode, D. Niles, D. S. Albin, R. Matson, a. M. Gabor, A. Tennant, A. Duda, and R. Noufi, “Structure, chemistry, and growth mechanisms of photovoltaic quality thin-film Cu(In,Ga)Se2 grown from a mixed- phase precursor,” *J. Appl. Phys.*, vol. 77, no. 1, p. 153, 1995.

[75] M. A. Contreras, B. Egaas, K. Ramanathan, J. Hiltner, A. Swartzlander, F. Hasoon, and R. Noufi, “Progress toward 20% efficiency in Cu(In,Ga)Se2 polycrystalline thin-film solar cells,” *Prog. Photovoltaics Res. Appl.*, vol. 7, no. 4, pp. 311–316, Jul. 1999.

[76] T. Dullweber, “Back surface band gap gradings in Cu(In,Ga)Se2 solar cells,” *Thin Solid Films*, vol. 387, no. 1–2, pp. 11–13, May 2001.

[77] O. Lundberg, M. Edoff, and L. Stolt, “The effect of Ga-grading in CIGS thin film solar cells,” *Thin Solid Films*, vol. 480–481, pp. 520–525, Jun. 2005.

[78] P. Jackson, D. Hariskos, and E. Lotter, “New world record efficiency for Cu(In,Ga)Se2 thin-film solar cells beyond 20 %,” *Prog. Photovoltaics Res. Appl.*, 2011.

[79] I. Repins, M. A. Contreras, B. Egaas, C. Dehart, J. Scharf, and C. L. Perkins, “19.9 % -efficient ZnO / CdS / CuInGaSe2 Solar Cell with 81.2 % Fill Factor,” *Prog. Photovoltaics Res. Appl.*, no. 16, pp. 235–239, 2008.

[80] C. Hirayama and Y. Ichikawa, “Vapor pressures of tin selenide and tin telluride,” *J. Phys.*, vol. 67, pp. 1039–1042, 1963.

[81] N. Kohara, T. Negami, M. Nishitani, and T. Wada, “Preparation of Device-Quality Cu(ln,Ga)Se2 Thin Films Deposited by Coevaporation with Composition Monitor,” *Jpn. J. Appl. Phys.*, vol. 34, pp. 1141–1144, 1995.

[82] T. Satoh, S. Hayashi, S. Nishiwaki, S. Shimakawa, Y. Hashimoto, T. Negami, and T. Uenoyama, “Fabrication of Cu(In,Ga)Se2 by in-line evaporation (composition monitoring method using heat radiation),” *Sol. Energy Mater. Sol. Cells*, vol. 67, pp. 203–207, 2001.

[83] T. Negami, M. Nishitani, N. Kohara, Y. Hashimoto, and T. Wada, “Real time composition monitoring methods in physical vapor deposition of Cu(In,Ga)Se2 thin films,” *Mater. Res. Soc. Symp. Proc.*, vol. 426, pp. 267–278.

[84] M. Nishitani, T. Negami, and T. Wada, “Composition monitoring method in CuInSe , thin film preparation,” *Thin Solid Films*, vol. 258, pp. 313–316, 1995.

[85] M. Altosaar, J. Raudoja, K. Timmo, M. Danilson, M. Grossberg, J. Krustok, and E. Mellikov, “Cu2Zn1- xCdxSn(Se1-ySy)4 solid solutions as absorber materials for solar cells,” *Phys. Status Solidi*, vol. 205, no. 1, pp. 167–170, Jan. 2008.

[86] N. Vora, J. Blackburn, I. Repins, C. Beall, B. To, J. Pankow, G. Teeter, M. Young, and R. Noufi, “Phase identification and control of thin films deposited by co-evaporation of elemental Cu, Zn, Sn, and Se,” *J. Vac. Sci. Technol. A Vacuum, Surfaces, Film.*, vol. 30, no. 5, p. 051201, 2012.

[87] E. R. Don and R. Hill, “The structure of CuInSe2 films formed by co-evaporation of the elements,” *Sol. Cells*, vol. 16, pp. 131–142, 1986.

[88] W. Hsu, I. Repins, C. Beall, C. Dehart, B. To, and W. Yang, “Growth mechanisms of co-evaporated kesterite : a comparison of Cu-rich and Zn-rich composition paths,” 2012.

[89] S. Ninomiya and S. Adachi, “Optical properties of wurtzite CdS,” *J. Appl. Phys.*, vol. 78, no. 2, p. 1183, 1995.

[90] M. Köntges, R. Reineke-Koch, P. Nollet, J. Beier, R. Schaffle, and J. Parisi, “Light induced changes in the electrical behavior of CdTe and Cu(In,Ga)Se2 solar cells,” *Thin Solid Films*, vol. 404, pp. 280–286, 2002.

[91] B. Hahn, W. Gebhardt, W. Riedl, and U. Rau, “Cu(In,Ga)Se2 solar cells with a ZnSe bu □ er layer : interface characterization by quantum efficiency measurements,” *Prog. Photovoltaics Res. Appl.*, vol. 7, pp. 423–436, 1999.

[92] A. O. Pudov, A. Kanevce, H. A. Al-Thani, J. R. Sites, and F. S. Hasoon, “Secondary barriers in CdS–CuIn1−xGaxSe2 solar cells,” *J. Appl. Phys.*, vol. 97, no. 6, p. 064901, 2005.

[93] S. B. Zhang, S.-H. Wei, and A. Zunger, “A phenomenological model for systematization and prediction of doping limits in II–VI and I–III–VI[sub 2] compounds,” *J. Appl. Phys.*, vol. 83, no. 6, p. 3192, 1998.

[94] D. B. Mitzi, “Solution Processing of Chalcogenide Semiconductors via Dimensional Reduction,” *Adv. Mater.*, vol. 21, no. 31, pp. 3141–3158, Aug. 2009.

[95] M. Yuan, D. B. Mitzi, W. Liu, A. J. Kellock, S. J. Chey, and V. R. Deline, “Optimization of CIGS-Based PV Device through Antimony Doping,” *Chem. Mater.*, vol. 22, no. 2, pp. 285–287, Jan. 2010.

[96] W. Liu, D. B. Mitzi, M. Yuan, A. J. Kellock, S. J. Chey, and O. Gunawan, “12% Efficiency CuIn(Se,S)2 Photovoltaic Device Prepared Using a Hydrazine Solution Process,” *Chem. Mater.*, vol. 22, no. 3, pp. 1010–1014, Feb. 2010.

[97] W. W. Hou, B. Bob, S. Li, and Y. Yang, “Low-temperature processing of a solution-deposited CuInSSe thin-film solar cell,” *Thin Solid Films*, vol. 517, no. 24, pp. 6853–6856, Oct. 2009.

[98] T. K. Todorov, K. B. Reuter, and D. B. Mitzi, “High-efficiency solar cell with Earth-abundant liquid-processed absorber.,” *Adv. Mater.*, vol. 22, no. 20, pp. E156–9, May 2010.

[99] T. Todorov, O. Gunawan, S. J. Chey, T. G. de Monsabert, A. Prabhakar, and D. B. Mitzi, "Progress towards Marketable Earth-Abundant Chalcogenide Solar Cells," *Thin Solid Films*, vol. 519, no. 21, pp. 7378–7381, Jan. 2011.

[100] D. B. Mitzi, M. Copel, and S. J. Chey, "Low-Voltage Transistor Employing a High-Mobility Spin-Coated Chalcogenide Semiconductor," *Adv. Mater.*, vol. 17, no. 10, pp. 1285–1289, May 2005.

[101] D. B. Mitzi, L. L. Kosbar, C. E. Murray, M. Copel, and A. Afzali, "High-mobility ultrathin semiconducting films prepared by spin coating.," *Nature*, vol. 428, no. 6980, pp. 299–303, Mar. 2004.

[102] D. B. Mitzi, "Synthesis, structure, and thermal properties of soluble hydrazinium germanium(IV) and tin(IV) selenide salts.," *Inorg. Chem.*, vol. 44, no. 10, pp. 3755–61, May 2005.

[103] M. Yuan and D. B. Mitzi, "Solvent properties of hydrazine in the preparation of metal chalcogenide bulk materials and films.," *Dalton Trans.*, no. 31, pp. 6078–88, Aug. 2009.

[104] D. B. Mitzi, I. B. M. T. J. Watson, P. O. Box, Y. Heights, and N. York, "Skim N4H9Cu7S4: A hydrazinium-based salt with a layered Cu7S4- framework," *Society*, vol. 46, no. 3, pp. 926–931, 2007.

[105] C.-H. Chung, S.-H. Li, B. Lei, W. Yang, W. W. Hou, B. Bob, and Y. Yang, "Identification of the Molecular Precursors for Hydrazine Solution Processed CuIn(Se,S) 2 Films and Their Interactions," *Chem. Mater.*, vol. 23, no. 4, pp. 964–969, Feb. 2011.

[106] J. Campbell, L. a. Devereux, M. Gerken, H. P. a. Mercier, A. M. Pirani, and G. J. Schrobilgen, "Ditin(IV) Chalcogenide Anions: 77Se, 119Sn, and 125Te Solution NMR Study of the Sn2 Ch64- and Sn2Ch74-(Ch = Se, Te) Anions, X-ray Crystal Structures

and Raman Spectra of K+(N(CH3)4+)3Sn2Se64-, (enH+)2(2,2,2-crypt-K+)2Sn2Se64-, and(K+)2(2,2,2-crypt-K+)2Sn2," *Inorg. Chem.*, vol. 35, no. 10, pp. 2945–2962, Jan. 1996.

[107] Q.-F. Zhang, W.-H. Leung, X.-Q. Xin, and H.-K. Fun, "Heterometallic Polymeric Clusters Containing Tetraselenotungstate Anion :One-Dimensional Helical Chain {[La(Me2SO)8][(μ-WSe4)3Ag3]}n and Cyanide-Bridged Three-Dimensional Cross-Framework {[Et4N]2[(μ4-WSe4)Cu4(CN)4]}n," *Inorg. Chem.*, vol. 39, pp. 417–426, 2000.

[108] B. Kreb, S. Pohl, and W. Schiwy, "Hexathio-digermanates and -distannates : A New Type of Dimeric Tetrahedral Ion," *Angew. Chem. Int. Ed. Engl.*, vol. 9, pp. 897–898, 1970.

[109] M. Yuan, M. Dirmyer, J. Badding, A. Sen, M. Dahlberg, and P. Schiffer, "Controlled assembly of zero-, one-, two-, and three-dimensional metal chalcogenide structures.," *Inorg. Chem.*, vol. 46, no. 18, pp. 7238–40, Sep. 2007.

[110] M. J. Manos and M. G. Kanatzidis, "Use of hydrazine in the hydrothermal synthesis of chalcogenides: the neutral framework material [Mn2SnS4(N2H4)2]," *Inorg. Chem.*, vol. 48, no. 11, pp. 4658–60, Jun. 2009.

[111] Y. Liu, Y. Tian, F. Wei, M. S. C. Ping, C. Huang, F. Boey, C. Kloc, L. Chen, T. Wu, and Q. Zhang, "A new hydrazine-bridged thioantimonate Mn2Sb4S8(N2H4)2: Synthesis, structure, optical and magnetic properties," *Inorg. Chem. Commun.*, vol. 14, no. 6, pp. 884–888, Jun. 2011.

[112] Y. Dong, Q. Peng, and Y. Li, "Semiconductor zinc chalcogenides nanofibers from 1-D molecular precursors," *Inorg. Chem. Commun.*, vol. 7, no. 3, pp. 370–373, Mar. 2004.

[113] L. Chai, J. Du, S. Xiong, H. Li, Y. Zhu, and Y. Qian, “Synthesis of Wurtzite ZnS Nanowire Bundles Using a Solvothermal Technique,” *J. Phys. Chem. C*, vol. 111, no. 34, pp. 12658–12662, Aug. 2007.

[114] O. Volobujeva, E. Mellikov, J. Raudoja, M. Grossberg, S. Bereznev, M. Altosaar, and R. Traksmaa, “SEM analysis and selenization of Cu-Zn-Sn sequential films produced by evaporation of metals,” pp. 257–260, 2008.

[115] R. A. Wibowo, W. H. Jung, M. H. Al-Faruqi, I. Amal, and K. H. Kim, “Crystallization of Cu2ZnSnSe4 compound by solid state reaction using elemental powders,” *Mater. Chem. Phys.*, vol. 124, no. 2–3, pp. 1006–1010, Dec. 2010.

[116] G. Hema Chandra, O. Lakshmana Kumar, R. Prasada Rao, and S. Uthanna, “Influence of substrate and selenization temperatures on the growth of Cu2SnSe3 films,” *J. Mater. Sci.*, vol. 46, no. 21, pp. 6952–6959, Jun. 2011.

[117] D.-H. Kuo, W.-D. Haung, Y.-S. Huang, J.-D. Wu, and Y.-J. Lin, “Single-step sputtered Cu2SnSe3 films using the targets composed of Cu2Se and SnSe2,” *Thin Solid Films*, vol. 518, no. 24, pp. 7218–7221, Oct. 2010.

[118] C. X. Shan, Z. Liu, X. T. Zhang, C. C. Wong, and S. K. Hark, “Wurtzite ZnSe nanowires: growth, photoluminescence, and single-wire Raman properties,” *Nanotechnology*, vol. 17, no. 22, pp. 5561–4, Nov. 2006.

[119] F. Hergert and R. Hock, “Predicted formation reactions for the solid-state syntheses of the semiconductor materials Cu2SnX3 and Cu2ZnSnX4 (X = S, Se) starting from binary chalcogenides,” *Thin Solid Films*, vol. 515, no. 15, pp. 5953–5956, May 2007.

[120] R. Schurr, a. Hölzing, S. Jost, R. Hock, T. Voβ, J. Schulze, a. Kirbs, a. Ennaoui, M. Lux-Steiner, a. Weber, I. Kötschau, and H.-W. Schock, “The crystallisation

of Cu2ZnSnS4 thin film solar cell absorbers from co-electroplated Cu–Zn–Sn precursors," *Thin Solid Films*, vol. 517, no. 7, pp. 2465–2468, Feb. 2009.

[121] S. Schorr, A. Weber, V. Honkimäki, and H.-W. Schock, "In-situ investigation of the kesterite formation from binary and ternary sulphides," *Thin Solid Films*, vol. 517, no. 7, pp. 2461–2464, Feb. 2009.

[122] P. M. P. Salomé, P. a. Fernandes, and a. F. da Cunha, "Morphological and structural characterization of Cu2ZnSnSe4 thin films grown by selenization of elemental precursor layers," *Thin Solid Films*, vol. 517, no. 7, pp. 2531–2534, Feb. 2009.

[123] P. A. Fernandes, P. M. P. Salomé, and A. F. da Cunha, "Growth and Raman scattering characterization of Cu2ZnSnS4 thin films," *Thin Solid Films*, vol. 517, no. 7, pp. 2519–2523, Feb. 2009.

[124] M. Ganchev, J. Iljina, L. Kaupmees, T. Raadik, O. Volobujeva, A. Mere, M. Altosaar, J. Raudoja, and E. Mellikov, "Phase composition of selenized Cu2ZnSnSe4 thin films determined by X-ray diffraction and Raman spectroscopy," *Thin Solid Films*, vol. 519, no. 21, pp. 7394–7398, Feb. 2011.

[125] a. Weber, H. Krauth, S. Perlt, B. Schubert, I. Kötschau, S. Schorr, and H. W. Schock, "Multi-stage evaporation of Cu2ZnSnS4 thin films," *Thin Solid Films*, vol. 517, no. 7, pp. 2524–2526, Feb. 2009.

[126] A. Weber, R. Mainz, and H. W. Schock, "On the Sn loss from thin films of the material system Cu–Zn–Sn–S in high vacuum," *J. Appl. Phys.*, vol. 107, no. 1, p. 013516, 2010.

[127] Y. Cao, M. S. Denny, J. V Caspar, W. E. Farneth, Q. Guo, A. S. Ionkin, L. K. Johnson, M. Lu, I. Malajovich, D. Radu, H. D. Rosenfeld, K. R. Choudhury, and W. Wu, "High-efficiency solution-processed Cu2ZnSn(S,Se)4 thin-film solar cells prepared

from binary and ternary nanoparticles.," *J. Am. Chem. Soc.*, vol. 134, no. 38, pp. 15644–7, Sep. 2012.

[128] W. Xie, X. Jiang, C. Zou, D. Li, J. Zhang, J. Quan, and L. Shao, "Synthesis of highly dispersed Cu2ZnSnS4 nanoparticles by solvothermal method for photovoltaic application," vol. 45, pp. 16–20, 2012.

[129] Q. Tian, X. Xu, L. Han, M. Tang, R. Zou, Z. Chen, M. Yu, J. Yang, and J. Hu, "Hydrophilic Cu2ZnSnS4 nanocrystals for printing flexible, low-cost and environmentally friendly solar cells," *CrystEngComm*, vol. 14, no. 11, p. 3847, 2012.

[130] J. J. Scragg, T. Ericson, T. Kubart, M. Edoff, and C. Platzer-bj, "Chemical Insights into the Instability of Cu2ZnSnS4 Films during Annealing," pp. 4625–4633, 2011.

[131] J. J. Scragg, P. J. Dale, D. Colombara, and L. M. Peter, "Thermodynamic Aspects of the Synthesis of Thin-Film Materials for Solar Cells.," *Chemphyschem*, vol. 13, pp. 3035–3046, Apr. 2012.

[132] M. Kaelin, D. Rudmann, and A. Tiwari, "Low cost processing of CIGS thin film solar cells," *Sol. Energy*, vol. 77, no. 6, pp. 749–756, Dec. 2004.

[133] R. Mainz, B. C. Walker, S. S. Schmidt, O. Zander, A. Weber, H. Rodriguez-Alvarez, J. Just, M. Klaus, R. Agrawal, and T. Unold, "Real-time observation of Cu2ZnSn(S,Se)4 solar cell absorber layer formation from nanoparticle precursors.," *Phys. Chem. Chem. Phys.*, vol. 15, pp. 18281–18289, Sep. 2013.

[134] D. A. Porter and K. E. Easterling, *Phase Transformations in Metals and Alloys*. Van Nostrand Reinhold, 1981.

[135] R. Haight, X. Shao, W. Wang, and D. B. Mitzi, “Electronic and elemental properties of the Cu2ZnSn(S,Se)4 surface and grain boundaries,” *Appl. Phys. Lett.*, vol. 104, no. 3, p. 033902, Jan. 2014.

[136] I. Repins, N. Vora, C. Beall, S. Wei, Y. Yan, M. Romero, G. Teeter, H. Du, B. To, M. Young, and R. Noufi, “Kesterites and Chalcopyrites: A Comparison of Close Cousins,” *Mater. Res. Soc. Symp. Proc.*, vol. 1324, pp. 97–108, Jun. 2011.

[137] C.-H. Chung, T.-B. Song, B. Bob, R. Zhu, H.-S. Duan, and Y. Yang, “Silver nanowire composite window layers for fully solution-deposited thin-film photovoltaic devices.,” *Adv. Mater.*, vol. 24, no. 40, pp. 5499–504, Oct. 2012.